



Title	Abrupt permafrost thaw processes after wildfire revealed by InSAR and on-site observations at Batagay, Northeastern Siberia
Author(s)	柳谷, 一輝
Citation	北海道大学. 博士(理学) 甲第14794号
Issue Date	2022-03-24
DOI	10.14943/doctoral.k14794
Doc URL	http://hdl.handle.net/2115/89162
Type	theses (doctoral)
File Information	Kazuki_Yanagiya.pdf



[Instructions for use](#)

**Abrupt permafrost thaw processes after wildfire
revealed by InSAR and on-site observations at Batagay,
Northeastern Siberia**

シベリア北東部バタガイにおける山火事後の急激な
永久凍土融解プロセス: InSAR と現地観測による解明

Kazuki Yanagiya

Submitted for the degree of Doctor of Philosophy

Department of Natural History of Sciences,
Graduate School of Science

March 2022



Contents

要旨	v
Abstract.....	vii
List of Abbreviations	ix
List of Figures.....	x
List of Tables	xii
Chapter 1. General Introduction.....	1
1.1 Permafrost	3
1.1.1 Definirion and distribution	3
1.1.2 Positeve feedback to global warming	4
1.1.3 Permafrost thaw and topography change.....	6
1.1.4 Abrupt permafrost thaw.....	10
1.1.5 Study site: Batagay, Sakha Republic, Northeastern Siberia	12
1.2 Space geodetic technique for permafrost.....	16
1.2.1 Fire scar detection with optical data	17
1.2.2 Synthetic Aperture Radar	20
1.2.3 Interferometric SAR.....	22
1.2.4 InSAR for permafrost observation	27
1.3 Thesis outline	30
Chapter 2. Post-wildfire Surface Deformation at the 2014 Fire Scar near	
Batagay, Eastern Siberia, Detected by L-band and C-band InSAR	33
2.1 Introduction	34
2.2 Study Site.....	39
2.3 Methods	40
2.3.1 InSAR and Data Sets	40
2.3.2 Multispectral remote sensing of burn severity	46
2.3.3 One dimensional frost-heave theory based on premelting dynamics	46
2.4 Results	47
2.4.1 Seasonal deformation and comparison of ALOS-2/Sentinel-1 interferograms	48
2.4.2 Long-term deformation inferred from time-series analysis of ALOS-2	

interferograms	52
2.4.3 Estimating the total volume of thawed excess ice	55
2.5 Discussion.....	56
2.5.1 Similarities and differences in the ALOS-2 and Sentinel-1 interferograms: implication for insignificant slope-parallel sliding	56
2.5.2 What controls the heterogeneous distribution of subsidence magnitude? Possible emergence of another megaslump	59
2.5.3 Interpretation of frost-heave signals	61
2.6 Report of on-site observation in 2019	64

Chapter 3. Transient Freeze-Thaw Responses to the 2018 and 2019

Wildfires near Batagaika Megaslump, NE Siberia 67

3.1 Introduction	67
3.2 Data and Method	70
3.2.1 SAR data	70
3.2.2 Thaw Depth Measurement.....	72
3.3 Result.....	75
3.3.1 Seasonal frost heave immediately after wildfire	75
3.3.2 Annual total ground deformation in a burned year.....	80
3.3.3 Temporal changes of thaw depth at the fire scars	83
3.4 Discussion.....	85
3.4.1 Reliability of heave signals in InSAR images	85
3.4.2 Comparison of seasonal freeze-thaw signals at certain unburned areas and fire scars	87
3.4.3 Thaw depth evolutions and frost heave signals at the fire scars.....	88

Chapter 4. Spatio-temporal Heterogeneity of Post-fire Permafrost Thaw

within the 2018-19 Fire Scars 91

4.1 Introduction	92
4.2 Data and Method	94
4.3 Result.....	96
4.3.1 Spatially heterogeneous signals detected L-band InSAR	96

4.3.2 SBAS time series analysis	100
4.3.3 Thaw depth and soil water content measurement.....	103
4.3.3 Pit survey around the gully in the 2019 fire scar.....	105
4.4 Discussion.....	106
4.4.1 Spatial heterogeneity around the gully in the 2019 fire scar	106
4.4.2 Clear boundary of subsidence and heave in the 2018 fire scar	109
Chapter 5. Thesis findings and conclusion	113
Chapter 6. Acknowledgment	117
Chapter 7. Bibliography	119
Chapter 8. Appendix.....	133

要旨

温暖化に伴う永久凍土の融解は、植物や微生物が活動する季節凍土層（活動層）を深化させ、数万年単位で凍結し貯蔵されていた有機炭素を分解し、気温上昇へ更なる正のフィードバックを与える可能性がある。さらに、森林火災や伐採の跡地で進行する“急速融解”は、局所的だが深部まで融解するため、気温上昇による広範かつ一様な融解よりも多くの炭素放出をもたらすのではないかと注目されている。例えば、火災は断熱層である地表有機層を焼失させ、夏季の気温上昇が地表面に直接作用するため、植生が回復するまでの数年から数十年間に融解を加速させると報告されている。しかし、こうした急速融解が炭素放出にもたらす加速度的な影響は十分に解明されていない。地球システムモデルでは、気温上昇に伴う一様な永久凍土の融解量は考慮され始めたが、火災や森林伐採による急速融解は融解の程度や分布に統一性がないためパラメーター化が難しい。また、永久凍土の融解は地盤を沈下させ、その変動プロセスと特徴的な地形群はサーモカルストと呼ばれる。こうした地形変化は周辺の生態系や水文環境を変化させ、生活圏では建造物やパイプラインを損壊させるため、極域の住民に密接した問題である。

永久凍土は地下の温度構造を反映しているため光学衛星や航空写真から動態が直視できない。その結果、全球的な融解量の観測が進んでおらず、極域陸圏における炭素放出量の不確実性の一因となっている。面的かつ広範な永久凍土融解の観測という地球物理学的課題に対して、2010年代から合成開口レーダー干渉法（Interferometric Synthetic Aperture Radar: InSAR）による観測が発展した。InSARは二時期のSAR衛星画像から相対的地盤変動量を検出する手法であり、SARは能動型のマイクロ波センサーであるため昼夜を問わず観測でき雲を透過する利点がある。また、地上観測点を必要としないため、頻回な現地観測が困難な極域においても有効である。直視できない地下の永久凍土融解過程を沈下量から観測する発想が革新的であり、アラスカから他の永久凍土分布域へ観測が波及したが、最大の分布域であるシベリアでは観測が進んでいない。

本論文では、世界最大の融解浸食地形（通称“バタガイカ メガスランプ”）がある東シベリア・サハ共和国バタガイ周辺における複数の急速融解事例について、InSARによる地盤変動観測と現地調査を実施した。バタガイカ メガスランプでは70年代に小規模なガリーから浸食が始まり、露頭には約20mに及ぶ地下水の層が露出しており、氷に富む永久凍土層（エドマ層）の分布が見て取れる。バタガイ周辺で発生した森林火災跡地において、以下の3つの異なる視点から急速融解の時空間変化を報告する：(1)2014年火災跡地における火災後2~5年の季節的・経年的融解沈下、(2)2018・19年火災跡地における火災直後の地盤変動、(3)高分解能画像の解析による火災後地盤変動の空間的不均一性の検出と検証。

初めに、ヤナ川対岸の北西の丘陵部で発生した2014年火災跡地における、火災後2~5年間の急速融解事例を報告する。InSARを用いてシベリアで初めて急速融解に伴う地盤変

動を検出した。また、ALOS-2 の干渉画像に SBAS 法という時系列解析を適用し、冬季も含めた季節的・経年的な地盤変動の時空間変化を明らかにした。一般的に、冬季の InSAR ペアは積雪による後方散乱過程の変化により干渉性を失うとされてきたが、本論文では ALOS-2 と独立した Sentinel-1 データを比較し、冬季も有意な変動シグナルを検出可能であることを確認した。これらの結果は、顕著な大陸性気候であるバタガイ周辺の乾燥した積雪をマイクロ波が透過することを示している。また、火災後 2~5 年間の総経年沈下量は、 $3.56 \times 10^6 \text{m}^3$ の地下水の融解流出を示唆している。さらに、季節的な隆起のシグナルは、アイスレンズ形成による凍上理論の premelting dynamics による解釈を試みた。

2018・19 年の火災跡地においては“燃焼直後”の融解過程について報告する。2014 年跡地の先例は、火災発生的前後が ALOS と ALOS-2 の観測運用期間外であり、直後の地盤変動過程が不明だった。また、2018・19 年火災跡地はバタガイカ メガスランプと同一斜面で発生したため、地下水の融解や第二のスランプ地形が発達する可能性がある。上述の 2014 年火災と比較して、どのような地形変化をもたらすかも問題である。Sentinel-1 により検出した季節変化は、火災直後から 2 年目までに季節的な凍上期間が増加したことを示した。また、ALOS-2 により検出した経年変化は、火災跡地における経年的融解沈下の振幅が焼失直後は小さく、一年目以降から卓越したことを示している。一方、沈降の開始前には凍上量そのものが増加していることも分かった。2019 年から計測を開始した現地の融解深データをもとに、これらの変動の時空間変化を解釈した。

最後に、ALOS-2 の高分解能データ (SM1 モード・空間分解能約 3m) によって検出した地盤変動シグナルの空間的不均一性について報告する。2020 年 8 月から実施した SM1 による新規観測の結果、2018・19 年火災跡地における季節変動と経年変動の両方で、空間的に不均一な変動シグナルを検出した。2019 年火災跡地内ではガリー地形と相関する変動シグナルを検出し、2018 年火災跡地では内部に変動域と非変動域の明瞭な境界があることが分かった。これらの空間的に不均一な地盤変動シグナルを検証し、原因を明らかにするため、2021 年 9 月に融解深・土壌水分量の分布を計測し、現時点での解釈について述べた。

バタガイ周辺の 3 つの火災跡地の事例から、火災翌年からの季節的沈下量・凍上量の増加、地下水融解に伴う経年沈下量の増加、火災後~5 年程度での経年沈下の終息を検出し、先行研究による火災跡地の融解過程と定性的に整合していた。変動シグナルと光学衛星画像から計算した燃焼指標や植生指標、標高との相関は見られないが、斜面方向やガリーの有無による相関が見られた。特に、高分解能画像と現地の観測により、定量的には火災跡地内部の変動量に不均一性が大きいことが分かった。融解深と季節変動量に必ずしも相関関係が無いことから、季節沈下量から融解深の直接予測が困難であることを示している。

Abstract

Permafrost thaw can lead to further positive feedback to temperature rising. Deepening the seasonally thawing layer induces microbial decomposition of organic carbon stored for tens of thousands of years. In particular, a localized but deep and drastic thawing at fire scars and deforested areas is called “abrupt thaw.” The abrupt thaw may release more greenhouse gases than the gradual thaw caused by temperature rising. For example, a wildfire burns a surficial organic layer, a heat insulator, increasing summer ground temperature. As a result, abrupt permafrost thaw is accelerated over several years to decades until vegetation recovers. However, the effects of abrupt thaw on carbon release are not fully revealed. Although the gradual thaw has begun to consider in the earth system models, the abrupt thaw is challenging to parameterize because of heterogeneity in the amplitude and distribution. Also, permafrost thaw causes topographic change, such as ground subsidence. The process and its characteristic landforms are called “thermokarst.” Thermokarst affects surrounding ecosystems, hydrological environments, and local infrastructures.

On the other hand, it is difficult to observe permafrost broadly because it is a subsurface thermal structure. Optical satellites and aerial photographs can not see the thawing process directly. Therefore, it causes uncertainty in carbon emissions in the polar terrestrial region. For this important geophysical issue, remote-sensing observation using Interferometric Synthetic Aperture Radar (InSAR) has developed from the 2010s. InSAR is a geodetic method that can detect relative ground displacement from two SAR satellite images. The microwave can penetrate the cloud and observe day and night. In addition, InSAR does not require ground-based observation points; it is also effective in polar regions where frequent field observations are difficult. Owing to the advantages, InSAR observation has spread from Alaska to other regions but has almost no progress in Siberia, the largest permafrost distributed area.

The thesis observed multiple cases of abrupt thaw around Batagay, Sakha Republic, Northeastern Siberia, focusing on the world’s largest retrogressive thaw slump (Batagaika mega-slump). The outcrop of the slump exposes a massive ice layer about 20 meters thick. It indicates the distribution of an ice-rich permafrost layer (yedoma layer). InSAR images detected ground deformations at the fire scars around Batagay, and on-site observations verified the deformation signals. The thesis reports spatio-temporal process of ground deformation and abrupt thaw from three different perspectives: (1) seasonal and annual thaw subsidence at the 2014 fire scar for 2-5 years after the fire, (2) post-fire immediate deformation at the 2018-19 fire scars, (3) detection and verification of spatial heterogeneity of post-fire deformation using ALOS-2 high-resolution images.

The first topic is the 2014 fire scar located on the hills opposite the Yana River. InSAR detected the abrupt thaw process 2-5 years after the fire. Time-series analysis, called the small baseline

subset method (SBAS), revealed the spatio-temporal changes of seasonal and annual ground deformations, including a frost heave in early winter. In general, InSAR pairs in winter lose coherence due to changes in the backscatter process caused by snowpack. By comparing ALOS-2 and independent Sentinel-1 interferograms, this thesis confirmed that consistent deformation signals could be detected even in winter. These results indicated that microwaves could penetrate dry snowpack around Batagay with a pronounced continental climate. The total secular subsidence 2-5 years after the fire suggests that $3.56 \times 10^6 \text{m}^3$ of massive ice melt. Furthermore, the seasonal uplift signal is interpreted by premelting dynamics of heave theory due to ice lens formation.

The second topic is thawing immediately after the 2018-19 fires. The immediate process was unclear at the 2014 scar because the burned year was not included in the ALOS and ALOS-2 observation periods. In addition, the 2018-19 fires occurred on the same slope as the Batagaika mega-slump, which may lead to the melting of massive ice and the second slump in the future. Therefore, we also focused on the difference in the deformation process from the 2014 fire. The Sentinel-1 interferograms detected an increase in the seasonal heave period from the burned year to the second year. The ALOS-2 interferograms detected that the heave signal was dominant in the burned year, and secular subsidence became dominant after the second year of the fire. We interpreted the spatio-temporal variation based on the local thaw depth data measured from 2019.

The third topic is the spatial heterogeneity of ground deformation signals detected by the high-resolution ALOS-2 data. InSAR images detected spatially heterogeneous signals in both seasonal and annual deformation within the 2018-19 fire scars. The seasonal heave signals correlated with gully topography in the 2019 fire scar. On the other hand, within the 2018 fire scar, there are clear boundaries between well-deformed and non-deformed areas. In order to verify these spatial heterogeneities and clarify their causes, we conducted the on-site observation in September 2021 and measured the distribution of thaw depth and soil water content. This chapter reports the preliminary interpretation from InSAR and on-site data.

To summarize the three cases of fire scars, the thesis found an increase in seasonal and annual deformation amplitude from the following year of the fires and an end of annual subsidence about ~5 years after the fire. These processes are qualitatively consistent with previous reports. The spatial pattern of deformation is not directly related to the elevation, the burn severity, and the vegetation index derived from the optical satellite images. Instead, the deformation is related to the slope direction and the presence of a gully. In particular, high-resolution InSAR images and on-site observations quantitatively revealed spatial heterogeneity in the deformation amount within the fire scars. Furthermore, no correlation between the thaw depth and the heterogeneity suggests that it is challenging to predict thaw depth directly from seasonal subsidence.

List of Abbreviations

Abbreviation	Meaning
°C	Temperature in degree Celsius
ALDS	Active Layer Detachment Slide
ALOS	Advanced land observing Satellite
ALOS-2	Advanced Land Observing Satellite 2
ALT	Active Layer Thickness
B-perp	Perpendicular Baseline
CALM	Circumpolar Active Layer Monitoring
DEM	Digital Elevation Model
dNBR	Delta NBR
ESA	European Space Agency
FIRMS	Fire Information for Resource Management System
GIS	Geographic Information System
InSAR	Interferometric SAR
IR	Infra-Red
ISRO	Indian Space Research Organisation
IW	Interferometric Wide swath
JAXA	Japanese Aerospace Exploration Agency
LOS	Line of Sight
MMAT	Monthly Mean Air Temperature
MODIS	Moderate Resolution Imaging Spectroradiometer
MP	Monthly Precipitation
NASA	National Aeronautics and Space Administration
NBR	Normalized Burn Ratio
NDVI	Normalized Difference Vegetation Index
NIR	Near-InfraRed
PALSAR	Phased Array Type L-band Synthetic Aperture Radar
PALSAR-2	Phased Array Type L-band Synthetic Aperture Radar 2
QGIS	Quantum GIS
RDC	Range Doppler Coordinates
RTS	Retrogressive Thaw Slump
SAR	Synthetic Aperture Radar
SBAS	Small Baseline Subset
SLC	Single Look Complex
SM	Strip Map
SOC	Soil Organic Carbon
SWC	Soil water Content
SWIR	Short-Wavelength InfraRed
TTOP	Temperature of Top Permafrost
VIIRS	Visible Infrared Imaging Radiometer Suite
WMO	World Meteorological Organization

List of Figures

Figure 1-1.	Permafrost distribution map of the northern hemisphere and East Siberia.	2
Figure 1-2.	Soil organic carbon map of the permafrost zone in the northern hemisphere.	4
Figure 1-3.	Schematic image of thermokarst lake and basin.	9
Figure 1-4.	The map of Sakha Republic and around Batagay.	12
Figure 1-5.	An overview of fire scars and permafrost terrain around Batagay.	15
Figure 1-6.	Workflow of the analysis.	16
Figure 1-7.	The map of NBR and dNBR around Batagay.	19
Figure 1-8.	Schematic image of SAR geometry.	21
Figure 1-9.	The geometry of Interferometric SAR.	23
Figure 1-10.	Conceptual images of coherence.	25
Figure 2-1.	Satellite imaging areas in Chapter 2.	35
Figure 2-2.	Schematic diagram of data time series.	43
Figure 2-3.	Temporal distribution of interferograms for the time-series analysis.	45
Figure 2-4.	Seasonal deformation at the 2014 fire scar detected by ALOS-2 and Sentinel-1 (stacked) interferograms.	48
Figure 2-5.	Differences in LOS-change detected by ALOS-2 and Sentinel-1 seasonal interferograms.	50
Figure 2-6.	Sentinel-1 interferograms during the 27 periods from June 2017 through June 2018 at the 2014 fire scar.	51
Figure 2-7.	Annual deformation at the 2014 fire scar detected by ALOS-2 interferograms.	52
Figure 2-8.	Cumulative LOS changes from 2015 to 2019 estimated by InSAR time-series analysis.	54
Figure 2-9.	Temporal LOS change at the point A-D in Figure 2-8.	55
Figure 2-10.	Non-dimensional heave rate profiles of an ice lens as a function of its boundary position.	61
Figure 2-11.	Map and pictures about on-site observation at the 2014 scar in 2019.	64
Figure 2-12.	Thaw depth data taken in the 2014 scar.	66
Figure 3-1.	Satellite imaging and fire scars area in Chapter 3.	70
Figure 3-2.	On-site observation areas in Chapter 3.	72

Figure 3-3.	Frost heave maps derived from stacked Sentinel-1 interferograms.	74
Figure 3-4.	Sentinel-1 InSAR images before stacking in 2018-2019.....	77
Figure 3-5.	Sentinel-1 InSAR images before stacking in 2019-2020.....	78
Figure 3-6.	Sentinel-1 InSAR images before stacking in 2020-2021.....	79
Figure 3-7.	Annual deformation at the 2018 and 2019 fire scars detected by ALOS-2 interferograms.....	80
Figure 3-8.	Coherence of one-year pairs of ALOS-2 interferograms.	82
Figure 3-9.	Temporal change of thaw depth at the burned and the adjacent unburned sites.	83
Figure 3-10.	Comparison of LOS displacement detected by ALOS-2 and Sentinel-1 in the nearly same period.	85
Figure 3-11.	Real color and NDVI images derived by Sentinel-2 image.....	87
Figure 3-12.	Temporal change of ADDT and ADDF at Batagay in September 2018-2021.	88
Figure 4-1.	Study and ALOS-2 imaging area around the 2018 and 2019 fire scars.	94
Figure 4-2.	Overview of the ALOS-2 SM1 InSAR images around the fire scars.	96
Figure 4-3.	ALOS-2 SM1 InSAR images around the gully in the 2019 fire scar.	98
Figure 4-4.	ALOS-2 SM1 InSAR images around the displacement boundary in the 2018 fire scar.	99
Figure 4-5.	Network of InSAR images for SBAS time series and cumulative estimated LOS change.....	100
Figure 4-6.	Time series of estimated LOS change in SBAS analysis.....	101
Figure 4-7.	The map of field measurement and thaw depth and SWC profile across the 2019 fire scar's gully.	103
Figure 4-8.	The map of field measurement and thaw depth and SWC profile in the 2018 fire scar.	103
Figure 4-9.	The vertical profile of temperature and SWC at the pits along the transect of the gully.	105
Figure 4-10.	Phase closures for all combinations of the interferograms.	108
Figure 4-11.	dNBR, true-color, and NDVI values in the 2018 fire scar.	109
Figure 4-12.	Elevation and slope topography in the 2018 fire scar.	111
Figure 8-1.	The pictures of pits at the transect of the gully.	139

List of Tables

Table 1-1. The average value (1991-2020) of MMAT and MP at Verkhoyansk.	12
Table 8-1. Data list of ALOS-2 for interferograms in Figures 2-4 a-e and Figure 2-7.	133
Table 8-2. Data list of Sentinel-1 for interferograms in Figures 2-4 f-j and 2-6.	134
Table 8-3. Data list of ALOS-2 for interferograms in Figures 3-4.	135
Table 8-4. Data list of Sentinel-1 for interferograms in Figures 3-3.	135
Table 8-5. Data list of ALOS-2 SM1 interferograms in Chapter 4.	138

Chapter 1

General Introduction

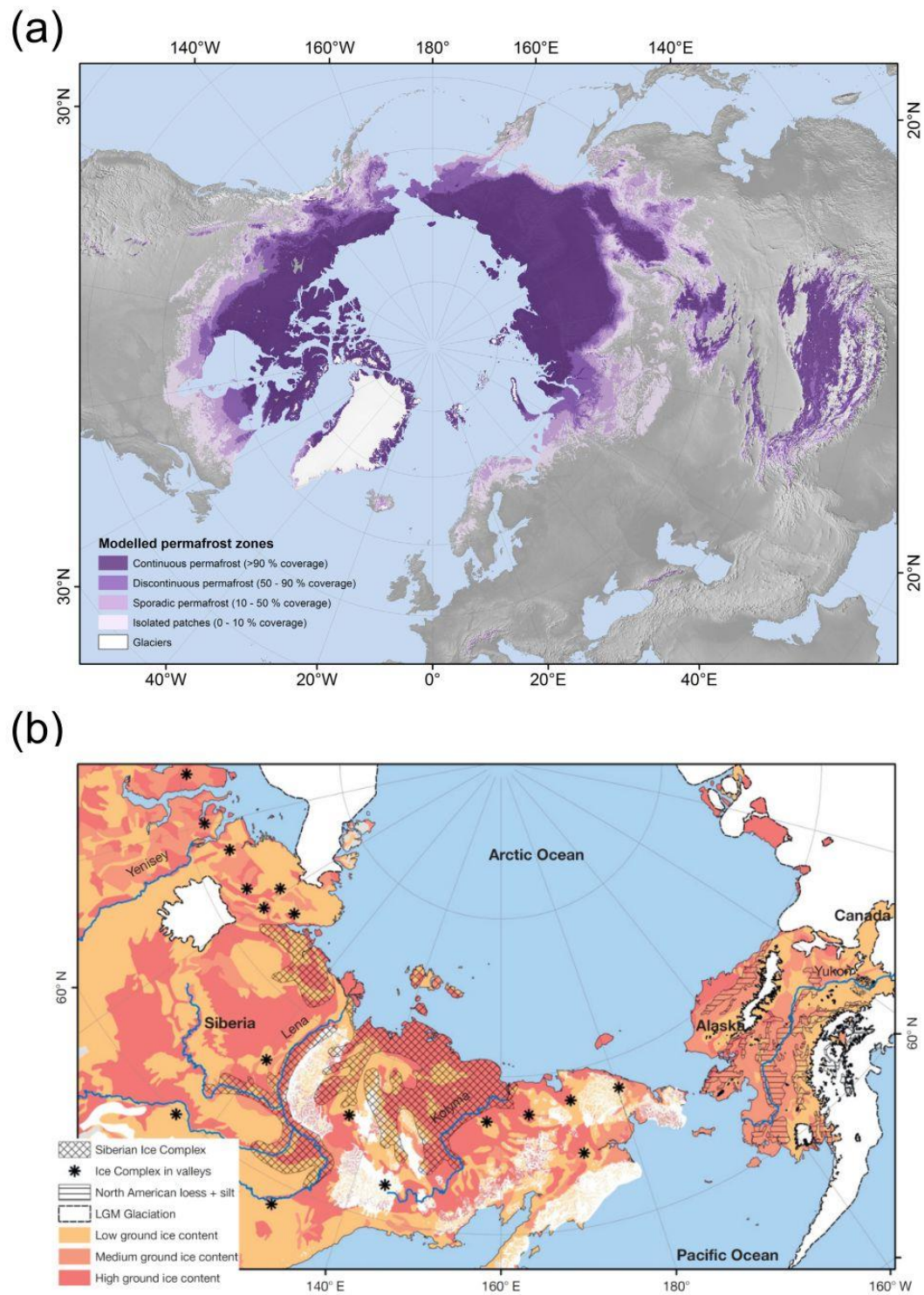


Figure 1-1. (a) Permafrost distribution map in Northern hemisphere derived with TTOP model from Obu et al. (2019). (b) Distribution of ice-rich permafrost and ground ice content in Arctic and Subarctic lowlands from Schirrmeister et al. (2013).

Chapter 1. General Introduction

1.1 Permafrost

1.1.1 Definition and distribution

Permafrost is thermally defined as "ground that remains at or below 0°C for at least two consecutive years" (Harris et al., 1988; French, 2007). It is widely distributed as a periglacial phenomenon in the polar and alpine zones. Broun et al. (1997) presented the first map of permafrost distribution consistently in the entire Northern Hemisphere. Obu et al. (2019) updated the map with the 'temperature of top permafrost (TTOP) model' on the spatial scale of a 1 km² grid (Figure 1-1a). TTOP is calculated by air temperature index of thawing/freezing, air temperature-surface thermal offset, and heat transfer offset from surface to the top of permafrost table. TTOP below 0°C is defined as permafrost distributed area, and it exists in 21.8% of the exposed land area in the Northern Hemisphere. According to the extent, permafrost can be classified into continuous (>90%), discontinuous (90-50%), sporadic (50-10%), and isolated zone (<10%). Siberia, the largest permafrost distribution area in the world, is mostly occupied by continuous permafrost.

Permafrost is defined as not a constituent but a thermal condition; thus, it contains organic matter, sediment, bedrock, and ice. Ice-rich permafrost, which consists of a sediment layer with high ice content, plays an essential role in permafrost thawing and topographic changes. In Siberia, such ice-rich permafrost is also called 'Ice Complex' and 'yedoma.' In the area unglaciated by the late Pliocene and Pleistocene called Beringia, the yedoma and subsurface ice has been developed in a broad area (Schirrmeister et al., 2013; Fedorov., 2018). Figure 1-1b shows the distribution of yedoma and ground ice around Siberia. These distribution maps are based on existing geological, soil, and vegetation maps and optical satellite data. However, permafrost and ground ice are subsurface structures and cannot be visually confirmed from the ground. Broad observation by satellite remote sensing is difficult compared to other cryosphere environments such as glaciers, ice sheets, and sea

ice. Hence, monitoring and understanding the immediate dynamics of permafrost over the entire globe is challenging.

1.1.2 Positive feedback to global warming

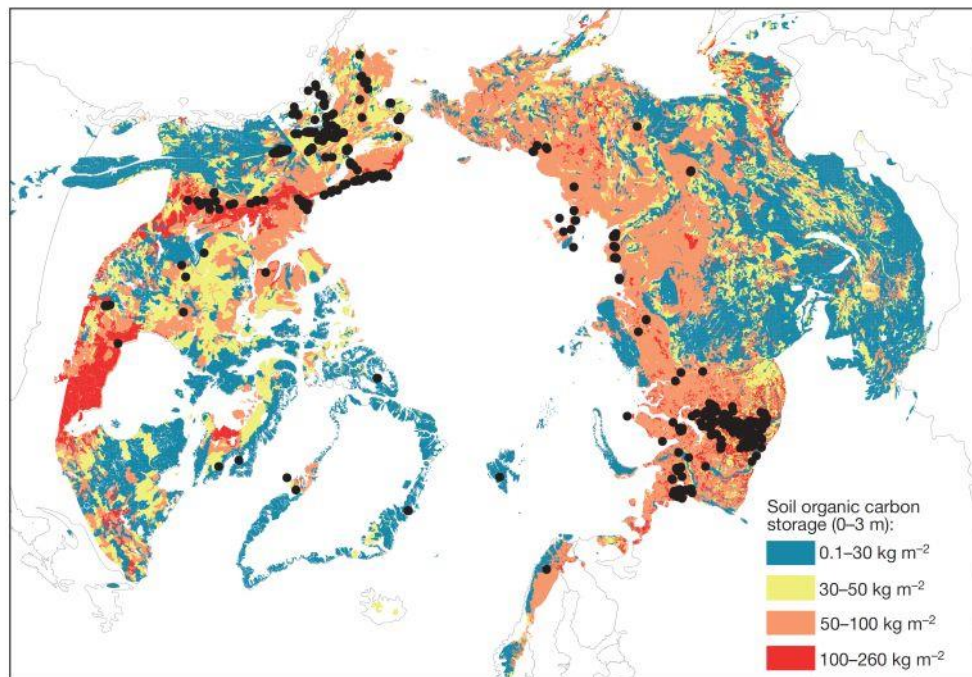


Figure 1-2. Soil organic carbon storage in the 0-3 m depth of the northern circumpolar permafrost zone from Schuur et al. (2015).

The vast permafrost area stores soil organic carbon (SOC) twice as much atmospheric carbon because organic carbon from past biological sources is frozen and not decomposed (Figure 1-2). Tarnocai et al. (2009) estimated the 1672 Pg of SOC is stored in the ground with 0-300 depth and in deltaic deposits and Siberian yedoma sediments in the northern permafrost region. This amount is about half of the global belowground organic carbon. Hugelius et al. (2014) estimated SOC, including quantitative uncertainties, and estimated the amount of SOC in the northern permafrost zone to be 1140-1476 Pg. They mentioned that the soil pedon database used for model estimation is based on

limited observational data and regional gaps cause the uncertainty. Olefeldt et al. (2016) suggest that about half of the organic carbon in these permafrost zones is concentrated and distributed in thermokarst terrain (details in the next chapter).

The active layer thickness (ALT) is defined as the maximum depth of 0°C isotherm or the maximum annual thaw depth (Burn, 1998). Deepening ALT can cause positive feedback to global warming; newly decomposed organic carbon in the deepened active layer is being released into the atmosphere, leading to further permafrost thaw due to rising temperature. Organic carbon is decomposed to carbon dioxide (CO₂) under aerobic conditions and methane (CH₄) under anaerobic conditions like thermokarst lake bottoms. Schuur et al. (2015) estimated that 5~15% of the carbon pool in terrestrial permafrost would be released during this century, although some uncertainty remains. If it is released as CO₂, it will be far less than the amount released by fossil fuels. However, they concluded that if it is released as CH₄, it could have much larger feedback, and the release is not pulsed and short-term but a constant and long-lasting release with further permafrost thawing.

Such permafrost thaw has a complexity of interactions with other climate and geomorphological factors as well as temperature increases. For example, fires release soil organic matter through combustion (Mack et al., 2011), which also accelerates the thawing of the underlying permafrost after burning (Yoshikawa et al., 2003). Also, thawing permafrost directly impacts lake and stream systems, leading to water-mediated material cycles (Vonk et al., 2015). Changes in hydrological conditions lead to changes in organic matter decomposition rates, aerobic-anaerobic conditions, and soil dryness, contributing to uncertainty in carbon release estimates (Walter et al., 2008; Lawrence et al., 2015). In addition, there is also the storage of mercury, which has raised concerns about its potential to affect the global mercury cycle (Schuster et al., 2018). In summary, the increased ALT can cause

positive feedback on rising temperature and gradual but certain spatial expansion of the material circulation field.

1.1.3 Permafrost thaw and topography change

In general, there is a positive correlation between air temperature increase and active layer thickness (ALT) and previous field measurements support the relationship (Shikolomanov and Nelson, 2002; Hinkel and Nelson, 2003). In order to estimate ALT as a function of air temperature, the empirical law named the Stefan equation has traditionally been used, as follows (Nelson et al., 1997; Klene et al., 2001; French, 2007):

$$Z(t) = \sqrt{\frac{2k_t S \{n_t ADDT_a(t)\}}{\rho \theta L}}, \quad (1.1)$$

where

k_t is the thermal conductivity of the melted soil (W/mK),

S is the scaling factor of time (86,400s/days),

$ADDT_a(t)$ is the accumulated degree days of thaw calculated from air temperature (K·days),

n_t is the ratio of air temperature to ground surface temperature, called n-factor,

ρ is the soil density (kg/m³),

θ is the volumetric water content ratio,

L is the latent heat of melting (J/kg).

The coefficients of soil conditions and some factors can be simplified as follows:

$$Z(t) = E \sqrt{ADDT_a(t)}, \quad (1.2)$$

where E is the constant value ($\text{m}^2/\text{K}\cdot\text{days}$)^{1/2}. For example, Hinkel and Nelson (2003) reported a positive correlation between ALT and temperature change for each year observed at the Circumpolar Active Layer Monitoring (CALM) site on the Alaska North Slope during 1995-2000.

On the other hand, Shikolomanov et al. (2013) pointed out that the relationship between ALT and temperature should be discussed considering the amount of isotropic thaw subsidence. They reported that with increasing ALT, soil consolidation and interannual isotropic subsidence occurred uniformly due to the thawing of the transition layer, which is an intermediate layer from the lower boundary of AL to the upper bound of the long-term permafrost table. The transition layer thaws at intervals of tens to several hundred years, and the stability of the underlying permafrost can be discussed with the development of its internal ice (e.g., ice lens; ice wedge) (Shur et al., 2005; Ishikawa and Saito, 2006). Especially in ice-rich permafrost regions, they also suggest that isotropic subsidence progresses while the ALT remains constant. Wagner et al. (2018) used artificial heaters to thaw permafrost in the interior region of Alaska. They observed subsidence of about 10 cm with a one-meter increase of ALT. They suggested that the heterogeneity of the deformation is associated with the spatial gradient of ice content in the transition layer. In summary, with a spatially wide range, temperature rising leads to (1) an increase of the ALT and (2) isotropic subsidence due to thawing of the transition layer, and ice content in the layer would affect the amount of subsidence.

On the narrow scale, ice-rich permafrost thawing may proceed spatial selectively due to the effects of surface disturbance, microtopography, and vegetation. Such local-scale thawing processes and resulting characteristic landforms are called thermokarst. Thermokarst has been classified into more than a dozen types according to their formation process and topography (Jorgenson and Osterkamp, 2005; Jorgenson, 2013; Kokelj and Jorgenson, 2013). On the plains, Thermokarst Lake is formed in depression by lateral thermomechanical erosion (Figure 1-3). Running off lake water due to

thawing of underlain permafrost layer makes depression called “thermokarst basin” or “alas.” On the slope, thawing of the transient layer causes a landslide called 'active layer detachment slide (ALDS). A retrogressive thaw slump (RTS) is a thermally eroded terrain caused by the melting and collapse of the massive ice exposed on the headwall. The Batagay, the study site of this thesis, has the world's largest RTS and continues to expand 50 years after its occurrence (see Chapter 1.1.5 for details).

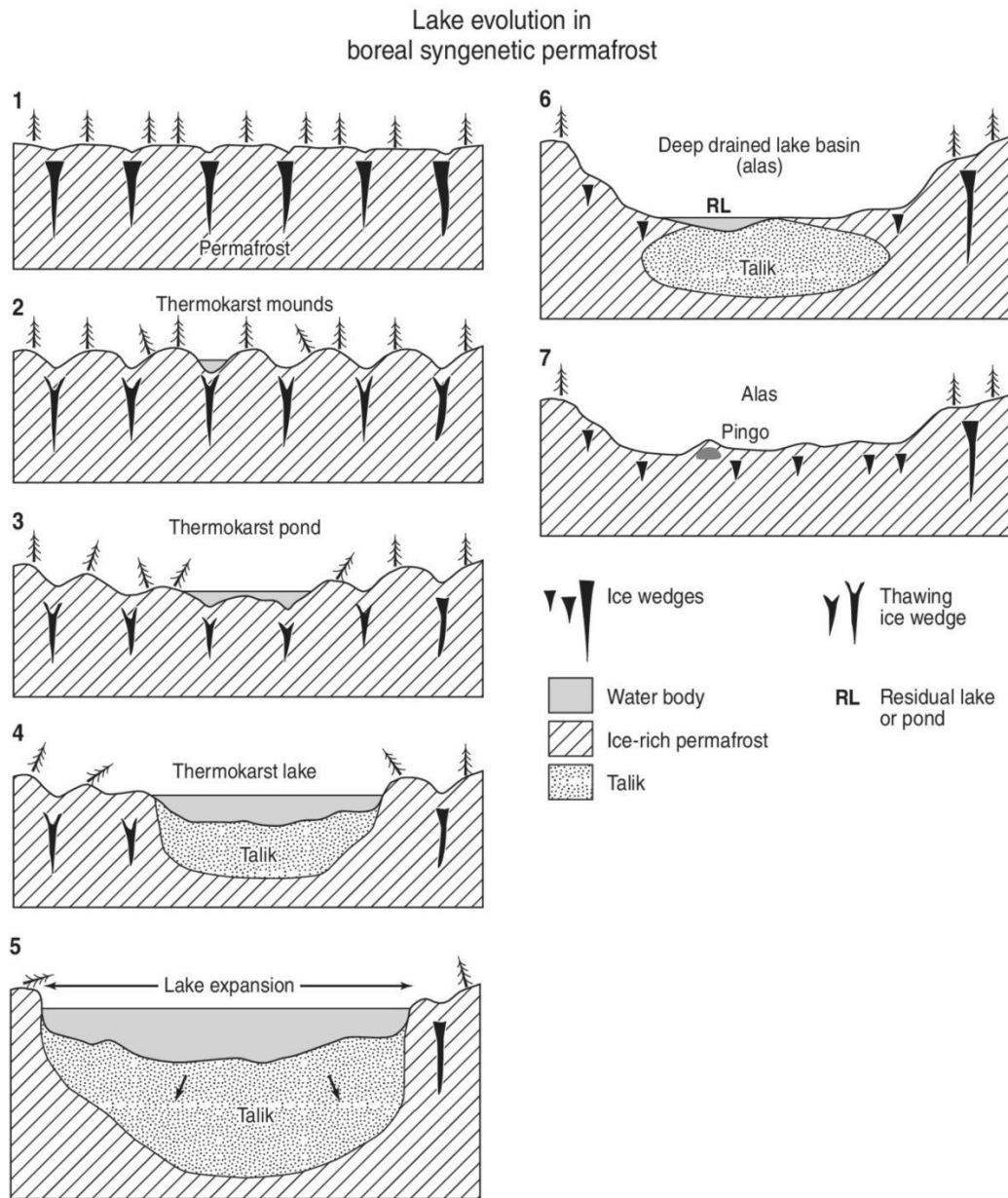


Figure 1-3. Schematic image of thermokarst lake and drained lake basin in the boreal syngenetic permafrost area. Modified after Ballantyne and Murton (2018).

The rising temperature and climate change have also accelerated these thermokarst processes. For example, Kokelj et al. (2015) observed slump expansion from Landsat optical images in the Peel Plateau, Canada, and concluded that extreme rainfall events accelerated the expansion.

Lewkowicz and Way (2019) visually detected the initiation and longevity of RTS on Banks Island, Canada, using the Google Earth Engine Timelapse dataset from 1984 to 2016. They concluded that RTS in 2013 (more than 4000) increased by about 60 times compared to 1984 (only 64 actives). The number of occurrences increased concerning the four extreme summer high-temperature events. In order to observe the spatio-temporal changes of the accelerating thermokarst process, satellite remote sensing has been used with conventional field observations. In particular, Interferometric Synthetic Aperture Radar (InSAR), which can detect relative ground displacement on the centimeter scale, has contributed for (details in Chapter 1.2.3).

1.1.4 Abrupt permafrost thaw

The permafrost thaw caused by localized disturbance (e.g., wildfires, deforestation, thermokarst) is called abrupt thaw or rapid thaw, in contrast to the spatially uniform gradual thaw caused by rising temperatures. Abrupt thaw occurs only at point locations but can reach depths of several tens meters. As it has a high regionality, the abrupt thaw is not included in large-scale model projections of climate change (Schuur et al., 2015). So, it has been noted to lack significant complexity of permafrost dynamics. Turetsky et al. (2020) compared carbon emissions from the gradual and abrupt thaw. They noted that abrupt thaw leads to climate-feedbacks about seven times greater than gradual thaw, although using a simple inventory model. Anomalous summer temperatures in the Arctic in 2020 and increased carbon emissions from wildfires would accelerate further abrupt thaw (Natali et al., 2021). There is a need for an urgent understanding of the abrupt thaw amount. The IPCC AR6 report describes that gradual thaw due to temperature rising is considered in recent carbon release models but points out that abrupt thaw is not well understood globally.

One of the drivers of abrupt thaw, wildfires accelerate thawing on timescales ranging from years to decades after the burning. Yoshikawa et al. (2003) observed surface organic matter, soil water

content, and albedo, which could be the causes of post-fire permafrost thawing at wildfire scars in the discontinuous permafrost zone of interior Alaska. Although albedo is reduced by exposed soil and combusted organic matters, its effect is relatively small than other factors. Soil water content, which increases soil thermal conductivity, increases short-term immediately after a fire but does not last long-term due to increased ALT and vegetation recovery. They suggested that the primary cause of long-term post-fire thawing was the loss of the surface organic layer, which acts as a heat insulator.

Holloway and Lewkowicz (2019) measured thaw depths at transects installed in 1962 along the Mackenzie Highway in Canada and noted permafrost thawing conditions at burned and unburned sites. The ALT increased at the fire scar in most cases, but the permafrost layer was retained if thick enough (> 50 cm) organic material remained on the surface. In other words, it is clear that both disturbance and recovery of permafrost are closely related to the presence of organic material at the surface after the fire. Abrupt thaw naturally leads to localized and severe topographic changes. The development of ice-wedge polygons and RTS has been observed by satellite imagery and LiDAR after the fire in the Alaskan tundra region (Jones et al., 2015; Iwahana et al., 2016a). Recently, thaw subsidence has been observed in fire scars in various regions in studies using InSAR, which has been validated for ground motion detection by thermokarst (see Chapter 1.2.3 for details).

1.1.5 Study site: Batagay, Sakha Republic, Northeastern Siberia

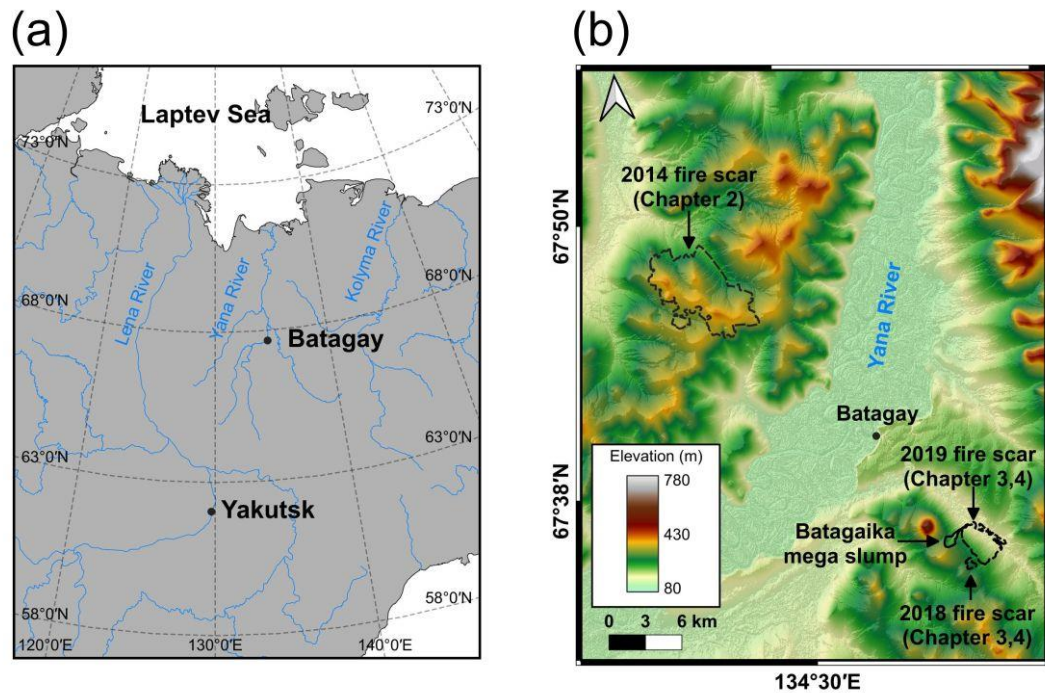


Figure 1-4. (a) Overview of Sakha Republic. (b) Map of the study sites around Batagay with shaded relief. The color indicates the elevation value of ArcticDEM.

This thesis targets wildfire scars near Batagay village in the Republic of Sakha, Northeastern Siberia. Batagay is located at 67°39'N, 134°38'E, about 650 km north of Yakutsk, the capital of the Republic of Sakha. This region is the continuous permafrost zone, and the climate is a representative continental climate, with a large temperature difference of 61.2°C (January-July). This is because the Siberian anticyclone dominates in winter, and the Southwest Asian cyclone dominates in summer. Table 1-1 shows the monthly mean air temperature (MMAT) and monthly precipitation (MP) at Verkhoyansk, 55 km west of Batagay. The Japanese Meteorological Agency archives the CLIMAT data observed by each country. The values were averaged observed data taken from 1991 to 2020. The press release from the World Meteorological Organization (WMO) reported that the daily maximum

temperature of 38°C was recorded at Verkhoyansk in June 2020. It is provisionally the highest known temperature in the north of the Arctic Circle.

In addition, the extent and frequency of fires have been increasing in recent years. Large fires have occurred around the Batagay at intervals of several years, with the most recent event in 2019 and 2020. For example, within the 44,000 km² image area around Batagay, the estimated burned area in 2019 and 2020 are 4,000 and 3,500 km², respectively, while the area in 2018 is 550km². Narita et al. (2021), based on statistical data from the government of the Republic of Sakha in 1999-2017, reported that dry thunderstorms caused 51% of the fires, and human factors such as mismanagement bonfires caused 34%. A dry thunderstorm is a thunderstorm with little or no rainfall at the ground surface. Rain evaporates under extremely dry conditions before it downfalls the ground, promoting lightning-caused fires.

Table 1-1. The average value (1991-2020) of MMAT and MP at Verkhoyansk.

	Jan.	Feb.	Mar.	Apr.	May	Jun.	Jul.	Aug.	Sep.	Oct.	Nov.	Dec.
MMAT (°C)	-44.7	-42	-28.6	-10.7	4.1	14	16.5	12.2	2.9	-13.2	-33.7	-43.5
MP (mm)	5.9	5.4	4.6	4.1	14.9	29.7	35.1	28.6	20.3	12.8	11.3	6.3

This area is located in the taiga zone, and there are floodplains of the Yana River and hills around Batagay. The vegetation is a boreal forest consisting mainly of larch, with other forests such as birch, alder, willow (Ashastina, 2018). The ground surface is covered with meadows such as grasses and lingonberry and mosses such as sphagnum as a surficial organic mat. In higher areas with elevations of 500-900 m, shrubs such as stone pine dominate. Figure 1-5 is the overview of the fire scars around the Batagay and the Batagaika mega slump in 2019-2021. The larch forest has remained

at the 2014 fire scar (Figure 1-5a), but the surficial organic mat had been burned away and did not recover entirely even five years after the fire. The 2014 fire scar locates on the opposite side of the Yana River, where there are no steady living people. Therefore, there is no trace of artificial extinguishing around the fire scar. On the other hand, the 2018 fire scar is surrounded by artificial firebreaks. This is because the local people stopped the expansion of the fires by excavating the ground surface. The 2018 fire scar has had many downed larches and lost organic mats. The 2019 fire site has remained larch but no organic mat as well. It was also surrounded by a firebreak built on the upper (westernmost) side of the slope, and the other boundaries are gullies and the Batagai River on the lower side of the slope. In the lower part of the slope near the Batagay River, meadows dominate instead of larches, and there are ice wedge polygons.

The world's largest RTS, called Batagaika mega slump, is located on the hillslope 10 km southeast of the village (Fig. 1-6h-g). Kunitsky et al. (2013) described the slump formed by a small gully in the 1970s and confirmed gradual expansion with optical images. In 2019, the length reached 1.8 km, and the width reached up to 0.8 km. The highest headwall is about 90 m, with upper sand layers from the surface to 20-30 m depth and a subsurface ice complex layer from 20 to 45 m (Murton et al., 2017 and 2021). The slump indicates subsurface yedoma and massive ground ice and vulnerability to topographic change due to abrupt thawing in the region. Indeed, we confirmed that massive ground ice was exposed on the flanks of gullies adjacent to the 2018 fire scar (Figure 1-5i). An abrupt thaw and further erosion in the environment may trigger a second mega slump.

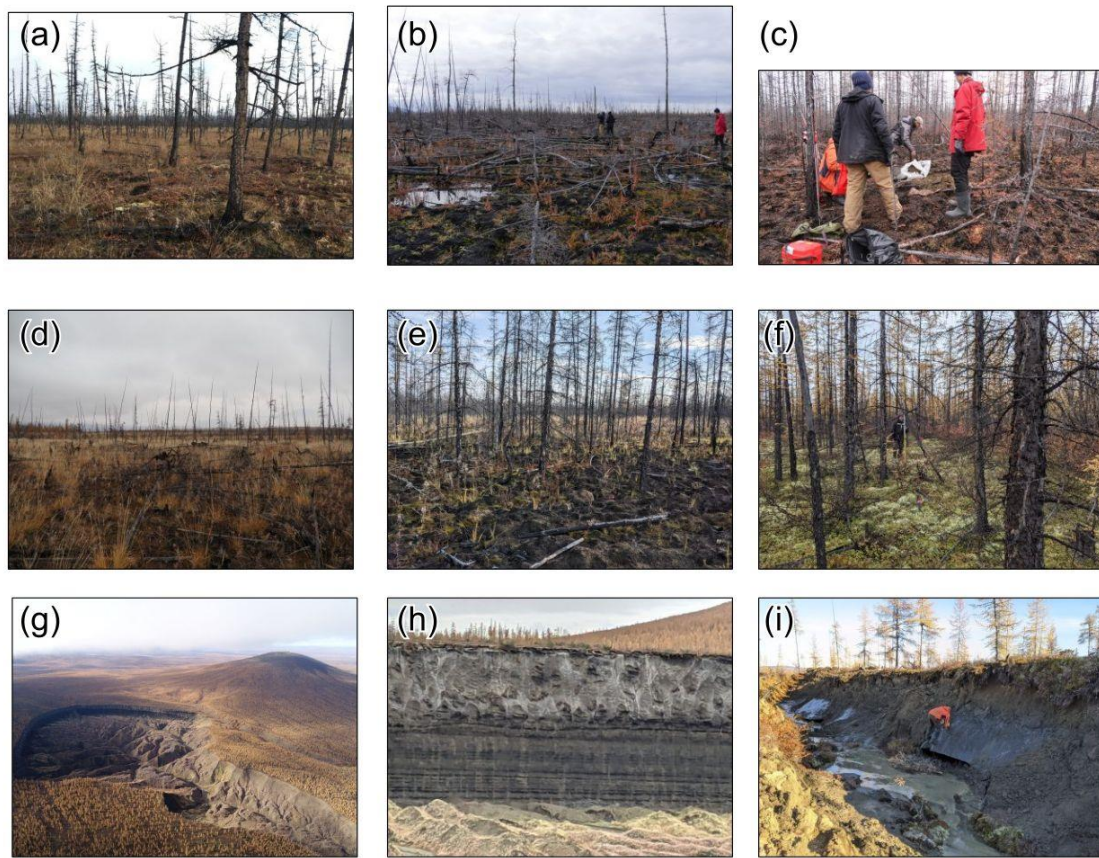


Figure 1-5. An overview of fire scars and permafrost terrain at Batagay. (a) The 2014 scar 5-years after the fire. (b) The 2018 scar next year of the fire. (c) The 2019 scar immediately after burning. (d) The 2018 scar 3-years after the fire. (e) The 2019 scar 2-years after the fire. (f) Unburned control site next to the 2019 scar. (g) Aerial views of the Batagaika mega slump. (h) Yedoma ice complex exposed on the southwest headwall of the slump. (i) Massive ground ice exposed on a gully near the 2018 scar. Picture (c, g) and (b, f) were taken by Nikolai Fedorov and Go Iwahana, respectively. Picture (a), (b,c), (d), (e), (f) and (g-i) were taken on 21 September 2019, 22 September 2019, 18 September 2021, 16 September 2021, 17 September 2021 and 21 September 2021, respectively.

1.2 Space geodetic technique for permafrost observation

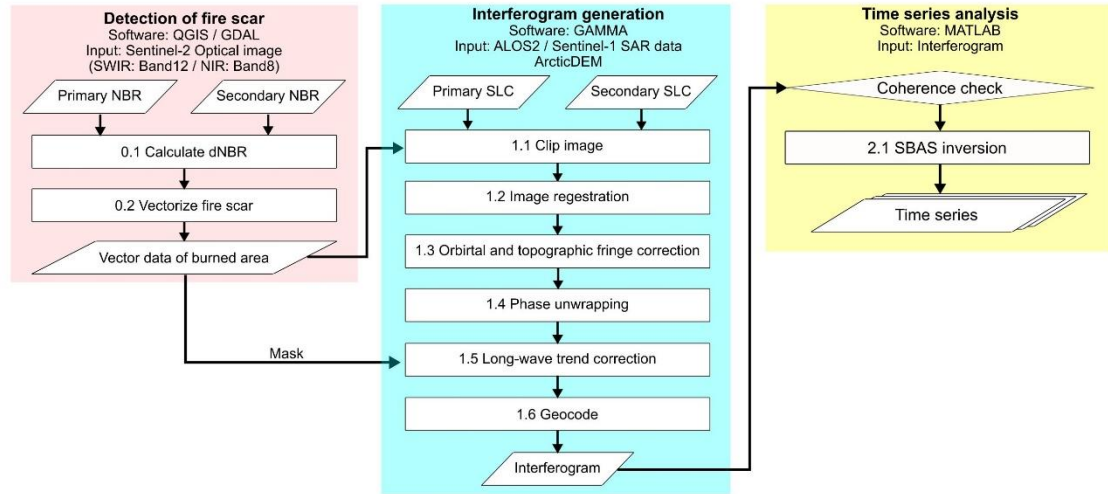


Figure 1-6. Workflow of the analysis; detection of burned area (step0), making interferogram (step1), and time series analysis (step2).

The analysis of ground deformation mapping (Chapter 2,3,4) consists of three steps: (1) Identification of the fire scar using optical images; (2) Generation of interferograms around the fire scar; (3) Time series analysis using interferogram with high temporal coherence (Figure 1-6). In the first step, we calculate NBR from the NIR and SWIR data of Sentinel-2. Then we calculate dNBR by taking a difference of NBR between before and after a fire. Finally, we assume that the fire scar showed a severe burn index (>0.27) and vectorize the data. In the second step, we make an interferogram from the SLC image clipped around the fire scar identified in the first step. The interferogram used in this study is corrected the long-wavelength phase trend with a quadratic polynomial estimation. At the estimation, the vector data of the fire scar is used to mask the phase changes. Interferograms with high temporal coherence, mainly made from ALOS-2 data, were used for time series analysis to reveal the spatio-temporal deformation process. On the contrary, interferograms with low temporal coherence, mainly made from Sentinel-1 data, were stacked to discuss the deformation in the arbitrary period.

An overview and the principles about fire scar detection with optical imagery (Chapter 1.2.1), synthetic aperture radar (Chapter 1.2.2), and interferometric SAR and time series analysis (Chapter 1.2.3) were summarized in the following sections.

1.2.1 Fire scar detection with optical data

The Moderate Resolution Imaging Spectroradiometer (MODIS) onboard NASA's Terra and Aqua satellites and the Visible Infrared Imaging Radiometer Suite (VIIRS) onboard Suomi-NPP and NOAA-20 satellites are mainly used for remote sensing of fire signal detection. In general, the difference in sensitivity to brightness temperature in multiple infrared channels detects the fire signal (Justice et al., 2002). The fire products acquired by these sensors are archived in the Fire Information for Resource Management System (FIRMS, [<https://firms.modaps.eosdis.nasa.gov/>]) developed by the University of Maryland in 2007 (Davies et al., 2009). Since the products are made from multiple satellites data, the temporal resolution is high, and it is very effective to understand immediately where the fire occurred. However, it is impossible to accurately identify the burned area because the spatial resolution is 1 km. In particular, in order to create a mask for the interferogram, it is necessary to identify the burned area with a spatial resolution of several tens of meters.

In contrast, another method has been reported to estimate the burn severity defined as Normalized Burn Ratio (NBR) by using the higher spatial resolution (tens of meter) optical satellites such as the Landsat (Key and Benson, 2006; Escuin et al., 2008). Fire decreases reflectance in the near-infrared (NIR) band, whereas fire increases reflectance in the shortwave infrared (SWIR) band. The principle is similar to the Normalized Difference Vegetation Index (NDVI), which indicates spatio-temporal changes in surface vegetation (Lillesand, 2007). NBR and NDVI are expressed as;

$$NBR = \frac{NIR - SWIR}{NIR + SWIR} , \quad (1.3)$$

$$NDVI = \frac{NIR - R}{NIR + R}, \quad (1.4)$$

where R represents the visible red band. NBR can be calculated as delta NBR (dNBR) by taking the difference between the same period before and after the fire and can be expressed as;

$$dNBR = NBR_{prefire} - NBR_{postfire}. \quad (1.5)$$

This study calculates NBR using band 8a (center frequency: 865 nm) and band 12 (center frequency: 2190 nm) of the Sentinel-2 satellite to estimate the extent and severity of fire around Batagay. The spatial resolution of these two bands is 20m, which is reasonable to the spatial resolution of InSAR images.

On the other hand, we want to mask the fire scars when estimating the long-wavelength phase trend on an interferogram. In particular, when creating wide-range interferograms such as the full scene of Sentinel-1, we need data that semi-automatically indicate the fire extent in the range of hundreds of kilometers. For this reason, we also create a dataset that simply shows only the burned area. The approach is as below (Figure 1-7).

- (1) Combine multiple Sentinel-2 raw data to include the SAR imaging range and calculate the NBR.
- (2) Create multiple dNBR data of two independent pairs of early thaw season (June) and late thaw season (September).
- (3) Classify the moderate burn severity area ($dNBR > 0.27$) and unburned area and add up the burned area of the two pairs.
- (4) Mask out clouds and their shaded areas defined as extremely low and high reflectance in SWIR and spatially small signals that could not be distinguished from noise ($> 0.05 \text{ km}^2$).
- (5) Vectorize the burned area and visually check the extent with true-color images.

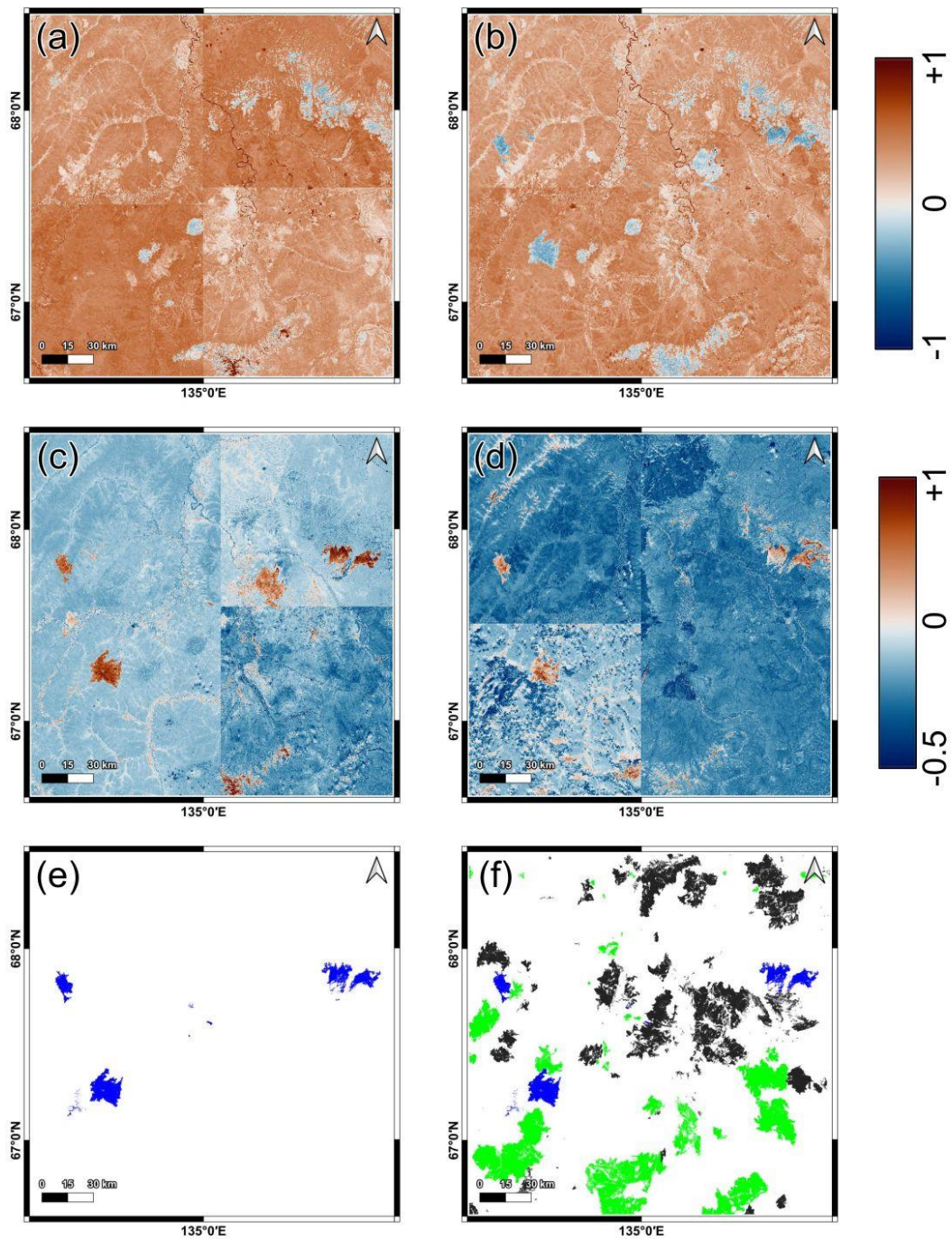


Figure 1-7. (a,b) NBR derived from four Sentinel-2 data taken in June 2018 and 2019, respectively. (c) dNBR calculated from June pair (a,b). (d) dNBR calculated from NBR in September 2017 and 2018. (e) 2018 fire scars around Batagay (dNBR > 0.27). (f) Fire scars from 2018 to 2020. Blue, black, and green areas indicate 2018, 2019, and 2020 fire scars, respectively.

1.2.2 Synthetic Aperture Radar

Synthetic Aperture Radar (SAR) is an active microwave radar generally onboard satellite or aircraft (Ouchi, 2004, 2013). SAR emits microwaves for diagonally downward direction and receives backscatter waves from the ground surface. It is impossible to distinguish observation points equidistant from the radar symmetrically if the radar emits directly under itself. Since SAR emits microwaves while moving, a synthetic aperture that is virtually longer than a real aperture can be made with frequency modulation by the Doppler effect. It can improve the resolution in the satellite flight direction (azimuth direction). In the case of a single aperture, the resolution in the azimuth direction (δ_a) can be expressed as;

$$\delta_a = \frac{\lambda R}{D_a}, \quad (1.6)$$

where λ is microwave wavelength, R is the distance of slant range, D_a is the diameter of an antenna. The resolution of a single aperture is proportional to microwave wavelength and inversely proportional to a diameter of an antenna. On the other hand, when synthetic aperture processing is applied, the resolution is expressed as;

$$\delta_a = \frac{D_a}{2}, \quad (1.7)$$

The resolution in the azimuth direction is proportional to the antenna diameter and independent of the slant range R . Notably, the resolution is determined by not the diameter of the synthetic apertured antenna but half of the real antenna diameter, resulting in meter order resolution. On the other hand, frequency modulation improves the resolution in the microwave emitted direction (range direction). The resolution in the unmodulated case is as follows;

$$\delta_r = \frac{c\tau}{2\sin\theta}, \quad (1.8)$$

where c is the speed of light, τ is the pulse time, θ is the incidence angle. The resolution with frequency modulation is expressed as follows;

$$\delta_r = \frac{c}{2B_w}, \quad (1.9)$$

where B_w is the bandwidth of a microwave. It indicates that the resolution in the range direction only depends on the bandwidth of the microwave. Using this frequency modulation reversely, a method to correct the frequency-dependent phase propagation delay in the ionosphere has been established (Gomba et al., 2016). This method hypothetically considers that a single observation as an observation with multiple frequency bands.

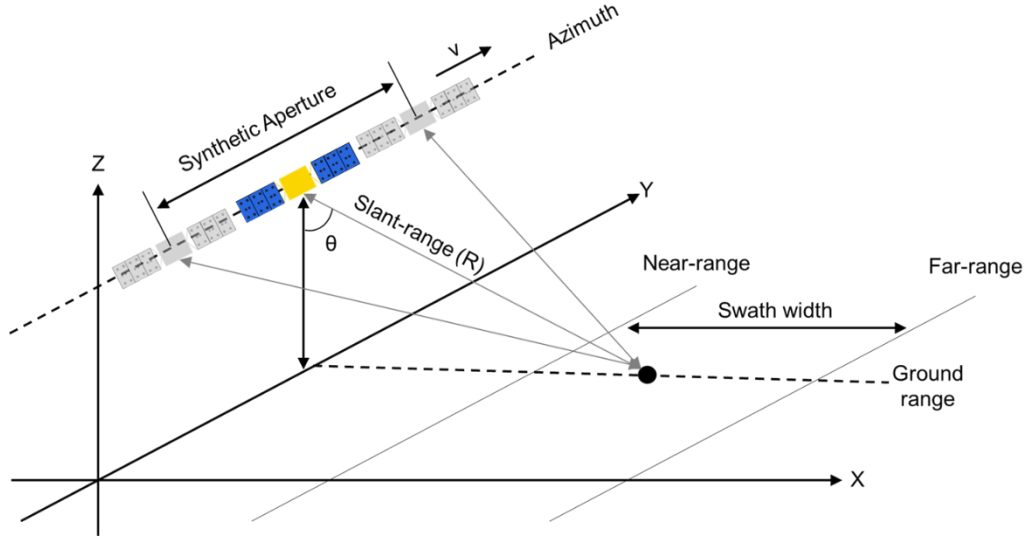


Figure 1-8. Schematic image of SAR geometry. θ is the satellite incidence angle, v is the velocity of the satellite.

The image, firstly obtained from SAR raw data, is called a Single Look Complex (SLC) image because it is not spatially averaged (single look) data expressed in complex numbers. A polar transformation of the complex numbers shows the phase value and backscatter intensity as a complex amplitude. The intensity image indicates a backscattering state of the ground surface. For instance, the temporal variation of intensity is used to detect glacier flow (e.g., Abe and Furuya, 2015) and to observe volcanic craters covered by plumes that cannot be seen in optical images (e.g., Ozawa and

Kozono, 2013). SAR can observe the earth's surface more constantly than optical satellites because it is an active microwave sensor resulting in day and night observation and can penetrate clouds. On the other hand, the phase values look like random noise when viewed in two dimensions image. However, in 1993, an epoch-making result of detecting earthquake-related crustal deformation based on the phase difference between two periods was reported (Massonnet et al., 1993), which significantly impacted geodesy and geophysics.

1.2.3 Interferometric SAR

Interferometric SAR (InSAR) is a space geodetic technique that derives the ground surface displacement from the phase difference in a SAR satellite imaging term. Some studies called it Differential InSAR (DInSAR) to distinguish its aim is ground surface displacement or otherwise (e.g., deriving digital elevation model). Massonette et al. (1993) firstly succeeded in detecting the crustal deformation displacement by simulating and subtracting the phase fringes other than ground displacement. Since then, InSAR has contributed to various geophysical observations such as seismic crustal deformation and volcanism (e.g., Fialko et al., 2001; Takada and Fukushima, 2013). This is because InSAR does not require ground-based observation points and can directly observe deformation at that moment as long as an image is captured before the event. In addition, recent studies have analyzed other than crustal deformation using microwave propagation delays, such as the detection of water vapor content, snow water equivalent, and anomaly of ionospheric electron contents anomaly (e.g., Kinoshita et al., 2013; Guneriusson et al., 2001; Furuya et al., 2017). This chapter describes the principle and analysis examples along the flow shown in step1 of Figure 1-6. For a comprehensive explanation, please see some excellent reviews (Bürgmann et al., 2000; Simons & Rosen, 2015).

The first step is matching the primary and secondary SLC images on the sub-pixel order. It is called coregistration. Calculate the offset in the azimuth and range directions, determine the affine

transformation coefficients with a least-squares method, and resample the secondary SLC. Multiplying the primary SLC image and the complex conjugates of secondary SLC image using the sub-pixel coregistered images derives an initial interfered image (interferogram). The interferogram amplitude is the amplitude product, and the phase represents the phase difference between each SLC image. This initial interferogram phase (ϕ_{init}) is expressed as follows;

$$\phi_{init} = \phi_{orb} + \phi_{elev} + \phi_{disp} + \phi_{iono} + \phi_{atm} + \phi_{noise}, \quad (1.10)$$

where ϕ_{orb} is the satellite orbital fringe, ϕ_{elev} is the fringe related terrain height, ϕ_{disp} is the fringe of ground surface displacement, ϕ_{iono} is the phase delay due to ionosphere, ϕ_{atm} is the phase delay due to water vapor in the troposphere, and ϕ_{noise} is the other noise such as soil water, snow cover, and thermal noise.

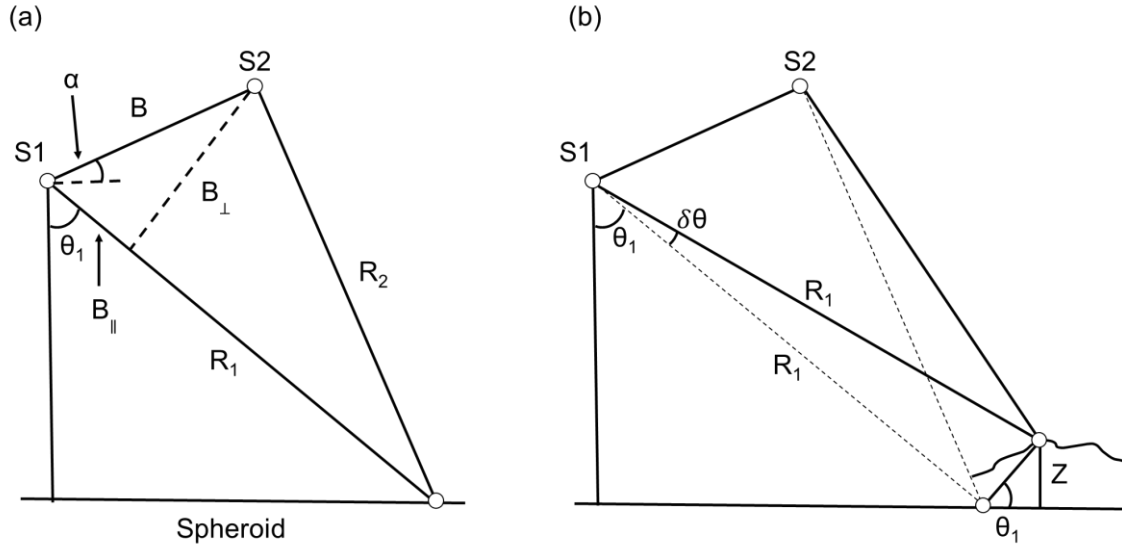


Figure 1-9. The geometry of Interferometric SAR. (a) Orbital fringe without considering the terrain height. (b) Considering terrain height (Z). Modified after Rosen et al. (1996).

Secondly, we simulate the fringe of the satellite orbit and terrain height and calculate the difference from the initial interferogram. Figure 1-9 shows the geometry of the InSAR. S is the position of the satellites, B is the baseline distance between the satellites, and R is the distance between the satellite and the ground surface. B_{\parallel} is a parallel component of B to the direction of the line of sight (LOS) from S1, and B_{\perp} is the perpendicular component. If B is small enough to R, the phase of the interferogram can be expressed as follows;

$$\phi_{orb} = -\frac{4\pi}{\lambda}(R_1 - R_2) \approx -\frac{4\pi}{\lambda}B_{\parallel} = -\frac{4\pi}{\lambda}B\sin(\theta_1 - \alpha), \quad (1.11)$$

where λ is the microwave wavelength. This is the component determined by the satellite's orbit and is called the orbital fringe (or flat earth component). When terrain height is taken into account, the LOS direction changes by $\delta\theta$ as shown in Figure 1-9b.

$$\phi = -\frac{4\pi}{\lambda}B\sin(\theta_1 + \delta\theta - \alpha). \quad (1.12)$$

The phase of the interferogram that varies depending on the terrain height (flatten earth component) is represented by the difference between equations 1.11 and 1.12

$$\phi_{elev} = \phi - \phi_{orb} \approx -\frac{4\pi}{\lambda}B\cos(\theta_1 - \alpha)\delta\theta, \quad (1.13)$$

with the assumption of $\cos\delta\theta \approx 1$ and $\sin\delta\theta \approx \delta\theta$ if the $\delta\theta$ is small. It also can be expressed using the elevation (Z) as follows

$$\phi_{elev} = -\frac{4\pi}{\lambda}B\cos(\theta_1 - \alpha)\frac{Z}{R_1\sin\theta_1}. \quad (1.14)$$

The baseline length is estimated from the satellite orbit information and the elevation derived by DEM in the actual processing. Therefore, creating a conversion table (called lookup table) from map coordinates to Radar Doppler Coordinates (RDC) by coregistering the DEM and primary SLC is necessary to simulate a height map in RDC. Subtracting the orbital and topographic fringe from the initial interferogram, we obtain displacement fringe as follows;

$$\phi_{disp} = \phi_{int} - \phi_{orb} - \phi_{elev} = \frac{4\pi}{\lambda} \delta d, \quad (1.15)$$

where δd is the surface deformation in the LOS direction. If no ionospheric and tropospheric noise is included in an interferogram, this represents the deformation of the ground surface.

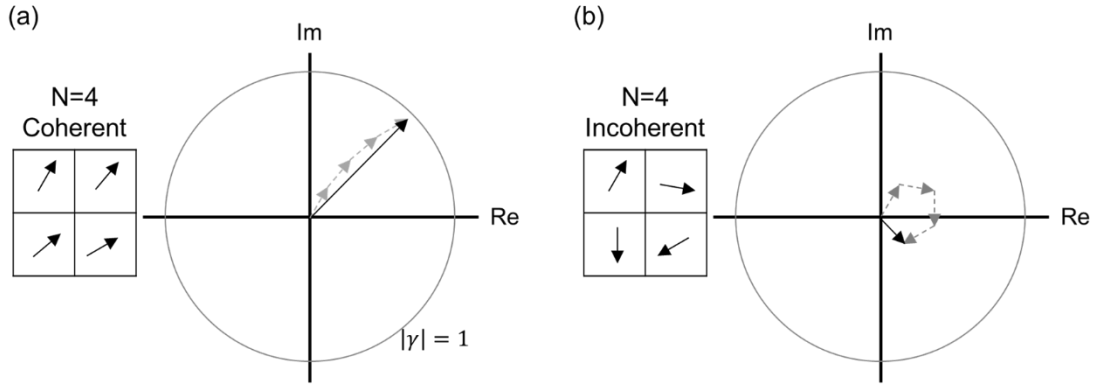


Figure 1-10 Conceptual images of coherence in case of window size of four pixels. The black arrows indicate interferogram complex values on the complex plane. (a) A coherent case. (b) An incoherent case.

The phase of the interferogram is wrapped from $-\pi$ to $+\pi$. Third process is adding the appropriate integer multiple of 2π to each pixel and correcting it to an absolute phase difference. The process is called Unwrapping, and we used a method called Minimum Cost Flow (Costantini, 1998). Because of this feature, it should be noted that the interferogram has an ambiguity of 2π . This thesis also used the basic Goldstein and Werner filter, an adaptive filter for smoothing the interferogram phase (Goldstein and Werner, 1998). In addition, coherence (γ) is the normalized magnitude of the interferogram (Figure 1-11), meaning the degree of decorrelation and defined as;

$$\gamma \equiv \frac{\sum_N C_1 C_2^*}{\sqrt{\sum_N C_1 C_1^* \sum_N C_2 C_2^*}} \equiv \frac{\sum_N \frac{C_1 C_2^*}{|C_1 C_2^*|}}{N}, \quad (1.16)$$

where C is the complex value of each SLC image, N is the number of pixels in the estimation window, and the superscript $*$ means complex conjugate. Coherence can range from 0 to 1. The low-value pixels are masked out in the unwrapping process.

If tropospheric or ionospheric noise is present, it is simulated and subtracted from the interferogram. For instance, tropospheric noise is corrected with meteorological data (Jolivet et al., 2011), and ionospheric dispersive noise is corrected by the split spectrum method, virtually splitting a single SLC into two independent center frequency images (Gomba et al., 2016). Since the SLC images are clipped around fire scars, this thesis considered some noises as long-wavelength phase trends and corrected them using a basic quadratic polynomial approximation. It also excludes the effect of phase changes due to isotropic thaw subsidence, which occurs uniformly across the image. Therefore, we use the vector data of the burned area created in chapter 1.2.1 to mask the areas where local deformation is expected. After the correction, the interferogram phase in the unburned area to almost zero and can discuss the relative displacement within the fire area. Finally, the interferogram is converted to map coordinates using the lookup table reversely. The interferogram shows the relative amount of ground deformation in the LOS direction. Positive values are displacements far away from the satellite, and negative values are displacements toward the satellite.

1.2.4 InSAR for permafrost observation

Liu et al. (2010) was the first to detect the interannual thermokarst deformation by InSAR in Prudhoe Bay, Alaska. Although previous studies reported seasonal deformation (Wang and Li, 1999) and landslides (Singhroy et al., 2007) due to permafrost thawing, this study brought a breakthrough in detecting secular and gradual permafrost thawing with a broad observation range. Since the 2010s, interannual permafrost thaw estimated from ground deformation has been widely discussed in other permafrost zones (e.g., Short et al., 2011 [Herschel Island, Canada]; Antonova et al., 2018 [Lena Delta, Siberia]; Daout et al., 2017 [Tibetan Plateau, China]). In general, ground subsidence associated with gradual thawing due to temperatures rising occurs uniformly over a wide area. However, InSAR can only detect relative displacements within its imaging range and thus cannot detect uniform deformation over the entire SAR imaging scene. In addition, propagated microwave delays due to ionosphere and troposphere can also result in spatial long-wavelength displacement, making it difficult to separate such noise from deformation. For example, Daout et al. (2017) expanded the imaging range by combining multiple Envisat images to include non-deformation regions. Moreover, they attempted tropospheric phase delay correction with an atmospheric reanalysis model.

On the other hand, also for abrupt thawing mainly caused by wildfire, some pioneering studies reported the ground deformation with the InSAR image. In an abruptly disturbed area with a smaller spatial extent than the gradual thawing region, the relative displacement to the adjacent non-disturbed area can be discussed. For example, the 2007 Anaktuvuk River Fire in Alaska was one of the largest tundra fires in the world, extending over 1000 km². ALOS/PALSAR L-band InSAR detected an increase in seasonal thaw subsidence of up to 8cm relative to before the fire (Liu et al., 2014). ALOS/PALSAR also detected interannual subsidence of 6.2cm/year in the first year and 3.3cm/year from two years after the fire (Iwahana et al., 2016a). Michaelides et al. (2019) also detected thaw subsidence due to other tundra fires in Yukon-Kuskokwim Delta, Alaska, using ALOS/PALSAR data. They observed thaw subsidence in several fire scars of different burned ages and discussed the

process of thaw amount restoration with vegetation recovery. There were also reports of fires in a boreal forest zone. For example, Molan et al. (2018) detected thaw subsidence following the 2009 Big-Creek fire, Alaska, by ALOS/PALSAR data. However, in previous studies on abrupt thawing, disturbances such as fires drastically change the surface vegetation and reduce the coherence of InSAR image, consisting of before and after a fire data. Since it is difficult to foresee where fires will occur in advance, it is also difficult to verify the results immediately after a fire by field observations. For these reasons, there has been little discussion about the thawing subsidence process immediately after a fire.

These previous studies were mainly developed in the Alaskan permafrost regions. On the other hand, there are few observations in Siberia, the largest permafrost distribution area in the world. This underdevelopment might be because Russia does not have SAR satellites for scientific observation, and it is socially and physically difficult to verify the results through in-situ observation. Antonova et al. (2018) detected the ground deformation in the thermokarst basins of the Lena Delta by TerraSAR-X InSAR images. Although they mentioned the possibility of scattering noise, they found 2 cm of seasonal subsidence, consistent with previous studies, and discussed the correlation with the spatial distribution of soil water content. Focusing on the abrupt thawing, Yanagiya and Furuya (2020) reported thaw subsidence in the 2014 fire scar southeast of Batagay using ALOS-2/PALSA2 and Sentinel-1 data (details in Chapter 2). In addition, Abe et al. (2020) reported a 0.5-3cm/year thermokarst subsidence in the deforested area around Mayya, Yakutsk detected by ALOS/PALSAR and ALOS-2/PALSAR-2 InSAR images. Notably, in Yakutsk and Batagay, winter snow cover does not affect the coherence due to the extremely dry continental climate. This environment is invaluable for understanding the entire seasonal deformation process, including frost heave. In addition, by using pairs of severe winters when the seasonal heave has ended, we can discuss the interannual variability without considering the difference in the deformation rate from year to year.

To summarize the previous permafrost studies using InSAR, almost all studies have either used L-band InSAR images or mentioned its effectiveness in detecting seasonal and interannual ground deformation. The main reason is that the relatively long wavelength is less affected by ground surface changes (e.g., vegetation, dry snow) and maintains high coherence over long temporal intervals. As Liu et al. (2010) first showed, an observation of accurate permafrost thawing requires a technique that can detect deformation of a few centimeters over several years. On the other hand, the current L-band SAR satellite has relatively fewer observation frequencies than other SAR satellites (e.g., 12 days of C-band Sentinel-1). Hence, more frequent observations by next-generation L-band SAR satellites (e.g., ALOS-4 by JAXA; NISAR by ISRO and NASA) will further develop permafrost observation.

1.3 Thesis outline

The thesis focuses on the post-fire abrupt thaw process around Batagay using ground deformation analysis by InSAR. Each chapter aims to answer the questions about three processes with different spatio-temporal ranges:

- (i) Estimate the medium-term (2-5 years) thaw process after the fire in order to report the detection of ground deformation induced abrupt thawing firstly in Northeastern Siberia.
- (ii) Elucidate the drastic thaw process immediately after the fire taking advantage of high coherence in winter interferogram pair around Batagay.
- (iii) Derive and validate a high spatial resolution map (4 m) of ground deformation to reveal the fine-scaled thawing disturbance within the fire scar.

Chapter2 focuses on the thawing process 2~5 years after the 2014 fire burned in the northwest of Batagay. Time series analysis by the SBAS method revealed the spatio-temporal variation of seasonal and interannual ground deformation. Generally, winter InSAR pairs lose coherence due to changing backscattering processes. However, comparing two independent satellite data confirmed that it can detect deformation signals even with winter pairs. The total subsidence for 2~5 years after the fire revealed that $3.56 \times 10^6 \text{ m}^3$ of subsurface massive ice had melted. Moreover, the seasonal uplift signal was interpreted by premelting dynamics.

Chapter 3 focuses on the initiated thawing process after the 2018 and 2019 fires at the same slope as the Batagaika mega slump, 10 km southeast of Batagay. ALOS-2/PALSAR-2 InSAR detected interannual deformation started two years after the fires. On the other hand, Sentinel-1 InSAR detected the temporal change of the frost heave process. Finally, we discussed the increased heave period based on the thaw depth measurements conducted from 2019 to 2021.

Chapter 4 describes the spatial heterogeneity of the ground deformation within the 2018 and 2019 fire scars near the Batagaika mega slump. ALOS-2/PALSA2 SM1 data revealed the spatial variation of deformation with higher resolution (4 m) than previous studies. As a result, InSAR detected two characteristic signals: the gully within the 2019 fire scar and the displacement boundary within the 2018 fire scar. We measured the thaw depth and surface soil water content (SWC) on each transect by field survey in September 2021. Surface SWC distribution around the gully topography was generally consistent with the spatial variability of seasonal deformation signals. A correlation between seasonal deformation and surface SWC was also found within the 2018 fire scar. However, the vegetation index, elevation, slope, and thaw depth were uniform within the fire scar. Therefore, we hypothesized a heterogeneous distribution of subsurface massive ice and discussed the spatial variation in seasonal deformation.

Chapter 5 summarizes all the topics and concludes on the post-fire permafrost thaw processes around Batagay.

Chapter 2

Post-wildfire Surface Deformation at the 2014 Fire Scar near Batagay, Eastern Siberia, Detected by L-band and C-band InSAR

The contents of this chapter (2.1 – 2.5) have been published in *Journal of Geophysical Research: Earth Surface*. In addition, we report 2019 on-site observation in chapter 2.6.

Yanagiya, K., M. Furuya (2020) Post-wildfire surface deformation near Batagay, Eastern Siberia, detected by L-band and C-band InSAR, *Journal of Geophysical Research: Earth Surface*, 125(7), 1–18. DOI 10.1029/2019JF005473

Chapter 2. Post-wildfire Surface Deformation at the 2014 Fire Scar near Batagay, Eastern Siberia, Detected by L-band and C-band InSAR

2.1 Introduction

Wildfires in boreal and arctic regions are known to have increased over recent decades in terms of both frequency and areal coverage (e.g., Kasischke & Turetsky, 2006; Hu et al., 2010), and have had significant impacts on permafrost degradation (e.g., Jafarov et al., 2013; Zhang et al., 2015; Gibson et al., 2018). Although fires do not directly heat up the subsurface space deeper than 15 cm (Yoshikawa et al., 2003), severe burning decreases surface albedo, and removes vegetation and the surface organic soil layer that previously acted as insulators buffering from changes in air temperature. Subsequent increases in both soil temperature and thickness of the active layer, a near-surface layer that undergoes a seasonal freeze-thaw cycle, have been documented for up to several years after the fire (e.g., Yoshikawa et al., 2003). Meanwhile, in ice-rich permafrost regions, the thawing of permafrost and the melting of massive ice can lead to formation of characteristic landforms such as thaw pits and ponds, and retrogressive thaw slumps. While there are a variety of classifications in terms of morphological and hydrological characteristics (Jorgenson, 2013), those thaw-related landforms and the topography they create are collectively termed as “thermokarst”. However, the role of wildfires in developing thermokarst terrain remains quantitatively uncertain. Moreover, in comparison to the controlled warming experiments in Alaska (Hinkel and Hurd Jr, 2006; Wagner et al., 2018), wildfires in arctic regions may also be viewed as uncontrolled disturbance experiments that aid in understanding the permafrost degradation processes.

Ice-rich permafrost deposits, known as the yedoma ice complex (yedoma), are widely distributed in the lowland of Alaska and Eastern Siberia (Kanevskiy et al., 2011; Schirrmeister et al., 2013). The greatest subsidence within the 2007 Anaktuvuk River tundra fire scar was identified in the yedoma upland by LiDAR (Jones et al., 2015). Yedoma is a unique permafrost deposit in terms of its

extraordinarily high volume of ice (50-90 %) and organic-rich sediments. While the organic carbon trapped in permafrost regions is estimated to be twice that in the current atmosphere, permafrost thawing and related thermokarst processes may release the carbon as greenhouse gasses (CO_2 and CH_4) via microbial breakdown, which may further promote global warming (Mack et al., 2011; Schuur et al., 2015). Thus, in order to estimate the volume of greenhouse gasses released, it is important to evaluate the volume of thawed ice associated with thermokarst processes in yedoma-rich areas.

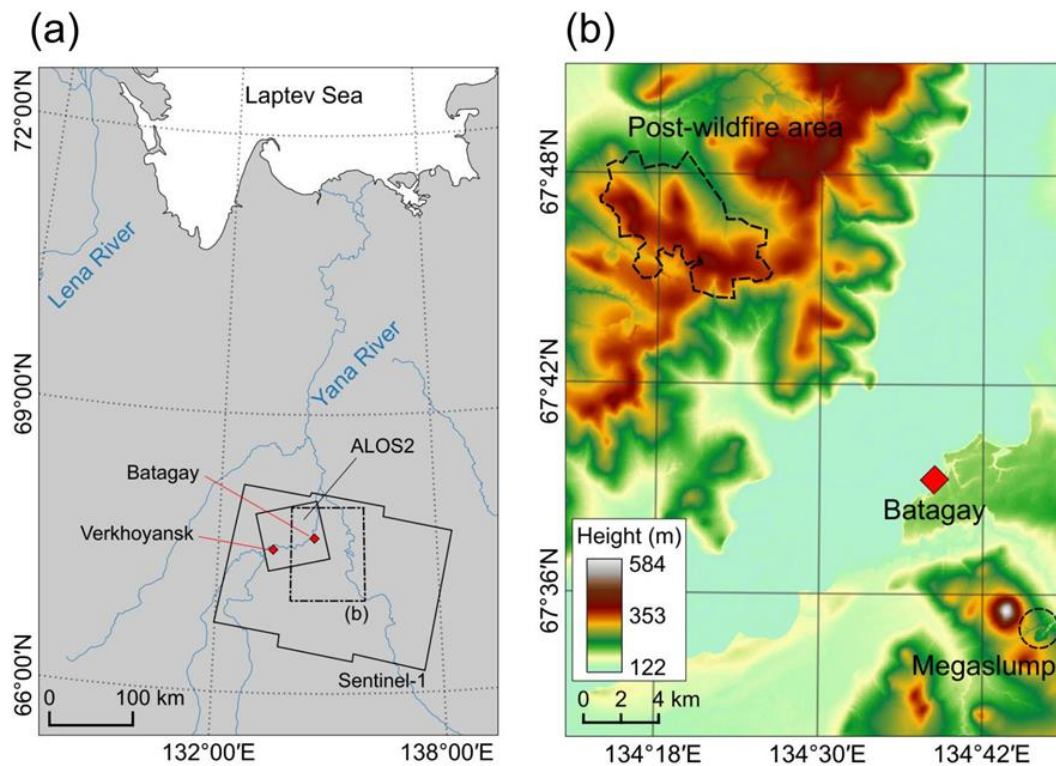


Figure 2-1. (a) Study area in Eastern Siberia. Black solid line boxes indicate the imaging areas taken by each satellite. Dashed line box indicates the area enlarged in (b). Batagay and Verkhoyansk (red diamonds) are located in the imaging area. (b) Elevation map around Batagay based on a TanDEM-X DEM (12 m mesh). The Batagaika megaslump is 15 km southeast of Batagay. Deformation signals due to the wildfire of July 2014 were detected in the black dashed area.

Near the village of Batagay, Sakha Republic, Eastern Siberia (Figure 2-1), there exists the Batagaika megaslump, known as the world's largest retrogressive thaw slump, exposing roughly 50-90 m thick yedoma deposits on the north-east facing slope (e.g., Kunitsky et al., 2013; Murton et al., 2017). Thaw slumps are characterized by a steep headwall surrounding a slump floor and develop as a result of rapid permafrost thawing. The Batagaika megaslump was initiated at the end of the 1970s by deforestation but still appears to be growing (Günther et al., 2016). Considering this feature, it is worth considering whether new disturbances in the proximity will result in the formation of similar landforms. A wildfire incident occurred in July 2014 near Batagay, which, like deforestation, will change the ground thermal regime. Therefore, it is important to examine whether future catastrophic thermokarst development could be similarly initiated at the fire scar, whose area is much larger than the Batagaika megaslump (Figure 2-1b).

The first objective of this study was to assess the effectiveness of satellite Interferometric Synthetic Aperture Radar (InSAR) in detecting surface deformation signals due to wildfire-induced thermokarst over different temporal scales. InSAR has been used to detect long-term and seasonal displacements over several thaw-related landforms in permafrost areas (e.g., Liu et al., 2010, 2014, 2015; Short et al., 2011; Iwahana et al., 2016; Molan et al., 2018; Antonova et al., 2018; Strozzi et al., 2018; Chen et al., 2018). Although subsidence signals as a result of thermokarst associated with Alaskan wildfires have been detected using InSAR (Liu et al., 2014; Iwahana et al., 2016a, 2016b; Molan et al., 2018; Michaelides et al., 2019), no such studies have been conducted on Siberian fires, to our knowledge. Also, all previous InSAR-based post-wildfire deformation mapping has been performed over relatively flat terrains, but no reports over hillslopes have been shown. Moreover, in contrast to previous studies, we employed two independent SAR imageries with distinct carrier frequencies and polarizations, L-band (1.2 GHz) HH- and C-band (5.4 GHz) VV-polarized microwave. Because the imaging geometries were different and had different sensitivities to the 3D displacement

vector, we could not only take advantage of the performance of each sensor in mapping deformation signals but could also cross-validate the measurements by two InSAR data sets.

Our second objective was to estimate the cumulative spatial distribution of subsidence, which allows us to estimate the thawed ice volume. Surface deformation signals over permafrost areas have been interpreted as being caused by two major processes: (1) irreversible subsidence due to thawing of ice-rich permafrost or excess ice and (2) seasonally cyclic subsidence and uplift (Liu et al., 2014, 2015; Molan et al., 2018). In these previous reports, however, quality interferograms (InSAR images) were limited in terms of both the temporal coverage and resolution. This limitation existed because the image acquisition interval was 46 days at best and the orbit was not well-controlled in the Japanese Advanced Land Observation Satellite (ALOS) operated from 2006 to 2011 by the Japan Aerospace Exploration Agency (JAXA). For instance, Liu et al (2015) assumed a simple linear subsidence trend in their inversion, probably because of the limitation in temporal coverage. Moreover, the 1.5-year temporal coverage in Molan et al (2018) would be not long enough to resolve the detailed temporal evolution. Hence, the total thawed ice volume estimates were uncertain. We also compared the spatial distribution of subsidence with burn severity and local landform.

Several studies have reported uplift signals by InSAR over permafrost areas (Samsonov et al., 2016; Daout et al., 2017; Chen et al., 2018; Rouyet et al., 2019), but no clear uplift signals have been shown in previous studies at fire scars as interferometric coherence was lost during the freezing season in analyzed areas. In contrast, this study provides the unambiguous detection of upheaval signals in the early freezing season and confirms the absence of continuing uplift during the colder season.

Our third objective was, given the clear frost heave signals, to interpret more physically the observed data. This was because it has been widely accepted that frost heave is unrelated to volume expansion of pre-existing pore water into ice, but caused, instead, by ice lens formation due to the migration of water (Taber, 1929, 1930). However, a physical understanding of frost heave mechanisms has been established only during recent decades (e.g., Dash, 1989; Worster and Wettlaufer, 1999; Rempel et al., 2004; Wettlaufer and Worster, 2006; Dash et al., 2006; Rempel, 2007). Although it appears counter-intuitive, taking a soil particle inside a unit of ice, there exists an unfrozen (premelted) water film between the ice and soil even below the bulk-melting temperature of 0 °C (e.g., Dash, 1989; Worster and Wettlaufer, 1999). Premelted water can be present because of the depression of freezing temperature by the curved geometry of the soil particle and the repulsive inter-molecular force between ice and soil particles. Under a temperature gradient the repulsive thermomolecular pressure on the colder side is greater than on the warmer side. Hence, the net thermo-molecular force on the soil particle tends to move it toward the warmer side, a phenomenon known as thermal regelation (e.g., Worster and Wettlaufer, 1999; Rempel et al., 2004). Meanwhile, the premelted water migrates toward lower temperature, where ice lenses will be formed. These processes are responsible for frost heave and continue as long as the temperature gradient is maintained, or until significant overburden pressure is applied (e.g., Dash, 1989; Worster and Wettlaufer, 1999; Rempel et al., 2004). Although there is still an ongoing debate on the theory (Peppin and Style, 2013), we applied the simple, physics-based 1D theory of Rempel et al (2004) to the observed frost heave signal so that we could physically interpret and explain the observed signals using reasonable parameters.

2.2 Study Site

Batagay (67°39'30" N, 134°38'40" E) is located on the Yana River, which is 872 km long and covers a 238,000 km² basin in a part of the East Siberian Lowlands in the Sakha Republic (Figure 2-1). The elevation ranges between 138 m above sea level at Batagay village and 590 m at Mt. Kirgilyakh on the north-west of Batagaika megaslump (Figure 2-1b). Our study site was a fire scar located on the western bank of Yana River, with elevation ~200-400 m (Figure 2-1b). The climate is highly continental with a mean annual temperature of -15.4 °C and mean annual precipitation 170 – 220 mm (Murton et al., 2017). Meteorological data were sourced from Verkhoyansk, 55 km west of Batagay. The mean temperature for July and December 2017, respectively, was 12 °C and -44 °C, while precipitation was 30 mm and 6 mm, respectively.

We have no in-situ observation data on permafrost conditions and sedimentology before the fire. However, the burned site is approximately 25 km to the northwest of the Batagaika megaslump (Figure 2-1); thus, we refer to the summary provided by Murton et al (2017) as a proxy for basic information on the burned area and permafrost. The open forest is dominated by larch with shrubs and lichen moss ground cover. Using normalized vegetation index by Landsat images we confirmed that the prefire vegetation at the fire scar was almost the same as that around the megaslump. Permafrost in the Yana River valley is continuous with the mean annual ground temperature at the bottom of the active layer, ranging from -5.5 °C to -8.0 °C, with the active layer thicknesses (ALT) beneath the forest/moss cover and open sites being 20-40 cm and 40-120 cm, respectively (Murton et al., 2017). In the upslope at Batagaika megaslump, below the 150 cm thick near-surface sand layer there lies a 20-45 m thick upper ice complex, under which there is a 20-38 m thick lower sand layer. Below this lies a 3-7 m thick lower ice complex (Murton et al., 2017). Although the horizontal distribution of this massive ice complex is yet uncertain, we discuss the possible variations in the ALT in section 2.5.2.

The wildfire incident occurred in July 2014 over 36 km² area, northwest of Batagay (Figure 2-1). This wildfire event was evident in the Landsat and MODIS optical images taken between July 17 and August 2, 2014. While wildfires in northeastern Siberia are often attributed to human activity (Cherosov et al., 2010), the cause of the July 2014 wildfire is uncertain. The number of days with high flammability has noticeably increased over large parts of Russia, including the Far East (Roshydromet, 2008). For instance, areas near our study site have experienced even larger wildfires in 2019 (Siberian Times, 2019), as well as a smaller wildfire near the Batagaika megaslump in 2018.

2.3 Methods

2.3.1 InSAR and Data Sets

InSAR has been used as a technique to detect surface displacements (see Bürgmann et al., 2000; Hanssen, 2001; Simons and Rosen, 2015 for detailed reviews). InSAR can map surface displacements over the swath areas with spatial resolution on the order of 10 m or less. InSAR image, called an interferogram, is derived by taking the differences between the phase values of SAR images at two acquisition epochs and further correcting for the known phases contributed from orbital separation (spatial baseline) and topography. Most SAR satellites have near-polar orbits, transmit microwave pulses normal to the flight direction and illuminate the surface of the Earth in ~50-500 km wide belts depending on satellite type and its observation mode (Figure 2-1a). The actual InSAR deformation map indicates the radar line-of-sight (LOS) changes that are derived by a projection of the 3D surface displacements onto the LOS direction. Because the incidence angle of the illuminating microwave is ~30°-40°, LOS changes are most sensitive to vertical (up-down) displacement followed by east-west displacement and are least sensitive to north-south displacement because of near-polar orbit. More specifically, the sensitivity to east-west displacement changes sign, depending on whether the surface is illuminated from the east or the west.

Depending on the specific two SAR image pairs and imaged locations, it is not always possible to quantify surface displacements from interferograms. As the phase values of an original interferogram are wrapped into $[-\pi, +\pi]$ with 2π ambiguity, they need to be unwrapped to quantify spatially continuous LOS changes. However, phase unwrapping becomes impossible when the reflected waves received at the two acquisitions lack interferometric coherence (i.e., they are uncorrelated with each other). Lower coherence is caused by long spatial baseline and temporal changes in the scattering characteristics at the SAR image resolution cell (temporal decorrelation). For instance, significant ground cover differences between conditions of deep snow and dry surface cause temporal decorrelation.

Effects of microwave propagation through non-vacuum medium, ionosphere and troposphere, on the derived interferometric phase also need to be considered, as they generate apparent LOS changes that are unrelated to surface displacements. Moreover, recent studies have also reported the effect of soil-moisture changes through volume scattering within the surface soil on the interferometric phase (e.g., De Zan et al., 2014; Zwieback et al., 2015, 2016).

In this study, we used L-band (23 cm wavelength) HH-polarized SAR images derived from the PALSAR-2 acquired by the Japanese Advanced Land Observing Satellite 2 (ALOS-2) from 2015 to 2019 together with C-band (5.6 cm wavelength) VV-polarized SAR images taken during 2017-2019 derived from Sentinel-1 (Figure 2-2; see also Tables 8-1 and 8-2 in Appendices for details). The incidence angles at the center of images were 36° and 39° for ALOS-2 and Sentinel-1, respectively. In the data sets used, ALOS-2 and Sentinel-1 were illuminating the surface from the west and east, respectively, and thus the sensitivity to the east-west displacement was in reverse. To correct for topographic phases, we used TanDEM-X DEM (12 m mesh). Compared to the former ALOS-1/PALSAR-1 InSAR, the ALOS-2 orbit is well controlled, and the spatial baseline is much shorter

(Table 8-1, in Appendices), which allowed us to ignore DEM errors in the interferograms; the same is true for Sentinel-1 (Table 8-2, in Appendices).

Tropospheric delay itself does not depend on the carrier frequency, but C-band InSAR provides more phase changes because of its shorter wavelength. In contrast, L-band InSAR phase is more prone to ionospheric effect, which could be corrected for by range split-spectrum method (Gomba et al., 2016; Furuya et al., 2017). However, the spatial scale of ionospheric anomalies was much larger than that of the burned area, and the ionospheric signals were apparently uncorrelated with the deformation signal. Thus, we simply took out the long-wavelength phase trend by fitting a low-order polynomial with clipped InSAR images after masking out the burned area. We also corrected for topography-correlated tropospheric errors when they clearly appeared in the InSAR image. These procedures were somewhat ad-hoc but allowed us to isolate relative displacements with respect to unburned areas regarded as reference. It was also likely, however, that possible long-wavelength permafrost degradation signals, known as “isotropic thaw subsidence” (Shiklomanov et al., 2013), were eliminated. Yet, it would be challenging to detect isotropic thaw subsidence signal only from InSAR data. Hence, we simply ignored such possible long-wavelength deformation signals.

Long-term InSAR & Time series analysis (Section 2.4.2)

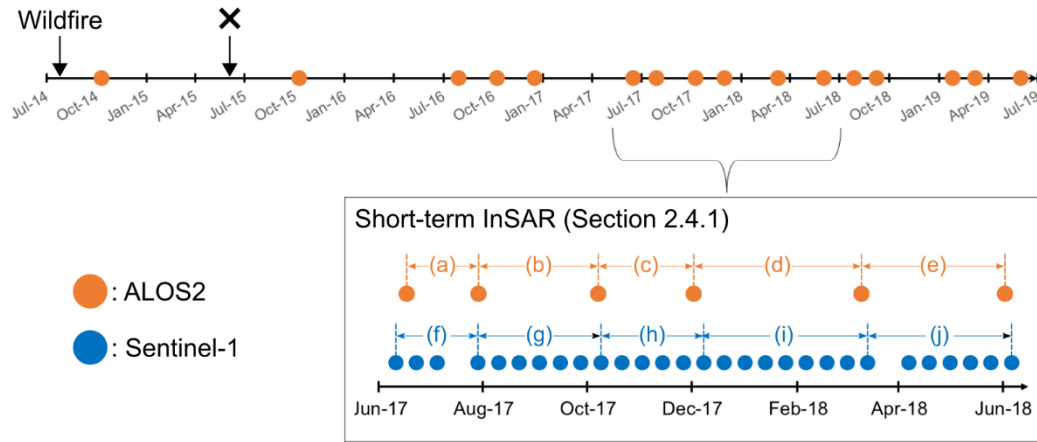


Figure 2-2. Schematic diagram of data time series. (Top) Long-term changes are derived from ALOS-2 acquired on orange dots. Wildfire occurred from July to August 2014, and JAXA modified the center frequency of PALSAR-2 Beam No. F2-6 data in June 2015 shown with the cross. (Bottom) Short-term deformation during 2017-2018 as examined by Sentinel-1 images. We compare the ALOS-2 and Sentinel-1 deformation maps during the five periods, (a)—(e) and (f)—(j).

While ALOS-2 has only imaged the area since 2014 its data acquisition interval is much longer than that of Sentinel-1 (Figure 2-2). Previous studies demonstrate that it is not possible to infer the total subsidence using pre- and post-wildfire SAR images, as the drastic changes in land cover cause low interferometric coherence (Liu et al., 2014; Molan et al., 2018). Additionally, JAXA changed the carrier frequency of PALSAR-2 in June 2015 (Figure 2-2). Hence, monitoring long-term deformation using ALOS-2 InSAR is possible only since October 2015. Conversely, frequent data acquisition in Sentinel-1 started only in 2017. Thus, we first performed an inter-comparison between ALOS-2 and Sentinel-1 InSAR, focusing on the seasonal changes in 2017. We stacked Sentinel-1 interferograms to set the temporal coverages to nearly identical with those of ALOS-2 (Figure 2-2). Stacking was necessary because we failed to derive long-term Sentinel-1 interferograms, as the burned

areas quickly lost coherence. During the temporal interval of ALOS-2 images Sentinel-1 had more cycles. Therefore, the number of Sentinel-1 stacks varied from three to eight (Figure 2-2).

Although L-band SAR is known to have better interferometric coherence than C-band SAR (e.g., Rosen et al., 1996) our study indicated that Sentinel-1 could maintain a comparable interferometric coherence with L-band ALOS-2 even during winter season. This is likely due to the short acquisition period of 12 days as well as the somewhat drier snow in the area in winter that allows microwave to reach the ground. A dry snow cover of depth less than 1 m is undetectable to microwave radiation, whereas over wet snow surface scattering dominates (Rees, 2001). The frequent data acquisition of Sentinel-1 since 2017 allowed us to examine detailed seasonal changes in surface deformation (Figure 2-2). Some Sentinel-1 InSAR pairs in early summer, however, did not show good coherence, possibly due to snow wetness.

In order to infer long-term temporal changes and cumulative displacements, we performed SBAS (Small Baseline Subset)-type time-series analysis (Berardino et al., 2002; Schmidt and Bürgmann, 2003), using 50 high-quality ALOS-2 interferograms that included one-year- as well as short-term interferograms (Figure 2-3). We could estimate the average LOS-change rates between each acquisition epoch without assuming any temporal change models. In contrast to the original SBAS approach, we did not estimate DEM errors because the well-controlled orbit, as well as the precise TanDEM-X DEM, have no sensitivities to those errors.

In order to estimate the errors of the derived time series, we assumed each original SAR scene contained 0.2 cm errors, and made InSAR data covariance matrix, following the method of Biggs et al. (2007). The errors are relatively smaller than those in previous studies of SBAS analysis (e.g. 0.4 cm in Schmidt et al., 2003; 0.75 cm in Biggs et al., 2007), because, as noted earlier, we took

out the long-wavelength phase trend from each InSAR image, and the analysis area is smaller (12×12 km) than previous studies.

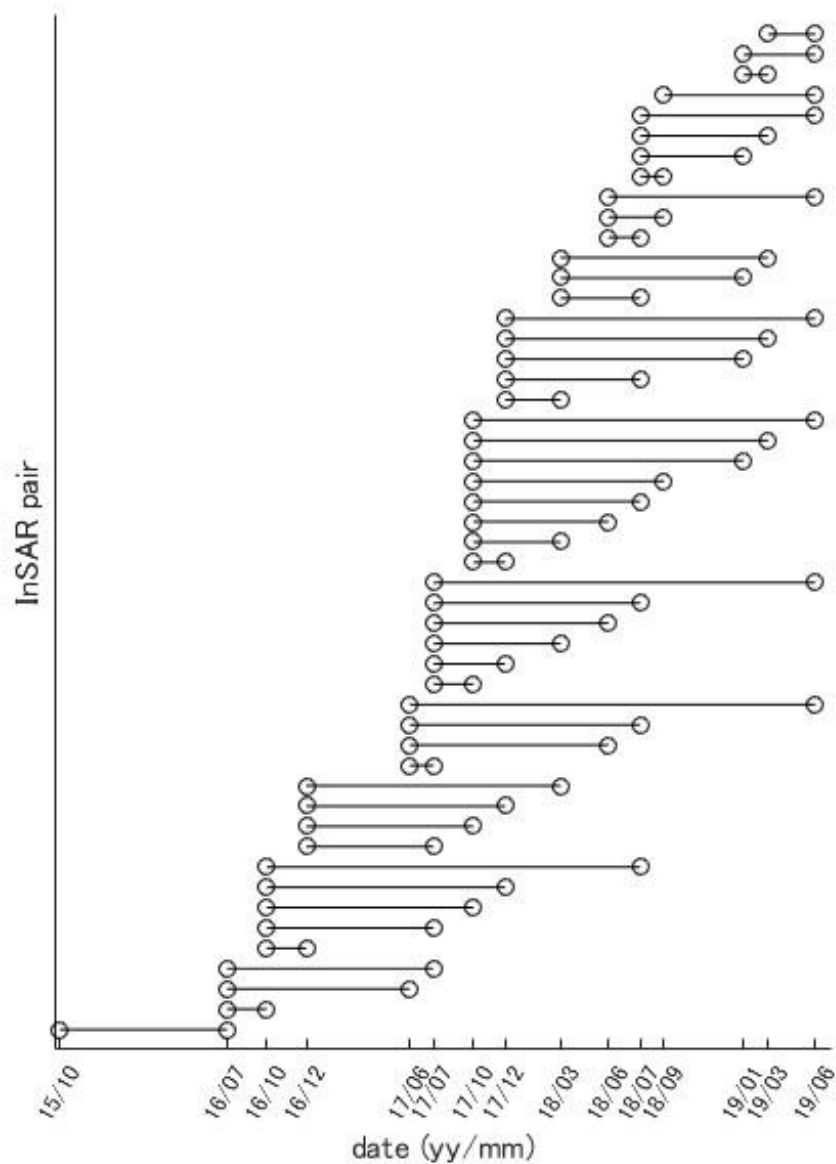


Figure 2-3. Temporal distribution of interferograms for the time-series analysis. 50 interferograms were generated from 15 ALOS-2 SAR images.

2.3.2 Multispectral remote sensing of burn severity

Normalized burn ratio (NBR) is a useful multispectral remote sensing index to assess the impact of wildfire on vegetation. Vegetation reflects more strongly in the near-infrared (NIR) than in the shortwave infrared (SWIR) region, while a fire scar reflects more strongly in the SWIR. Utilizing this property, NBR is defined as $NBR = (NIR - SWIR) / (NIR + SWIR)$. The difference NBR (dNBR), i.e., the difference between prefire NBR and postfire NBR, indicates burn severity (Key and Benson, 2006; Miller and Thode, 2007). Generally, when dNBR is greater than 0.66 the fire is regarded as “highly severe”. We computed dNBR for the 2014 fire using Landsat 8, Band 5 (850-880 nm) and Band 7 (2110-2290 nm) images for near-infrared and shortwave-infrared, respectively, to associate the inferred subsidence distribution with burn severity.

2.3.3 One dimensional frost-heave theory based on premelting dynamics

We used the one-dimensional frost-heave theory as a tool to interpret the observed uplift signals. Inspired by one-way frost heave experiments (Mutou et al., 1998; Watanabe and Mizoguchi, 2000), Worster and Wettlaufer (1999) and Rempel et al (2004) derived a steady-state heave rate V_l of an ice lens, considering the force balance among thermo-molecular force F_T , hydrodynamic force F_μ , and overburden force F_O (pressure P_O). Here, we assumed a constant heave rate V_l , which may not necessarily reflect the actual observations shown below as well as in Hu et al (2018). However, this assumption simplified the theory, and we assumed that the observed heave rate did not change drastically over time. Rempel et al (2004) proposed a non-dimensional heave rate v_l of an ice lens as a function of its boundary position ξ_l given:

$$v_l \equiv \frac{\mu V_l}{k_0 \rho G} = \left[\int_0^{\xi_l} (1 - \phi S_S) d\xi - p_o \right] \left[\int_{\xi_h}^{\xi_l} \frac{(1 - \phi S_S)^2}{\tilde{k}} d\xi \right]^{-1}, \quad (2.1)$$

where μ , k_0 , and ρ are the viscosity of water, the permeability of ice-free soil, density of water, respectively. The quantity $G \equiv (L/T_m)\langle \nabla T \rangle$ has the same dimension as gravity and indicates thermo-

molecular force when multiplied by the mass of displaced ice; L is the latent heat of fusion and T_m is the bulk melting temperature. The first and second term in the bracketed numerator are proportional to F_T and F_O , respectively, while the bracketed denominator is proportional to F_μ . The integral is performed along $\xi \equiv z/z_f$, where z_f is the position above (below) where ice saturation S_s becomes non-zero (zero); z_h indicates the position where hydrostatic pressure is achieved, and ϕ is the porosity of soil. The normalized overburden pressure and permeability are defined as $p_0 \equiv P_0/\rho G z_f$ and $\tilde{k} \equiv k/k_0 \geq 1$, respectively.

2.4 Results

We performed an inter-comparison of ALOS-2/Sentinel-1 interferograms, focusing on the seasonal changes in surface deformation. We then showed short-term deformation derived by Sentinel-1 and long-term deformation derived by time-series analysis of ALOS-2. Subsequently, we estimated the total volume of thawed excess ice. Although both satellite images covered the Batagaika megaslump we did not observe clear LOS changes as detected at the fire scar, which could be due to the lack of spatial resolution of the InSAR images.

2.4.1 Seasonal deformation and comparison of ALOS-2/Sentinel-1 interferograms

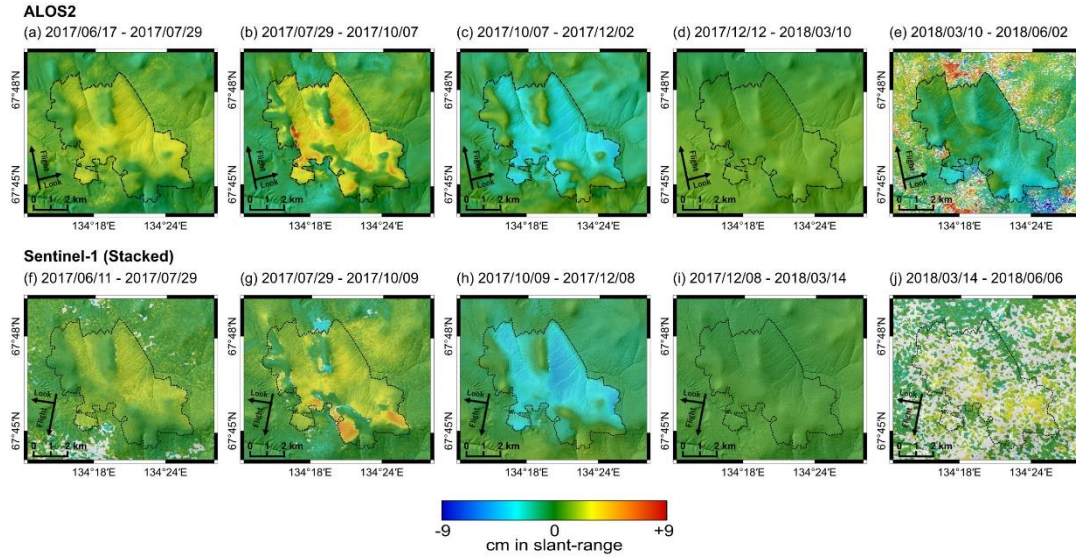


Figure 2-4. (Top) ALOS-2 interferograms during the five periods, (a—e). (Bottom) Sentinel-1 stacked interferograms during the five periods, (f)—(j), derived so that the temporal coverage could nearly match those from (a) to (e); all the interferograms are overlaid on shaded relief maps. Warm and cold colors indicate LOS changes away from and toward the satellite, respectively.

We compared the ALOS-2 and stacked Sentinel-1 interferograms for five periods (Figure 2-4) and assessed their differences (Figure 2-5). Despite differences in look directions both ALOS-2 and Sentinel-1 indicated extensions in the LOS during periods (a, f) from the middle of June to the end of July and (b, g) from the end of July to the early October. Also, their deformation areas and amplitude were mostly consistent, suggesting that LOS changes were largely due to summer subsidence (see section 2.5.1 below for details). In terms of the spatial distribution of deformation signals, we noticed that the LOS changes over higher-elevation areas such as ridge and peak were insignificant, whereas the boundaries between the burned and unburned areas were clear. The north-western area, however,

showed few LOS changes (see section 2.5.2 for the relationship between LOS changes and burn severity). During the period (c, h) from early October to early December both ALOS-2 and Sentinel-1 indicated shortening in the LOS by an approximate 5 cm maximum, and the deformation areas and amplitude were quite similar. This observation presumably indicated frost heave in the early freezing period. In view of the previous three periods, both subsiding and uplifting areas were nearly the same. The following period (d, i) from early December to the middle of March also included the winter season with much colder air temperatures, but we did not observe any significant deformation signals, indicating that frost-heave virtually stopped in early December. While the good interferometric coherence during mid-winter was an unexpected result, we speculate that it could have been due to drier, lower amounts of snowfall.

In the periods (e, j) from the middle of March to early June, both ALOS-2 and Sentinel-1 suffered from decorrelation, and we could not identify clear deformation signals. However, in light of Figure 2-6 below, each of the Sentinel-1 interferograms had overall good coherence with the exception of the data acquired in the middle of May. These observations suggested that the decorrelation may be attributable to the rapid changes on the ground surface during the initiation of the thawing season when the air temperature rises above the freezing point and the active layer begins to thaw.

Figure 2-5 shows the differences between ALOS-2 and Sentinel-1 InSAR data with nearly identical periods, which may help in cross-validating the measurements and understanding the actual deformation processes. The estimated differences and their 2σ scatter were 0.5 ± 1.2 cm (Fig 2-5a), 0.7 ± 2.3 cm (Fig 2-5b), 0.3 ± 1.3 cm (Fig 2-5c), and 0.6 ± 0.3 cm (Fig 2-5d), with mean of 0.5 ± 1.5 cm. The differences and their variances were variable over time but apparently indicated some systematic trends. For instance, over the east-facing slopes, the differences were almost always positive (This is discussed more comprehensively in section 2.5.1).

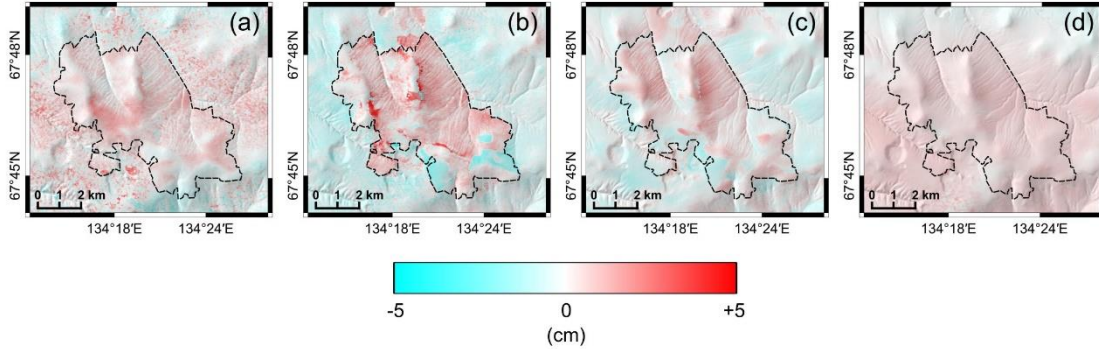


Figure 2-5. Differences in LOS-change detected by ALOS-2 and Sentinel-1 seasonal interferograms (Figures 2-4 a-d and f-i). In the last term of seasonal analysis (Figure 2-4 e and j), we could not estimate differences due to coherence loss.

The Sentinel-1 interferograms for 2017 demonstrate that the progress of deformation was not at a constant rate (Figure 2-6). The most rapid deformation took place in June (periods 1 and 2) with no substantial deformation in July (period 3) and started to subside again in August (periods 4-6). We found that the subsidence occurred sporadically over time and space and that the burned area did not uniformly subside. For periods 4, 5 and 9 we were unable to perform phase unwrapping at specific locations near the ridge and the boundaries between the burned and unburned areas. These unwrapping errors were responsible for the localized, large differences observed in Figure 2-5b. We confirmed the presence of low coherence bands along the unwrapping errors, which may suggest large phase jumps due to large displacements during the 12 days; enigmatically, no such line-shaped low coherence was detected in the long-term ALOS-2 interferograms. Moreover, Figure 2-6 demonstrates that the frost heave started in late September, which was missed in the periods (b) and (g) of Figure 2-4, and that the absence of any deformation signals lasted from early December to May of the following year. We will physically interpret the absence of deformation signals during the coldest season in section 2.5.3.

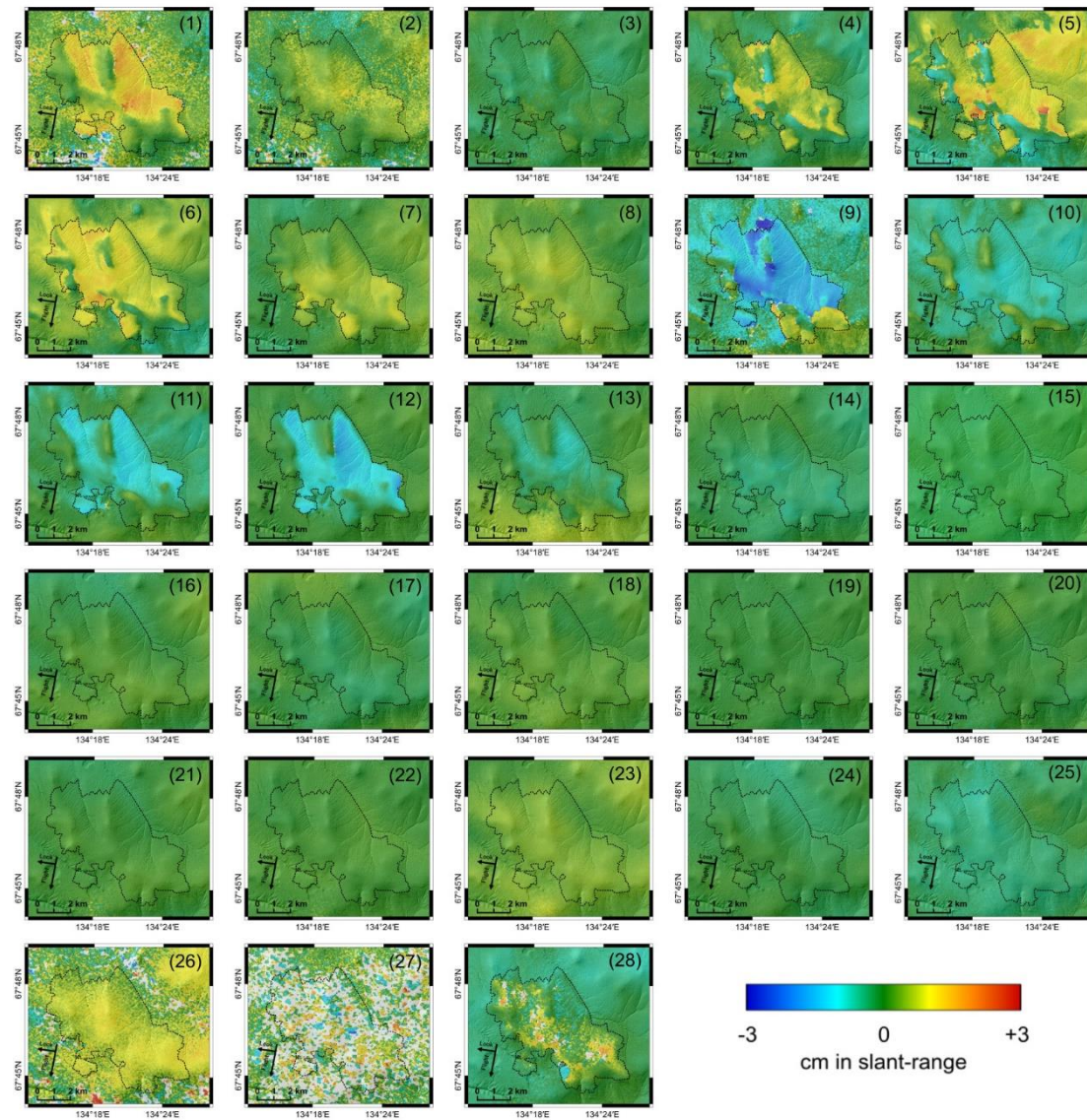


Figure 2-6. Sentinel-1 interferograms during the 27 periods from June 2017 through June 2018 overlaid on hill-shade map. Details of each image are described in Appendix (Table 8-2).

2.4.2 Long-term deformation inferred from time-series analysis of ALOS-2 interferograms

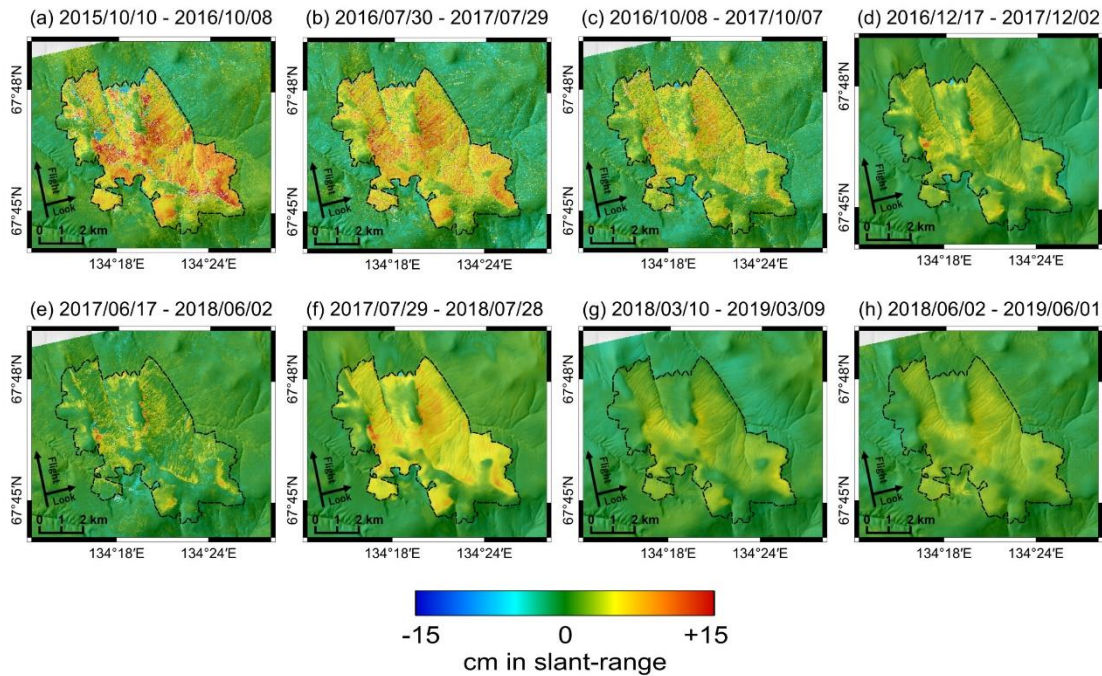


Figure 2-7. LOS-changes of ALOS-2 interferograms overlaid on shaded relief map.

Details of each image are described in Table 8-1; imaging was performed by ascending, right-looking orbit. Warm and cold colors indicate LOS changes away from and toward the satellite, respectively. Black dashed line indicates the boundary between the burned and unburned area confirmed with Landsat optical images.

Figures 2-7 a-h show ALOS-2 interferograms, each of which covers nearly one-year after October 2015 with some overlaps in its temporal coverages. Figure 2-7a, derived at the earliest period after the fire, indicates the maximum one-year subsidence to be as much as 10 cm or more. If the amplitude and timing of seasonal subsidence/uplift cycle are invariable over time, a one-year interferogram will tell us only the irreversible displacements regardless of the acquisition times of primary/secondary images, which corresponds to the “pure ice” model in Liu et al (2015). Figure 2-7

sequentially shows the periods from October 2015 to June 2019 and indicates that the yearly subsidence rate slowed down. However, the variations of the one-year LOS changes in Figures 2-7 suggest that the actual deformation processes were more complex.

Figure 2-8a shows the cumulative LOS changes from October 2015 to June 2019 derived from SBAS-type time-series analysis, and that the maximum LOS extension reached as much as 25 cm; the 2σ errors for Figure 2-8a were ± 1.5 cm. Considering that the LOS changes during the first year after the 2014 fire were not included, the total LOS changes were presumably much greater than 25 cm, which meant that the subsidence was greater than 30 cm on account of the 36° incidence angle. As mentioned earlier, however, the higher-elevation areas such as the ridge did not undergo significant deformation, which probably would have been the case even during the first year after the fire. In addition to the high elevation areas, we realized clear contrasts in the LOS changes between the east- and the west-facing slopes near the northwestern area and the central north-south trending ridge; this spatial heterogeneity could also be recognized in Sentinel-1 (Figure 2-4). Their possible mechanisms comparing the burn severity (Figure 2-8b) and local landform (Figure 2-8c) are discussed in section 2.5.2.

We show the estimated time-series data at four representative sites (Figures 2-9 a-d), whose locations are indicated in Figure 2-8a. The sites (a) and (b) underwent nearly the same cumulative LOS changes by roughly 20 cm but were located at different slopes that are 4.3 km apart. On the other hand, the cumulative LOS changes at the site (d) were relatively small (approximately 10 cm). The site (c) located in the ridge did not show either significant seasonal or long-term deformation.

Time series data in Figures 2-9a and 2-9b clearly indicate that the largest subsidence took place from 2015 and 2016. We believe, however, that the most significant subsidence probably

occurred only during the thaw season in 2016, as we have observed earlier, that no deformation occurred from December to March. Thus, the actual subsidence rate from October 2015 to July 2016 should have been more complicated than that expected from the linear trend in Figures 2-9a and 2-9b. The error bars in Figures 2-9 a-d indicated an estimated standard deviation with 2σ and attained ± 1.5 cm in the last epoch.

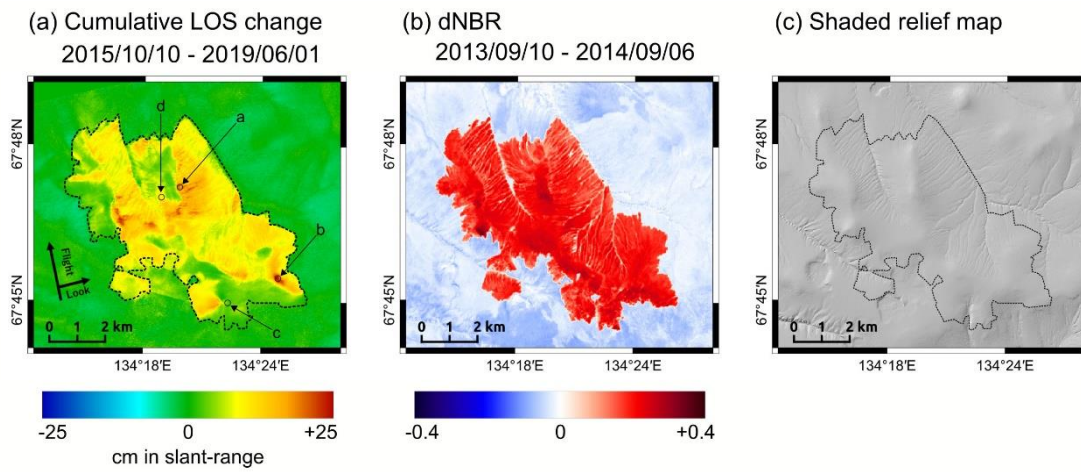


Figure 2-8. (a) Cumulative LOS changes from 2015 to 2019 estimated by InSAR time-series analysis. The 2σ error is ± 1.5 cm. The time series of LOS change at each site (a–d) is indicated in Figure 2-9. (b) Map of dNBR before and after the fire. (c) Shaded relief generated from DEM. Black dashed line indicates the boundary of the 2014 fire.

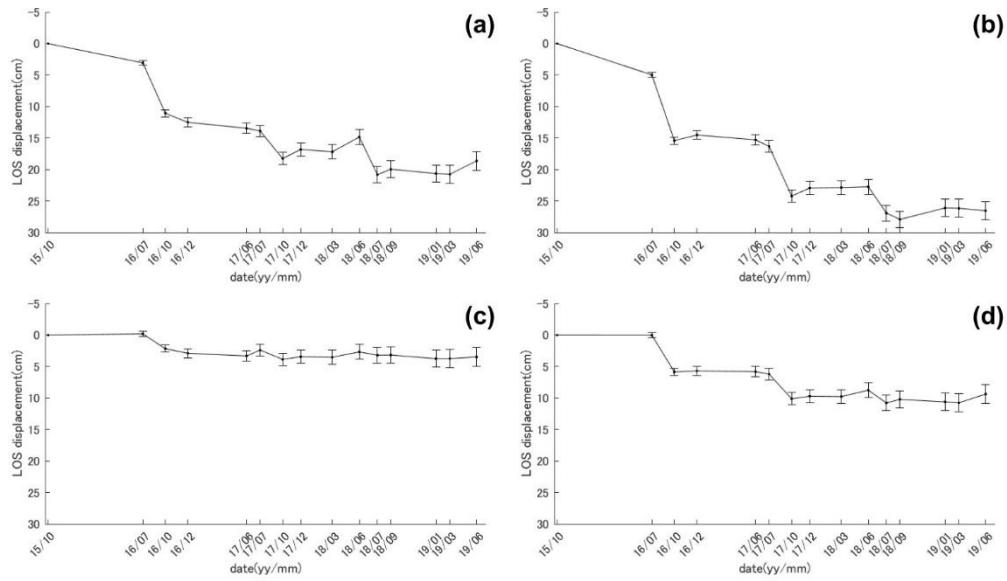


Figure 2-9. Panels (a–d) indicate the time series of LOS changes at each point indicated in Figure 2-8. Sites (a) and (b) are located at the east facing slope. Site (c) is located at the ridge, where no deformation signal was detected by original interferograms. Site (d) is at the west facing slope.

2.4.3 Estimating the total volume of thawed excess ice

Post-wildfire deformation over a permafrost area presumably consists of two contributions: (1) irreversible subsidence due to melting of ice-rich permafrost below the active layer, and (2) seasonally cyclic subsidence and uplift due to freeze-thaw of the active layer (Liu et al., 2014, 2015; Molan et al., 2018). In order to separate the two processes from the observed deformation data, Liu et al (2014) used independent ground-measured ALT data to predict the ALT contribution to total subsidence. Ground-measured pre-fire ALT data were not available at this study site. Given the temporal evolution of post-wildfire deformation data (Figures 2-9 a-d), however, we may regard the cumulative deformation in Figure 2-8a as being due to irreversible subsidence during the period between October 2015 and June 2019, and estimate the total thawed volume as $3.56 \pm 2.24 \times 10^6$ m³; the error bar is based on the root mean square of the no-deformation signals outside the burned

area, which is multiplied by the burned area. However, in view of the temporal evolution in Figure 2-9, we could speculate that a much larger deformation was also taking place immediately after the 2014 fire until October 2015, during which, unfortunately, no deformation data are available. Thus, this estimate should be viewed as a lower estimate, with the actual volume of thawed permafrost possibly being much greater.

Nevertheless, despite its much smaller area size (Figure 2-1b), the thawed volume at the Batagaika megaslump is greater than $2.5 \times 10^7 \text{ m}^3$ (Günther et al., 2016), an order-of-magnitude larger than our estimate above. Moreover, the thaw-subsidence rate at the fire scar is slowing down (Figure 2-9). We discuss the possibility of the another megaslump emergence at the fire scar in section 2.5.2.

2.5 Discussion

2.5.1 Similarities and differences in the ALOS-2 and Sentinel-1 interferograms: implication for insignificant slope-parallel sliding

Taking into account the imaging geometries of the ALOS-2 and Sentinel-1, we could comprehensively interpret the differences in Figure 2-5 and also infer the actual deformation processes. The weights multiplied to the 3D-displacements, (U_{ew} , U_{ns} , U_{ud}), to compute LOS changes were +0.573, +0.132, and -0.809 for ALOS-2 and -0.583, +0.236, and -0.777 for Sentinel-1, respectively; eastward, northward and upward displacements were taken to be positive. Assuming the LOS changes of the two sensors are identical (which is roughly the case in Figure 2-4), and no north-south displacement U_{ns} , the constraint on the east-west and up-down displacements can be derived as $U_{ew}:U_{ud} = 0.032:1.156$. The assumption of zero U_{ns} might appear unrealistic but can be reasonable over the east- and west-facing slopes, which incidentally cover a broad area of the fire scar. As this

constraint indicates the dominance of vertical displacement, we can infer that slope-parallel sliding did not take place over the east- and west-facing slopes.

In the thawing season when the vertical displacement is downward (negative), the previous constraint on the two displacements also indicates that the east-west displacement should always be westward (negative), regardless of the slope. As this is physically implausible, we may assume that east-west displacements were virtually zero over both the east- and west-facing slopes. We can thus infer a pure vertical subsidence without any east-west displacements during the thaw season. Hence, the differences between ALOS-2 and Sentinel-1 in the thawing seasons (Figures 2-5a and 2-5b) will be simply equal to $-0.032U_{ud}$. Therefore, we can expect systematically positive differences in the thawing season, regardless of the east- and west-facing slopes, which appear consistent with observations (Figures 2-5a and 2-5b). Quantitatively, however, the mean differences of 0.5-0.7 cm are too large to be attributable to the geometric difference alone, on account of the subsidence by as much as 5 cm or more. Here, we hypothesize the possible impact of soil-moisture changes, which can reach $\sim 10\%$ of the carrier wavelength (Zwieback et al., 2015, 2016). As changes in soil moisture generate larger apparent LOS changes in L-band than in C-band InSAR, the observed differences can be likely.

In contrast to thaw subsidence frost-heave is more likely to occur towards the slope normal direction. Assuming the magnitude of slope-normal uplift, U_f , over a slope with gradient θ , the differences between ALOS-2 and Sentinel-1 would be $U_f(1.156\sin\theta - 0.032\cos\theta)$ assuming zero U_{ns} . We estimated $|\theta| = 1.58^\circ$, which corresponds to 55 m height difference over 2 km horizontal distance and was fairly consistent with the slope of the studied area. Meanwhile, the differences can also be considered $1.156U_{ew} - 0.032U_{ud}$, which indicates additional positive and negative effects on the east- and west-facing slope, respectively. Indeed, Figure 2-5c appears to depict clearer contrasts in sign on the east- and west-facing slopes. Moreover, the impact of changes in soil moisture are likely

much smaller in the colder season than in the thaw season, which may explain the smaller differences in freezing seasons.

As we derived the differences over the no-deformation season (Figure 2-5d), we can attribute them to the atmospheric effect on ALOS-2 and Sentinel-1 interferogram (Figures 2-4d and 2-4i). The overall positive differences are likely because the spatial scale of atmospheric delay was greater than the fire scar area.

Previous reports of thermokarst subsidence after fire have focused on relatively flat areas as those at the 2002 tundra fire in the central Seward Peninsula, Alaska (Iwahana et al., 2016b), the 2007 Anaktuvuk River tundra fire (Liu et al., 2014; Jones et al., 2015; Iwahana et al., 2016a), and the 2009 Big Creek Fire in the Alaskan Yukon River basin (Molan et al., 2018). As such, in addition to the broad subsidence detected by InSAR, polygonal patterns associated with ice wedge degradation became clearly visible 4-7 years after the fire by high-resolution optical and LiDAR remote sensing (Jones et al., 2015; Iwahana et al., 2016b). At the studied hillslopes, in contrast, no such polygonal patterns are likely to be detected. Nonetheless, the dominance of vertical displacements with little slope-parallel sliding indicate that rapid active-layer detachment sliding (ALDS) events were insignificant. In contrast, many ALDS events triggered by fire have been mapped at Mackenzie Valley, Canada, whose length could sometimes reach hundreds of meters (Lewkowicz and Harris, 2005). If ALDS event with such length occurred, we could have observed significant loss of interferometric coherence. It is possible, however, that local ALDS events occurred but were undetected because of the coarse resolution (~10 m) of InSAR images. Because the subsidence was caused by thawing of ice-rich permafrost, meltwater should have been supplied at the base of active layer. Considering the mechanisms of ALDS (Lewkowicz, 2007), porewater pressure increase might have been not enough to reduce the effective overburden stress and to initiate significant slope-parallel sliding. This is

possibly because the meltwater could have drained through the gullies. However, in view of the significant uplift signals over the burned area even years after the fire, the meltwater is still likely to be undrained on the slope. If there were further enough water input by, for instance, warmer days and/or heavy rain, significant ALDS events may take place in the future.

2.5.2 What controls the heterogeneous distribution of subsidence magnitude? Possible emergence of another megaslump

The cumulative subsidence magnitude was spatially variable but showed some systematic changes. In addition to the ridges and peaks the west-facing slopes showed significantly smaller subsidence than the east-facing slopes (Figures 2-4 and 2-8a). To interpret the spatially heterogeneous subsidence, we associated burn severity and local landform with the cumulative subsidence (Figure 2-8). In light of the inferred dNBR (Figure 2-8b), which ranged from 0.2 to 0.4, the burn severity was moderate rather than high. Also, the burn severities were spatially less heterogeneous than those of cumulative subsidence and local landform. In fact, we could even identify deformation-free areas having even higher burn severity. Thus, although the fire undoubtedly initiated the subsidence, the burn severity did not control the subsequent cumulative magnitude.

Notably, however, gullies were clearly more developed on the east-facing slopes than on the west-facing slopes (Figure 2-8c), which were confirmed to be present at least back in 1991 by Landsat image. Considering the striking correlation between the development of gullies and the larger subsidence, there is high likelihood of a causal relationship between them. Similar dependence on the slope aspect was reported by Lacelle et al (2010, 2015), who found that hillslope thaw slumps in the Richardson Mountains–Peel Plateau, northwest Canada, predominantly developed on the east-facing slope. Lacelle et al (2015) interpreted that the active layer on the east-facing slope might be thinner because of lower amount of insolation than on the south- and west-facing slopes, which promoted a

triggering mechanisms of thaw slumps because the ice-rich permafrost was closer to the surface. Although the broadly subsiding areas are not so-called thaw slumps, thinner active layers on the east-facing slope are likely and can consistently explain both the larger subsidence and the rich development of gullies. This hypothesis can be tested either by examining the surface deformations at the 2018 and 2019 fire scars and other fire scars across Siberia and other boreal regions or by performing field-based thaw-depths measurement.

The recent slowdown of the subsidence rate (Figure 2-9) may suggest that the 2014 fire scar could stabilize in the near future. However, although it depends on how quickly the vegetation is recovered, we do not preclude the possible emergence of another megaslump particularly on the east-facing slopes. In order to initiate thaw slumps, ice-rich permafrost needs to be exposed at the surface (Kokelj and Jorgenson, 2013), at which the initial headwall and slump floor are formed. In contrast to the thaw slumps near shorelines, coastlines and riverbanks (e.g., Burn and Lewkowicz, 1990; Kokelj et al., 2009), no mechanical erosions by waves and currents are effective on hillslopes like the studied area. For the development of retrogressive thaw slumps (RTS) on hillslopes, Lacelle et al. (2010) suggested that ALDS triggered by meteorological events could remove the overlying active layer and expose the ice-rich permafrost. Although no large-scale ALDS events were detected during the studied period, they might take place as discussed in the previous section. Moreover, Figure 2-8a indicates that the subsidence magnitude becomes larger toward upslope, and there are clear boundaries between the subsiding and non-subsiding portions, where an initial headwall for RTS could be exposed. Once an initial headwall has formed, subsequent retreat rate is rapid on the order of several meters per year (Burn and Lewkowicz, 1990; Lacelle et al., 2015). Thus, in order to monitor the early formation process of RTS in more detail, long-term radar remote sensing with higher spatial and temporal resolution would be necessary and promising.

2.5.3 Interpretation of frost-heave signals

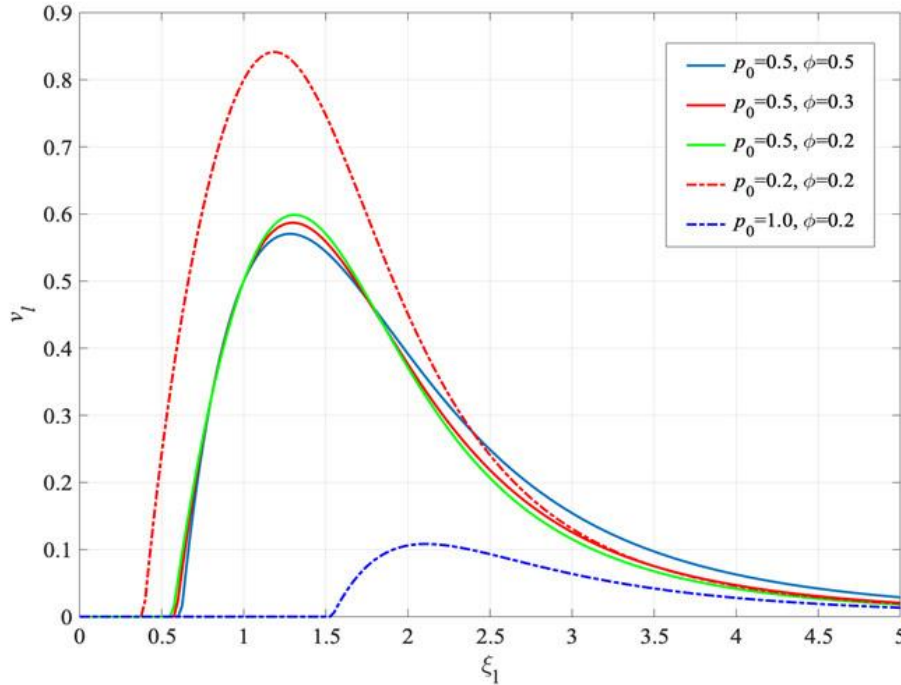


Figure 2-10. Non-dimensional heave rate profiles of an ice lens as a function of its boundary position, based on the analytical model by Rempel et al (2004). Five cases of non-dimensional overburden pressure p_0 and porosity ϕ are shown.

In order to interpret the detected frost heave signal on the basis of the theory by Rempel et al (2004), we first examine the sensitivity of the heave rate on the normalized overburden pressure p_0 and porosity ϕ . Figure 2-10 shows five cases of non-dimensional heave rate profiles as a function of the ice lens boundary position ξ_l , indicating that the maximum heave rate is mainly controlled by the normalized overburden pressure p_0 and is somewhat insensitive to the porosity ϕ . Details of the heave rate profiles will depend on the assumed models of permeability and ice saturation, but the qualitative characteristics are not altered (Rempel et al., 2004). There exist two positions that give the same heave rate, but only the branch with smaller ξ_l is stable (Worster and Wettlaufer, 1999; Rempel et al., 2004).

We can attribute the clear contrast in the frost heave signals inside and outside the burned area to the differences in the normalized overburden pressure p_0 . Because the mechanical overburden pressure P_0 will not significantly differ from the inside to the outside of the burned area, the larger frost heave rate in the burned area would be caused by larger temperature gradient G and/or deeper frozen depth z_f . Owing to the removal of vegetations and surface organic layers over the burned area, the larger temperature gradient G than that of the unburned area is likely more marked in the early freezing season and may generate a greater thermomolecular force that will effectively reduce the normalized overburden pressure. We may also interpret the absence of frost heave signals in mid-winter as due, probably, to the smaller temperature gradient G than that in late fall/early winter; if frost heave were controlled by temperature instead of temperature gradient, we would expect even more significant signals during the much colder part of the season. The deeper frozen depth z_f is also likely due to the loss of surface vegetation and should supply more water for frost heave.

From the end of September to the middle of November 2017, Figure 2-6 shows LOS changes by approximately 1.5 cm over 12 days toward the satellite that corresponds to an approximate 1.9 cm uplift. Assuming a constant-rate frost heave, this corresponds to a heave rate of 1.8×10^{-8} (m/s). The most critical parameter controlling heave rate is the permeability for ice-free soil k_0 , which can vary by orders-of-magnitude, while other parameters are well-constrained. We may fit our observed heave rate with the ice-free permeability, $k_0 \sim 10^{-17}$ (m²), which is a likely value in view of the three cases in Rempel (2007).

Here we comment on the modeling of uplift signals as caused by in situ freezing of pore water into ice (Hu et al., 2018). The in situ freezing model is simple, and can explain the timing, duration, and magnitude of uplift signals, if one assumes such pore water in the active layer. However, because the Stefan function approach in Hu et al (2018) is essentially controlled by atmospheric (or

ground) temperature that is rather homogeneous over this spatial scale, it is difficult to account for the observed heterogeneous distribution of uplift signals. The distribution of uplift signals was closely correlated with that of subsiding signals, which led us to interpret that the permafrost thaw and its incomplete drainage could become a water reservoir for ice lens formation and frost-heave. The frozen pore ice within the soil and the ice lens formed by water migration are totally different in terms of their formation mechanisms and subsequent forms of ice. From a geomorphological perspective, the presence of ice lenses will play a role in reducing the strength of soil and potentially initiating ALDS, because porewater pressure will increase at the front of thawing, whereas pore ice within the soil would simply stay as pore water with little impact on the landform.

We also recognize, however, that the microphysics-based theory adopted in this study is developed in 1-D geometry and is based on the assumption of “frozen fringe”, a region where liquid freezes into ice through the pores of soil. Some laboratory experiments did not support the presence of frozen fringe (e.g., Watanabe and Mizoguchi, 2000), and the “fringe free” frost heave theory has also been proposed; see Peppin and Style (2013) for review. In addition to the controlled lab experiments and theoretical developments, more detailed observations of natural frost heave signals are becoming possible and might help better understand the physics of frost heave and its geomorphological consequences.

2.6 Report of on-site observation in 2019

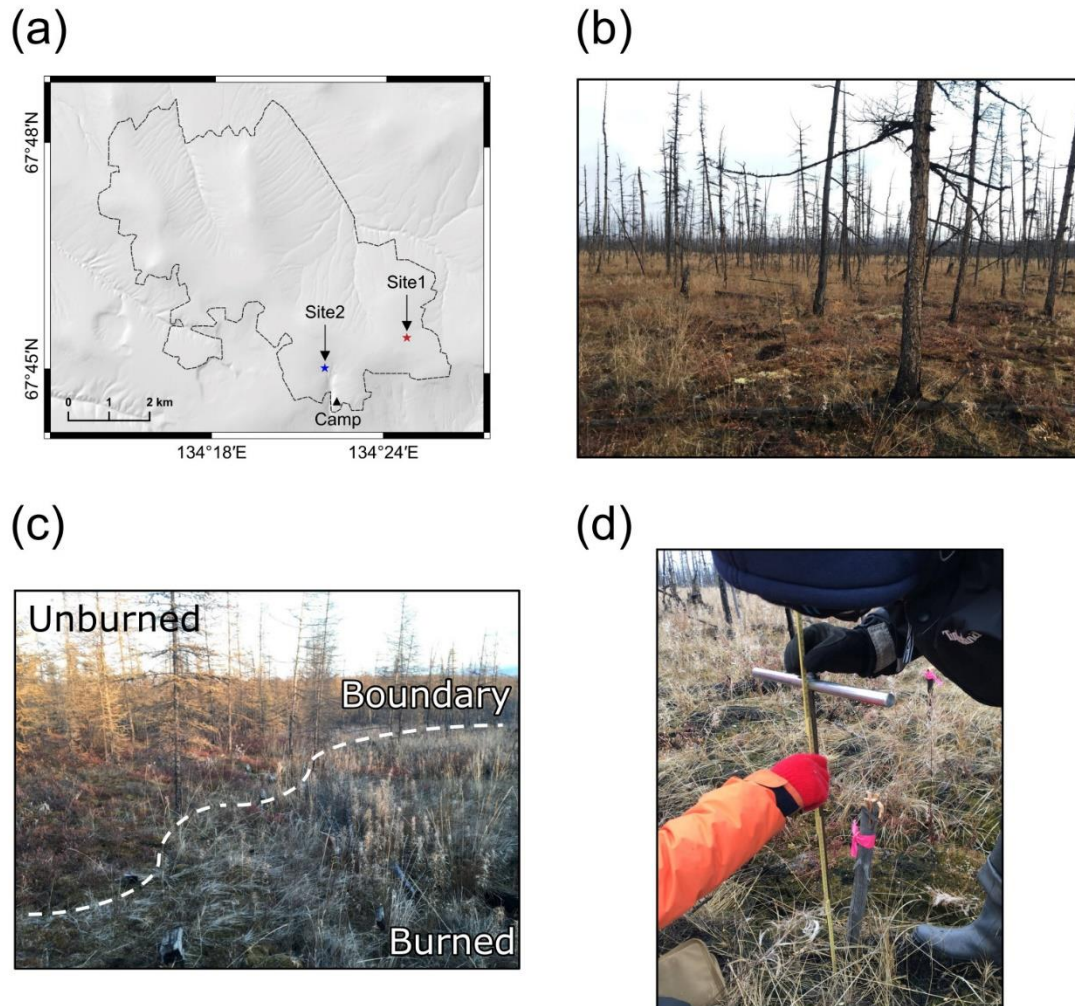


Figure 2-11. (a) Map of on-site observation conducted from 20 to 22 September 2019 with shaded relief image derived by DEM. The red and blue stars indicate the location of thaw depth measurement sites. The black triangle indicates the location of the camping. (b) Picture of the Site1. (c) Picture of the Site2. The white dash line indicates the boundary between burned and unburned areas. (d) Picture of thaw depth measurement at Site1. All pictures were taken on 21 September 2019.

We conducted on-site observation at the 2014 scar from 20 to 22 September 2019 to observe thaw depth, soil temperature, elevation, and surface condition five years after the fire. The location of observation is shown in Figure 2-11a. Here, we report the thaw depth data measured at Site1 (Figure 2-11b) and Site2 (Figure 2-11c). Site1 is in the east part of the 2014 scar, where InSAR images showed a large displacement signal. Site2 is located in the south part of the 2014 scar. The unburned area remained around Site2, and we observed thaw depth across the burned and unburned area. The thaw depth data was corrected by a metal rod with accuracy in centimeters. We manually probed the rod vertically and measured depth from ground surface to frost table. In addition, we set the logger to measure the temporal change of soil temperature at Site1. In the future, we will extract the logger data and conduct second leveling to measure relative height change.

The mean thaw depth values are 124 cm at Site1, 123 cm at Site2 burned area, and 45 cm at Site2 unburned area (Figure 2-12). The 2014 fire deepened the thaw depth by about 80 cm compared to the unburned area. In addition, the data briefly indicated the correlation between the large amplitude of the seasonal deformation in the InSAR image and thaw depth at the Site1 and Site2 burned area. It suggests an increase in ice lens formation within the deepened active layer. On the other hand, the amount of secular subsidence settled down in 2019. It suggests that summer temperature is unlikely to thaw the layer below ~140 cm due to the soil thermal conductivity. We need to monitor how long it takes vegetation to recover and the associated ground deformation process. Until the surface vegetation recovers, the amplitude of the seasonal deformation will remain larger than that of the surrounding unburned area.

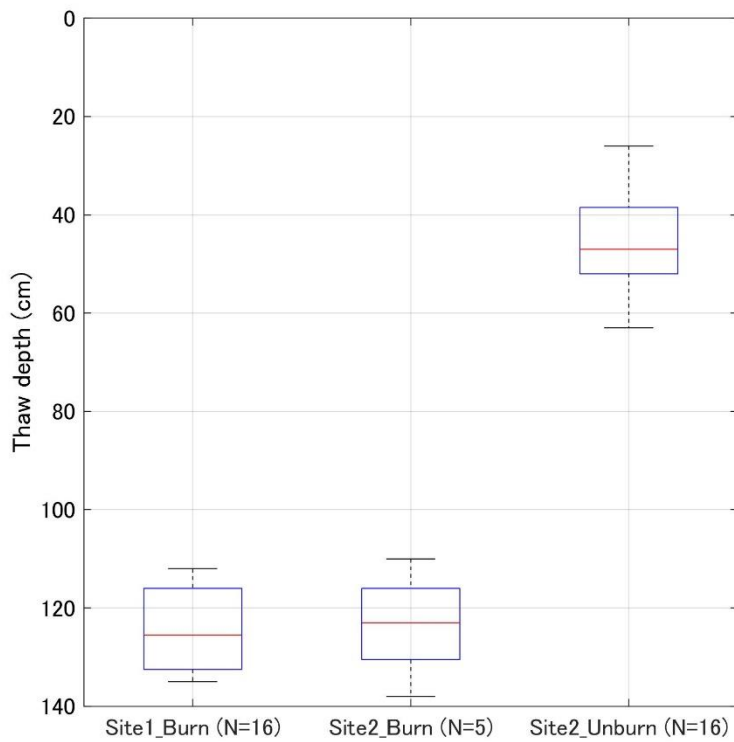


Figure 2-12. Thaw depth data measured on Site1 and Site2 in the 2014 scar. The location of both sites is shown in Figure 2-11a. The black bars indicate min and max values. The red bar indicates the median value. The blue box indicates the range from lower quartile to upper quartile.

Chapter 3

Transient Freeze-Thaw Responses to the 2018 and 2019 Wildfires near Batagaika Megaslump, NE Siberia

The contents of this chapter are now in preparation to be submitted.

Yanagiya, K., M. Furuya, G Iwahana, P. Danilov (2022) Transient Freeze-Thaw Responses to the 2018 and 2019 Wildfires near Batagaika Megaslump, NE Siberia, Inferred from InSAR and On-site Observations, in preparation.

Chapter 3. Transient Freeze-Thaw Responses to the 2018 and 2019 Wildfires near Batagaika Megaslump, NE Siberia

3.1 Introduction

Wildfire in Arctic region is responsible for rapid and extensive thawing of near-surface permafrost because thermal insulation effects by the vegetation cover are substantially lost (e.g., Yoshikawa et al., 2003). Holloway and Lewkowicz (2019) have reported that the progression of permafrost thawing in a fire scar depends on the thickness of the remaining organic layer. As it takes several years for the vegetation to recover, permafrost thawing can last for years and change the local terrains, known as a thermokarst process (Holloway et al., 2020). Moreover, the number of wildfires and burned areas are increasing in the Arctic region in recent decades (Gillett et al., 2004; Kasischke et al., 2010; Ponomarev et al., 2016), and thus they could even more accelerate permafrost degradation particularly in ice-rich permafrost regions. Furthermore, as permafrost in high-latitude regions stores twice as much carbon as in the atmosphere, its thawing can enhance microbial decomposition of organic carbon and result in greenhouse gas emissions such as CO₂ and CH₄, known as permafrost carbon feedback (Tarnocai et al., 2009; Shuur et al., 2015).

Monitoring fire location and burned areas is nowadays near operational thanks to satellite remote sensing by optical and infrared sensors (e.g., Parkes et al., 2014). Nevertheless, it has been uncertain how much volume of permafrost thaw was caused by wildfires because of their remote locations and underground substance. However, it has become possible to estimate the thawed volume by measuring topography changes with the use of satellite-based microwave interferometric synthetic aperture radar (InSAR) images (e.g., Liu et al., 2014; Iwahana et al. 2016; Molan et al., 2018; Yanagiya and Furuya, 2020). In the previous studies of post-wildfire deformation mapping, however, there has been one issue known as the loss of interferometric coherence before and after wildfires because of the dramatic changes in the microwave scattering characteristics (Liu et al., 2014; Molan et al., 2018). As a result, no previous studies have demonstrated how much surface displacements occurred before

and after the fires at the fire scars. Thus, to our knowledge, all previous post-wildfire deformation mapping by InSAR has been done using only post-wildfire images, and it has been uncertain if significant permafrost thaw occurs in the burned year before freezing season or in the next year after initiation of the next thawing season. We first show below our successful detection of post-wildfire deformation, using pre- and post-wildfire images both acquired in winter.

We focus on two fire scars formed in 2018 and 2019 in Batagay village, Sakha Republic, Northeastern Siberia. The two fire scars are located adjacent to the Batagaika megaslump, the world largest retrogressive thaw slump, located about 10 km southeast of the village (Figure 3-1). The periods of the 2018 and 2019 fires are from 4 to 6 August 2018 and from 12 to 23 July 2019, respectively. Both fire scars are located on the same slope as the Batagaika megaslump, which is gently dipping toward the northeast, and the slope becomes nearly flat at the Batagay river. As the formation of the Batagaika megaslump was initiated by deforestation and subsequent erosion on a small gully in the 1970s (Kunitsky et al., 2011), it is possible that the nearby wildfires could trigger another formation of megaslump. It is thus urgently important to keep monitoring if and how the topography will change after the fires using modern remote sensing techniques.

The first purpose of this paper is to report the freeze-thaw amount immediately after the fires, using two independent InSAR data. It would be the first successful detection of pre- and post-fire displacements by coherent InSAR image, as there have been no similar reports, to our knowledge. The second purpose is to show the ground-based thaw-depth measurement data that will complement and help our interpretations on the InSAR data. These observations and interpretations have implications for the understanding of the post-fire thaw processes.

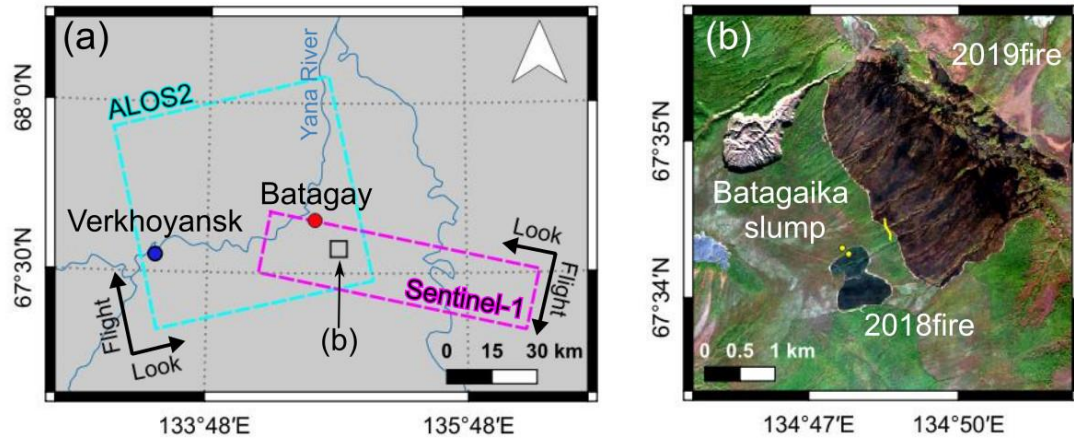


Figure 3-1. (a) Map around Batagay. Cyan and magenta dashed-box indicate imaging areas of ALOS2 and Sentinel-1, respectively. (b) Map of the wildfires located very close to the Batagaika megaslump from Sentinel-2 image on 31 August 2019. The small-western scar was burned in 2018, and the large-eastern scar was burned in 2019. Yellow points and line are the field observation sites in 2019 and 2020.

3.2 Data and Method

3.2.1 SAR data

InSAR is a space geodetic technique to detect the relative ground deformation in the imaged area as phase changes between two imaging periods (see Massonnet & Feigl, 1998; Bürgmann et al., 2000; Simons & Rosen, 2015). This study used two types of SAR data. One is the ALOS-2, the JAXA's L-band SAR satellite, for detecting one-year deformation; another is the Sentinel-1, the ESA's C-band SAR satellite with a 12days imaging interval. We used the GAMMA software, version 20200728 (Wegmüller & Werner, 1997), to generate differential interferograms for each satellite data. The DEM data to remove topographic fringe was ArcticDEM 10 m mosaic (Porter et al., 2018), which is fine enough for the spatial resolution of present InSAR images. Also, we used QGIS version 3.10.8 to stack the interferograms and generate deformation maps.

InSAR image contains long-wavelength noises due to troposphere and ionosphere in addition to ground deformation signal (Goldstein, 1995; Gomba et al., 2016). In order to reduce them, we fit all the phase-unwrapped InSAR images with a quadratic polynomial and subtracted the calculated trend. This method could also subtract spatially homogenous ground deformation across the image known as “isotropic thaw subsidence” (Shiklomanov et al., 2013). After removing the long-wavelength trend, the phase change is close to zero outside the fire scars. Therefore, we only discuss the ground deformation in fire scars relative to the unburned area.

So far, a winter InSAR image over a snow-covered area has been known to lose its coherence due to the changes in scattering processes, such as from ground surface scattering to volume scattering within a snow layer (Tsai et al., 2019). The coherence loss is particularly serious for wet snow. On the other hand, for dry snow, it was reported that microwave could penetrate the snow layer about several meters, and a satellite could receive backscatter from the ground surface (Rignot et al., 2001). Dry snow does not cause a coherence loss but can generate a phase delay due to changes in snow water equivalent (SWE) (Gunteriusen et al., 2001). Since this study removes the long-wavelength trend, we can ignore the effect of spatially uniform changes in SWE. Yanagiya and Furuya (2020) confirmed that the displacements obtained from winter pairs with nearly the same period were consistent in both L-band and C-band InSAR images at the 2014 fire scar, 15 km northwest from Batagay. Since the phase delay due to SWE change depends on the microwave wavelength, the consistency between L- and C-band InSAR images demonstrate that the signal was not substantially affected by the local SWE distribution but the real ground deformation. InSAR data is a projection of the real 3D displacements onto the radar Line-Of-Sight (LOS) direction. Now, the ALOS-2 illuminates the surface from west to east with 38.0 degrees of incidence angle, whereas the Sentinel-1 does from east to west with 38.7 degrees of incidence angle (Figure 3-1); InSAR data is most sensitive to the vertical displacement and insensitive to the north-south displacement because of near-polar orbit. We stack several Sentinel-1 InSAR images to match the measurement interval to that of the ALOS-2 InSAR image and compare

the seasonal deformations. Despite the different illumination directions of both satellites, the derived InSAR LOS changes in both satellites are consistent in terms of the spatial pattern in LOS changes, which indicates that the vertical displacements dominate the LOS changes.

3.2.2 Thaw Depth Measurement

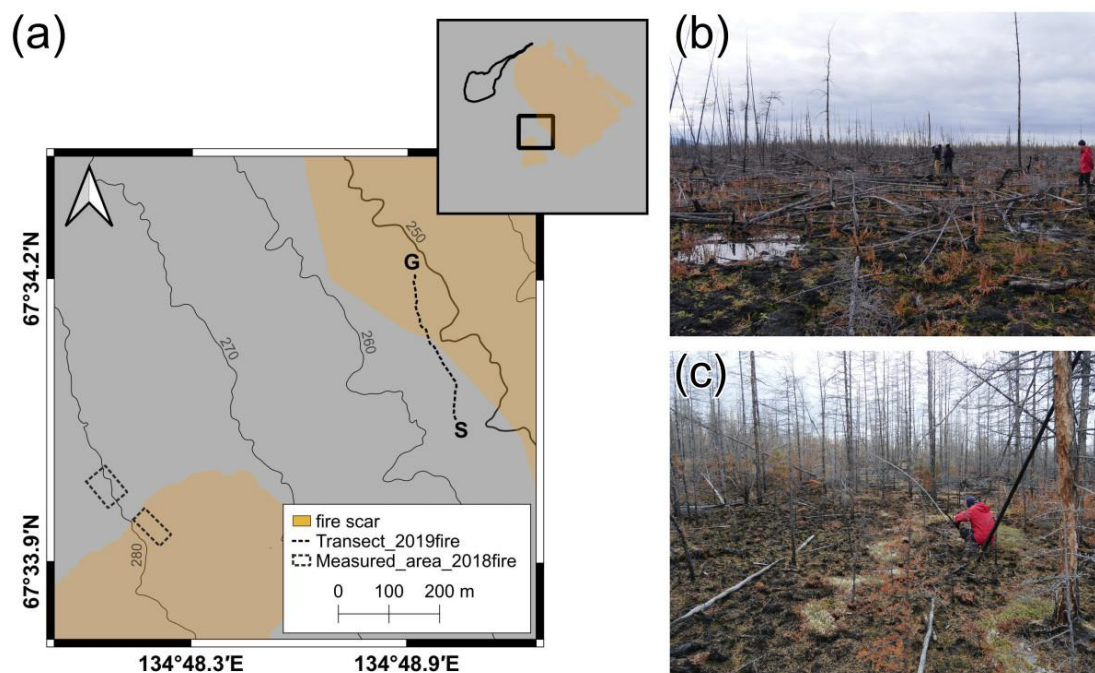


Figure 3-2. (a) The map of field observation areas. Orange areas are the 2018 and 2019 fire scars, black dashed squares indicate the measurement areas, and the black dashed line indicates the transect near the boundary of the 2019 fire scar. (b) The situation of the 2018 fire scar on 23 September 2019. (c) The situation of the 2019 fire scar on 23 September 2019.

We measured thaw depths by manually inserting a frost probe at the 2018 and 2019 fire scars at the end of summer season when thaw depth becomes the deepest in a year. Figure 3-2a shows the detailed location of the measurement area. The first measurement was done on 23

September 2019, the second on 12 September 2020, and the third on 17 September 2021. At the 2018 fire scar (Figure 3-2b), we randomly measured thaw depth at 50, 20, and 30 points in about 70×30 m area in 2019, 2020, and 2021, respectively (Figure 3-2a). The adjacent unburned area was a control site, and we measured the same number of the points as the burned area in about 70×50 m area each year.

Moreover, we set up a linear 300 m transect (Figure 3-2a) that starts from the unburned control site (S) and ends inside the fire scar (G; Figure 3-2c) and measured the thaw depth along with the transect. The total measurements are at 53 points in the fire scar and 59 points in the control site, and we averaged them respectively in 2019. In 2020 and 2021, we measured them again but with a reduced number of points due to the limited time and averaged 27 points in the fire scar and 30 points in the control site, respectively.

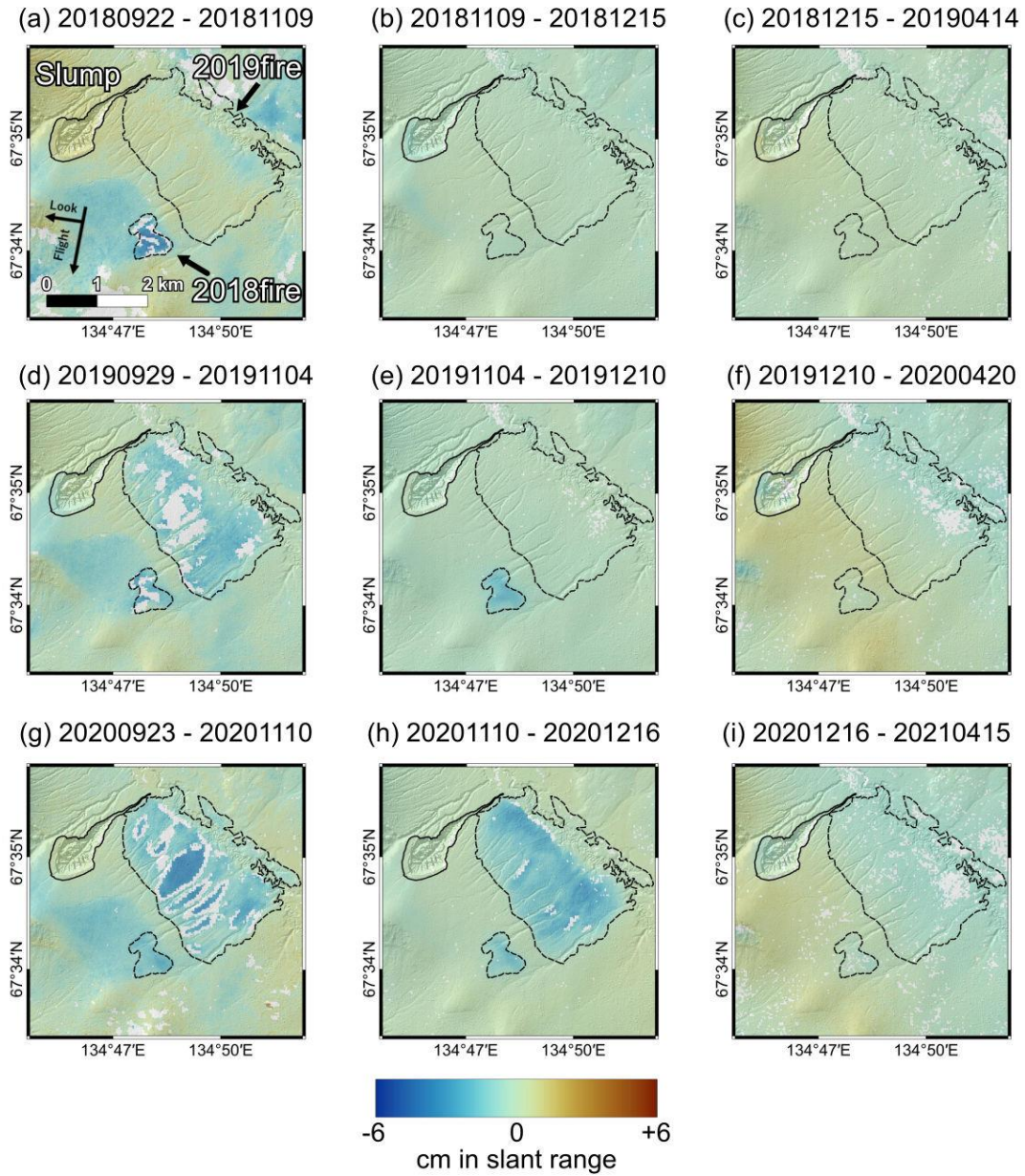


Figure 3-3. Frost heave maps derived from stacked Sentinel-1 InSAR images (from yyyyymmdd to yyyyymmdd). The left (a,d,g), central (b,e,h), and right (c,f,i) columns are early, mid, and late winter, respectively. Warm and cold colors indicate the subsidence and uplift in the LOS direction, respectively. The black line is the Batagaika megaslump shown in the Sentinel-2 optical image on 21 June 2020. The west and east black dashed lines are the fire scars burned in 2018 and 2019, respectively.

3.3 Results

3.3.1 Seasonal frost heave immediately after the wildfires

Figures 3-3 shows seasonal frost heave maps during early, mid, and late winter in 2018, 2019, and 2020, derived by concatenating several Sentinel-1 InSAR images. We compare the seasonal frost heave signals during the three years; the original 12 days interval InSAR images are shown in Figures 3-4, 3-5, 3-6. First, early winter covers from mid-September to early November when the air temperature drops below the freezing point and the frost heave starts. We can point out clear frost heave signals in the diamond-shaped area outside of the 2018 scar that repeats every year but occurs only in the early winter (Figures 3-3a, d, g). The low-elevation area inside the north-eastern portion of the 2019 scar has a similar deformation pattern before the fire (Figure 3-3a). Sentinel-2 images indicate that these areas commonly have fewer trees (Figure 3-11).

Meanwhile, the impact of wildfire during the burn year is observed as frost heave signals in Figures 3-3a and d for the 2018 and 2019 fires, respectively. Figures 3-4m, n, and o indicate that the frost heave at the 2018 scar precedes that at the diamond-shaped area. The amplitude of the heave signal is apparently larger in the fire scars than that in unburned areas. Figure 3-3a shows up to 6 cm uplift occurred in the early winter at the 2018 scar, whereas some pixels are missing due to phase unwrapping error due to low coherence. We can again observe the uplift at the 2018 scar during the early winter in 2019 and 2020 (Figures 3-3d, g), but the amplitude was not as large as observed in 2018 (Figure 3-3a). Figure 3-3d also tells the impact of the 2019 fire in the same year. Compared to Figure 3-3a, we can observe clear uplift signals except for the low-elevation portion where uplift signals were detected already in 2018, as mentioned above. In 2020, the uplift amplitude at the 2019 fire scar became larger in places than the previous year (Figure 3-3g).

Mid winter covers from November to December when the air temperature drops below -30 °C. We did not observe any significant uplift signals outside the burned areas during the mid winter (Figures 3-3b, e, and h). Moreover, the heave amplitude extends depending on the elapsed time since the fire episode. Figures 3-3b and e show that the first post-wildfire heave ended before mid winter at the 2018 and 2019 scar, respectively. However, at the 2018 scar in Figure 3-3e, the second year's post-wildfire heave by up to 2.7 cm uplift was still lasting. Namely, the heave duration gets longer in the next year than the previous burned year. In Figure 3-2h, up to 4.0 cm uplift occurs in both the 2018 and 2019 scars with the exception again at the low-elevation portion of the 2019 scar. Therefore, the heave map in the mid winter demonstrates that the frost heave duration is extended at the fire scars in the second year after the fires; we will discuss the possible mechanism with reference to the ground-based thaw depth measurements.

The late winter covers from December to April, with the air temperature dropping below -40 ~ -50 °C. Figure 3-3c shows no significant differences in the LOS amplitude between the burned and unburned areas, suggesting that the thawed layer during the summer was completely frozen until the late winter. On the other hand, despite the different acquisition dates, Figures 3-3f and i seem to show broad but consistent “subsiding” signals at the western portion of the area with the exceptions of the 2018 scar and the megaslump. We speculate that the apparent subsiding signals could be due to the temporal changes of non-uniform SWE toward the later winter, but the true origins are uncertain.

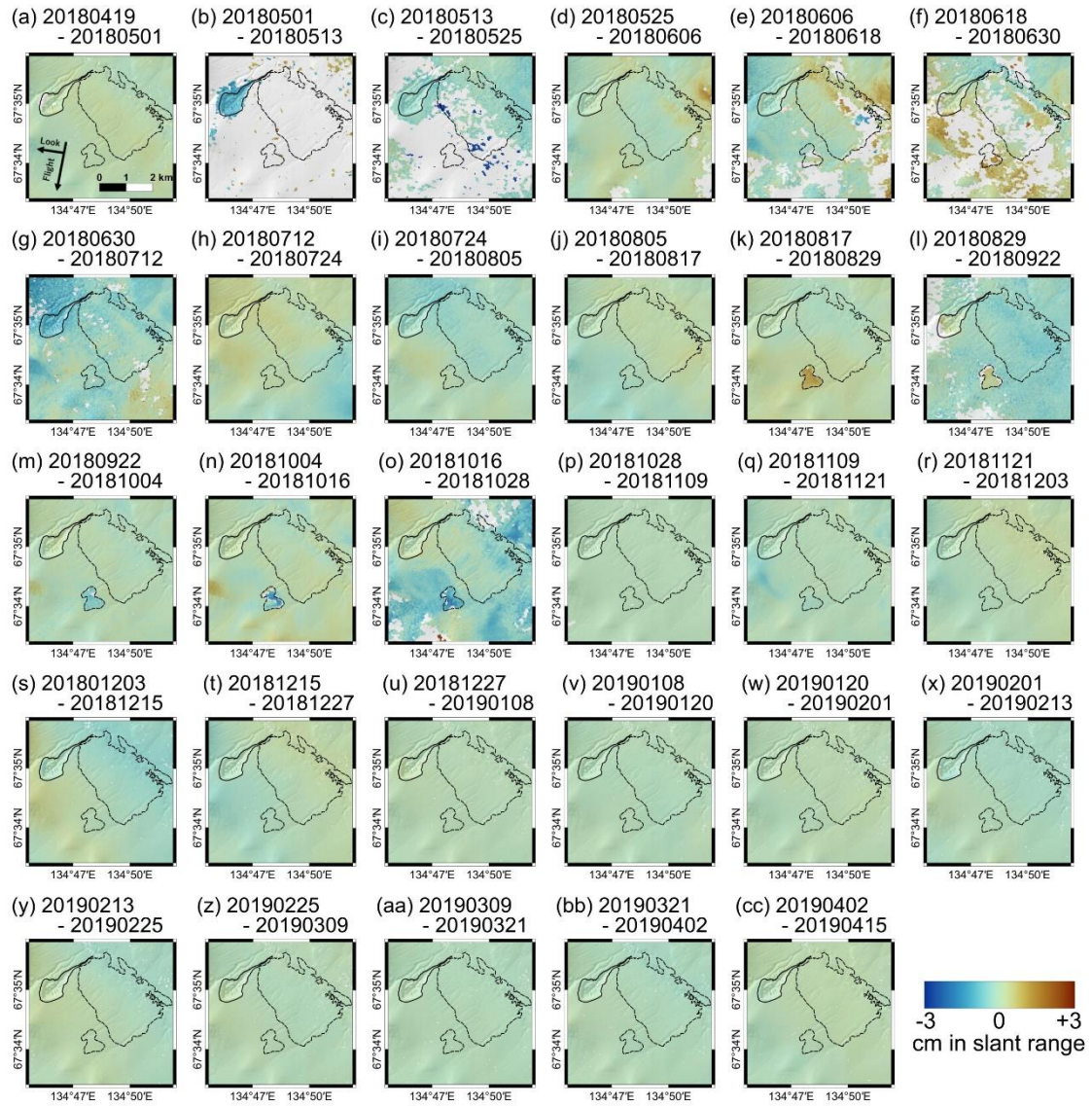


Figure 3-4. Sentinel-1 InSAR images before stacking in 2018-2019.

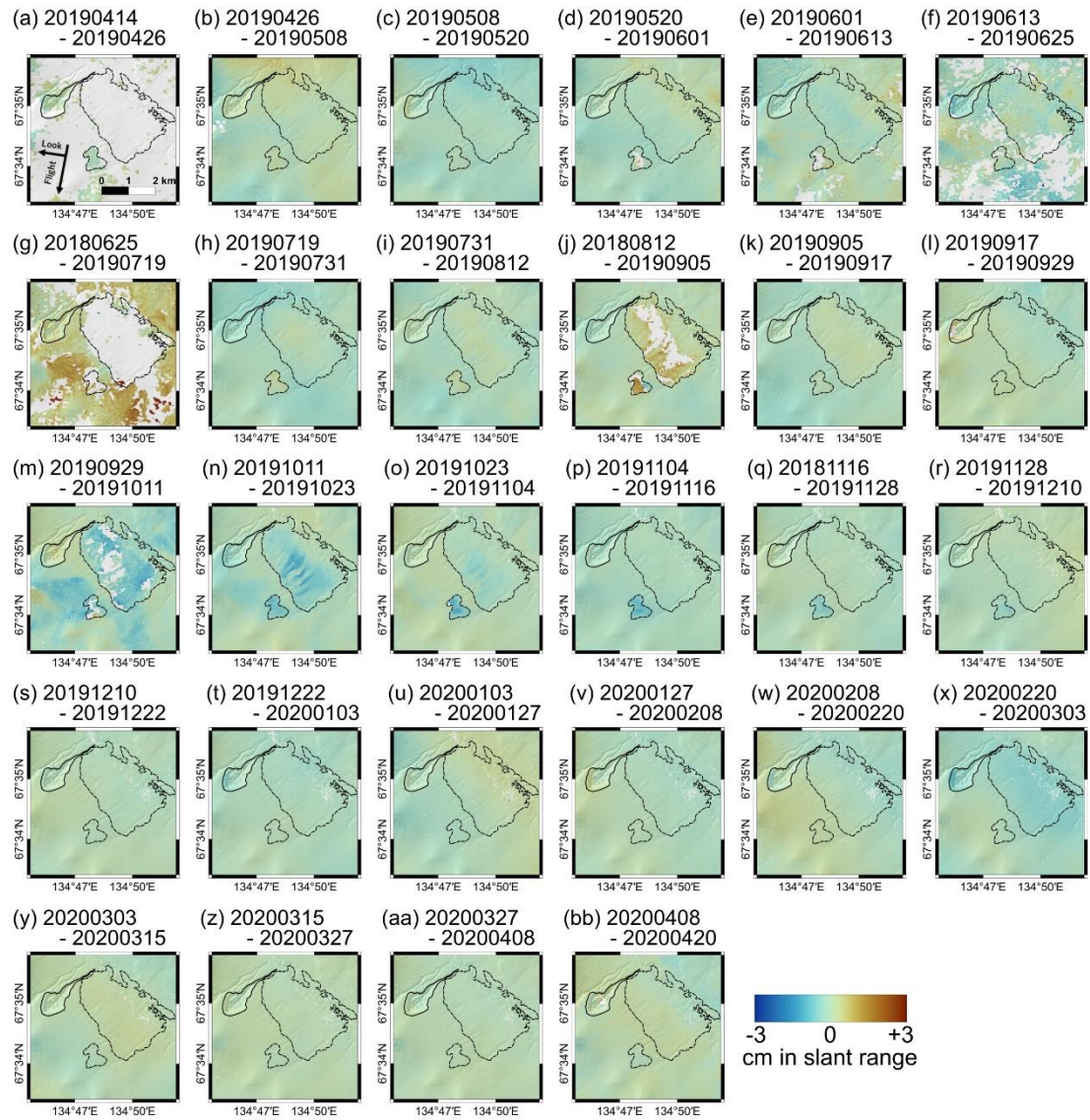


Figure 3-5. Sentinel-1 InSAR images before stacking in 2019-2020.

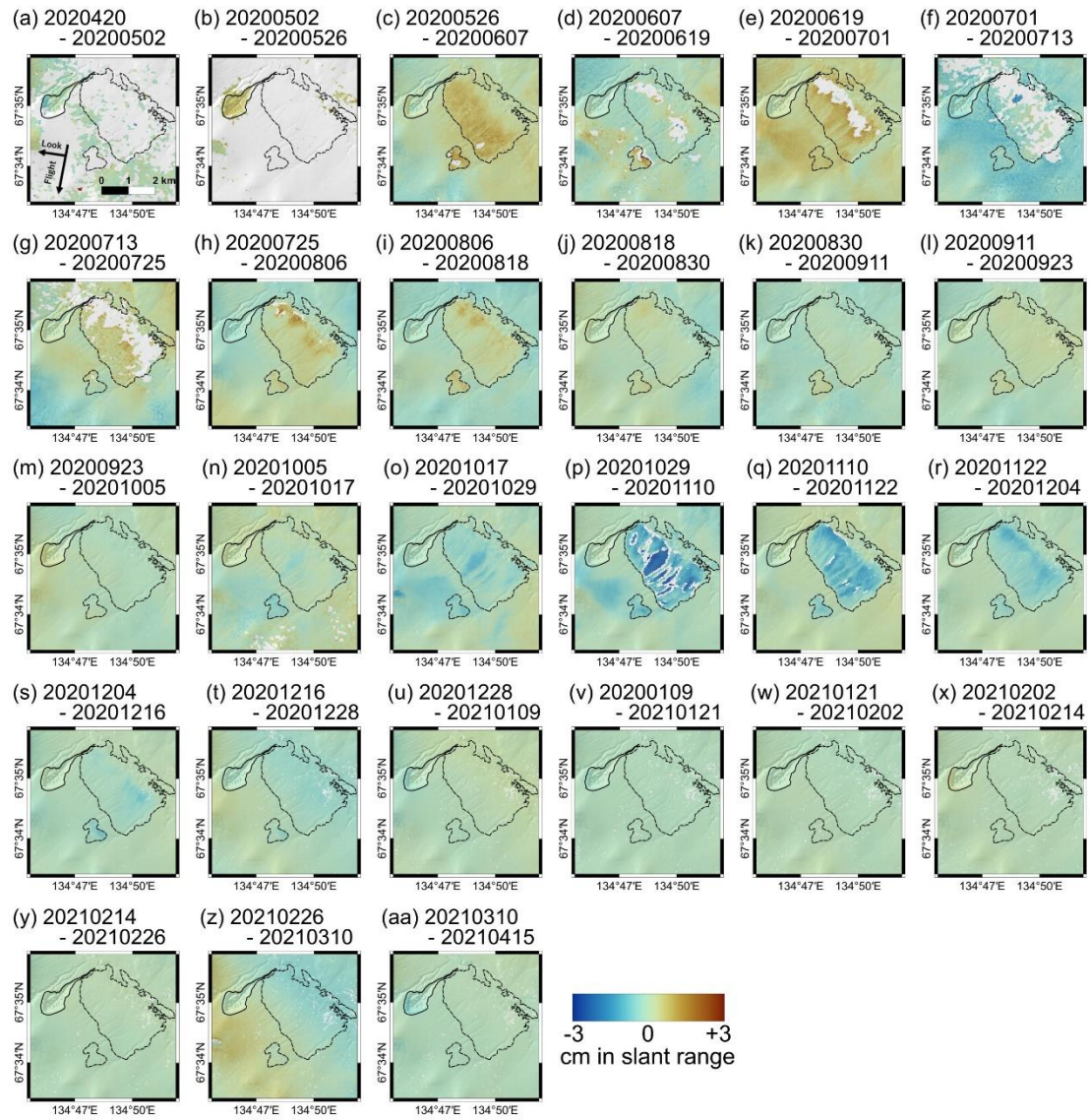


Figure 3-6. Sentinel-1 InSAR images before stacking in 2020-2021.

3.3.2 Annual total ground deformation in a burned year

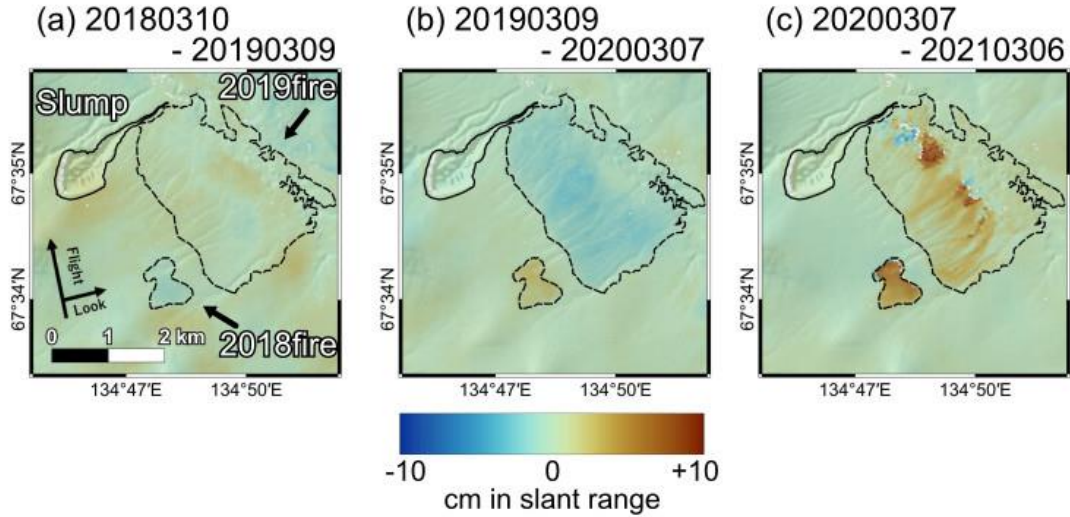


Figure 3-7. ALOS-2 InSAR images covering one year (from yyyyymmdd to yyyyymmdd). Figures (a), (b), and (c) are total LOS changes, starting from March 2018, 2019, and 2020, respectively. LOS changes toward the satellite, meaning an uplift, are detected in the 2018 and 2019 scars in the burned year. Phase unwrapping errors cause some discontinuous phase changes in (c).

Figures 3-7a, b, and c are ALOS-2 InSAR images that cover one year from March 2018, 2019, and 2020, respectively. In previous studies, an InSAR image, when it includes a fire period, has lost interferometric coherence between primary and secondary images (e.g., Liu et al., 2014; Molan et al., 2018), and no deformation data between pre- and post-fire period were available. However, in the study area, the coherence of a one-year InSAR image with the March data is higher than that of the image with the June data (Figure 3-8); the coherence was derived from the non-filtered interferogram and intensity images. Although the fire scars show lower coherence than unburned sites in Figure 3-8, the March pairs maintain higher coherence than the June pairs (Figures 3-8a and d in 2018; 3-8b and e in 2019). The March pairs also have higher coherence than the June pairs in the unburned area, suggesting that there is no volume scattering due to snow cover in the unburned area (Figures 3-8a

and d in 2018; 3-8b and e in 2019). Note that the interferograms in this thesis are the image after adaptive filtering. After smoothing out the local phase noise, they reveal even better coherence in all periods. Therefore, the one-year InSAR image can tell the annual total deformation signal even when the temporal coverage includes the fire period.

Moreover, the one-year InSAR images are helpful to show if either the net subsidence by permafrost thaw or uplift is dominant annually because seasonal subsidence and uplift can be canceled out. Indeed, it is important to note the absence of significant signals at both the diamond-shaped region to the west of the 2018 scar and the low-elevation part inside the 2019 scar in Figures 3-7, which clearly showed up in Figures 3-3a, d, and g; the corresponding seasonal subsidence is also observed in Figures 3-4, 3-5, 3-6.

Figures 3-7 shows that excess uplift takes place at the 2018 and 2019 scars in the year immediately following the fires and that “permanent” annual subsidence starts in the next year after the fire. Moreover, Figures 3-7b and c indicate that the amplitude of annual subsidence in the second year after the fire is even larger than the first year at the 2018 scar. On the other hand, the annual subsidence signal in the 2019 fire scar is spatially heterogeneous compared to the 2018 fire scar (Figure 3-7c). The heterogeneity of the annual thaw subsidence amplitude may be related to the distribution of massive ice and micro-topography, such as gullies on a slope. Also, the discontinuous phase changes in Figure 3-7c are most likely due to unwrapping errors.

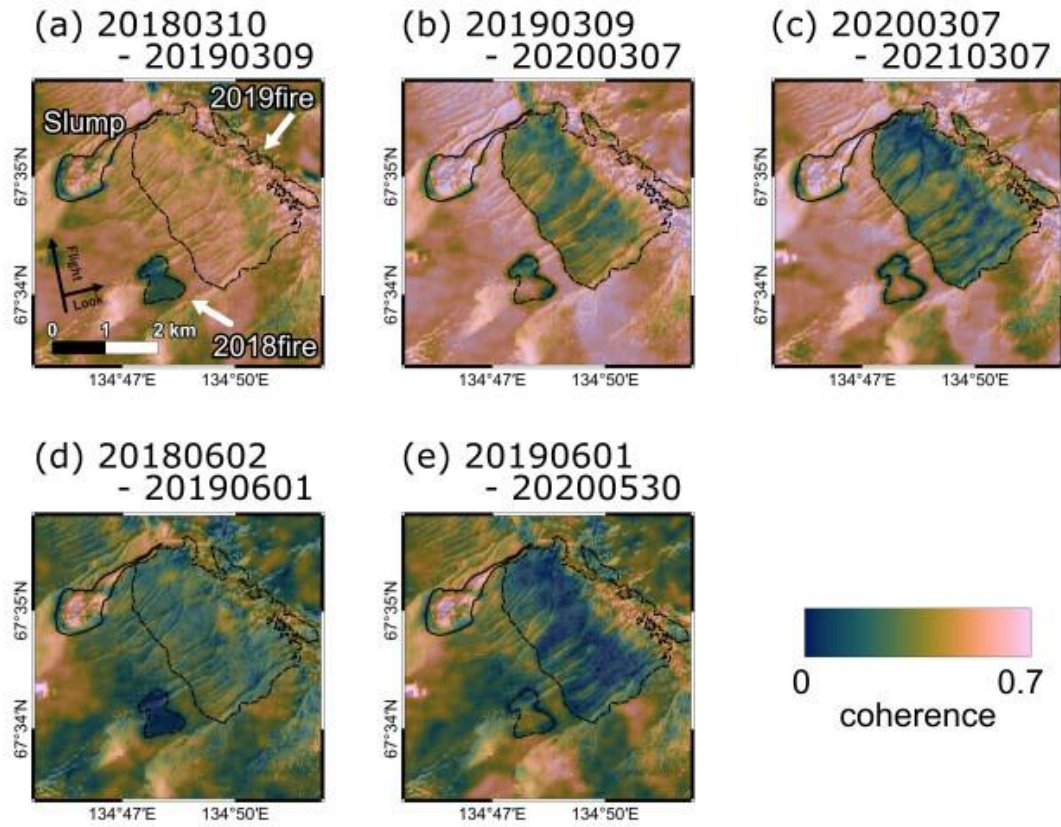


Figure 3-8. Coherence of one-year pairs of ALOS-2 interferograms (from yyyyymmdd to yyyyymmdd) before adaptive filtering. The upper row images are the coherence maps using March images. The lower row images are the interferogram using June and May images.

3.3.3 Temporal changes of thaw depth at the fire scars

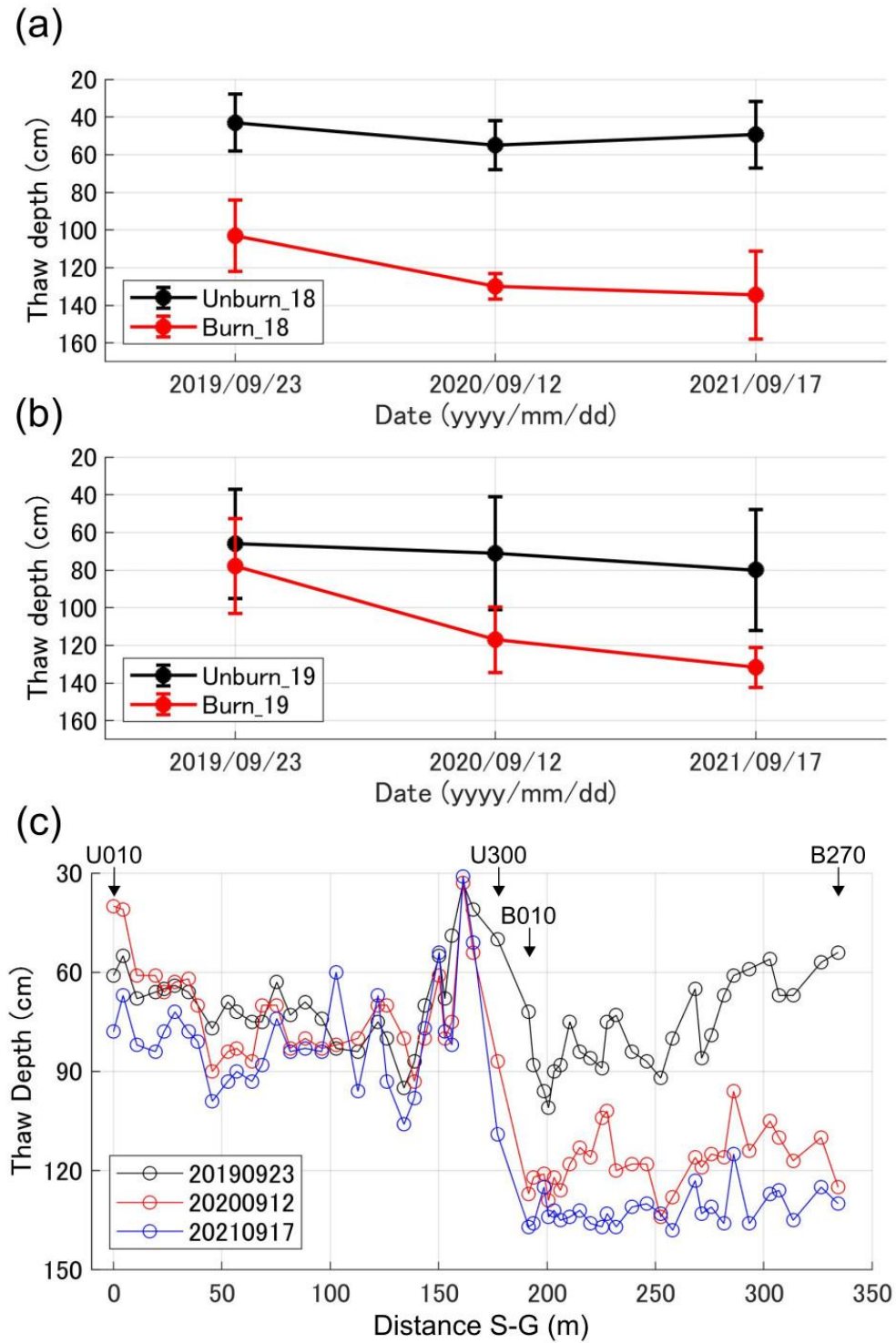


Figure 3-9. (a) Temporal changes of mean thaw depth at the 2018 scar. The black and red lines are mean values taken at unburned and burned sites, respectively. Error bars indicate the estimated standard deviation with 2σ . (b) Temporal change of mean thaw depth at the 2019 scar. (c) Temporal change of thaw depth before averaging at the transect S-G showed in Figure 3-2a. The unburned site is from point U010 to U300. The burned site is from point B010 to B270. The black, red, and blue lines indicate thaw depth at each measurement point in 2019, 2020, and 2021, respectively.

Figures 3-9 summarize the thaw depth measurements from 2019 to 2021, performed at both the 2018 and 2019 scars and the nearby unburned areas for comparison. In 2019, the mean thaw depth at the 2018 scar was about 103 ± 19 cm (Figure 3-9a), deeper by more than 60 cm than at the nearby unburned area. However, the mean thaw depths inside and outside the 2019 fire scar were 78 cm and 66 cm (Figure 3-9b), which are not significantly different. The thaw depth at the 2019 control site was originally about 20 cm deeper than at the 2018 control site, and there is no significant temporal change of depth at both control sites. Therefore, we can conclude that the thaw depths have deepened indeed by the wildfires in 2018 and 2019, whereas the deepening occurs not in the burned year but in the following years. It is notable that the thaw depth at the 2018 scar deepened further in 2020 than in 2019. Then, in 2021, the deepening rate decreased, reaching about 130 cm at the 2018 scar. The 2019 scar also reached about 130 cm thaw depth in 2021.

Figure 3-9c indicates the thaw depth values measured along the transect from point S to point G shown in Figure 3-2. The unburned area is from point U010 to point U300 with almost stable thaw depth values. Thaw depth deepened at point U300 since the point is located on a fire road with no surficial organic layer between unburned and burned sites. The burned area is from point B010 to point B270. The thaw depth increased at all measurement points in the first year more than in the

second year after the fires. In addition, some points reached about 130 cm depth in the first, and no deepenings were detected in the second year. It suggests that these points have high burn severity and post-fire thawing progressed rapidly.

3.4 Discussion

3.4.1 Reliability of heave signals in InSAR images

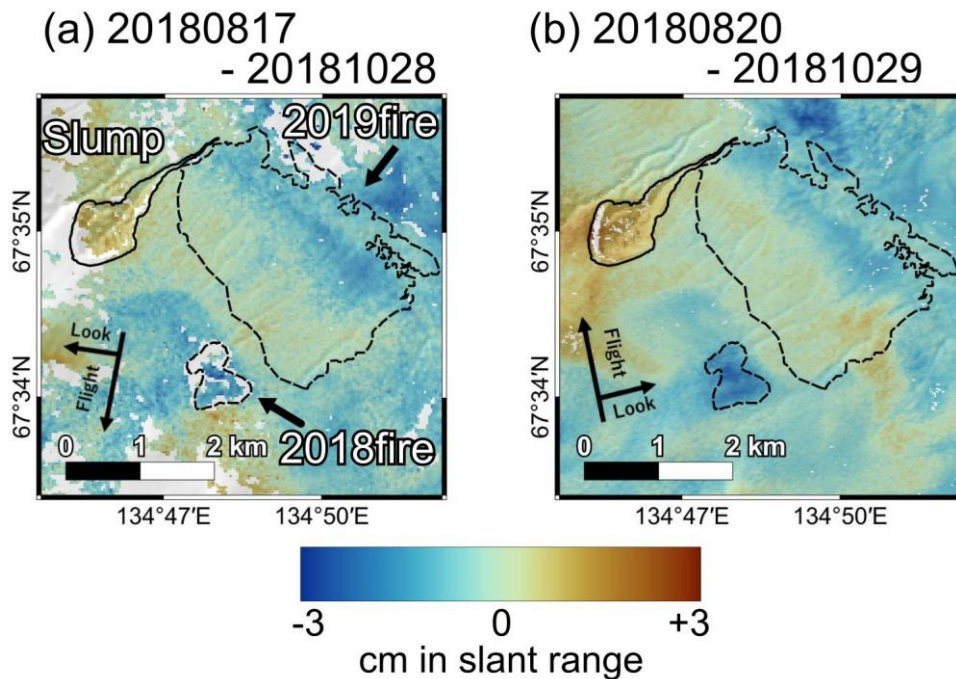


Figure 3-10. Comparison of LOS displacement value. (a) Sentinel-1 five interferograms stacked from 17th August to 28th October 2018. (b) ALOS2 interferogram from 20th August to 29th October 2018.

Figures 3-10 compares the LOS changes detected by Sentinel-1 (Figure 3-10a) with those by ALOS-2 (Figure 3-10b) during almost the same period from August to October 2018; they are derived from pre-snow- (pre-freezing) and post-snow-covered (post-freezing) images and the 2019 fire does not yet take place. Despite the different look directions and wavelengths of both sensors, at the 2018

and 2019 scars, the spatial distribution of the LOS changes in Sentinel-1 and ALOS-2 InSAR images are mostly consistent. It suggests that the LOS changes indicate almost entirely vertical ground surface deformation and are not significantly disturbed by imaging-date-dependent noise (e.g., tropospheric and ionospheric phase delay). Another reason of the consistency is that the gradient of the slope is gradual by 2~ 3 degrees. Therefore, we do not have to consider the sensitivity of the satellite look direction. If the slope is highly steep, the displacement in the normal direction will be significantly separated into vertical and horizontal components, and the amplitude distribution will change depending on the LOS direction.

The temporal change of the annual deformation in Figure 3-7 clearly indicates that they are due to frost heave instead of SWE. According to equation 6 in Guneriusen et al. (2001), an increase in SWE causes positive phase change. Since the long-wavelength trend is detrended, the signals at the fire scars represent a relative displacement to the unburned area. In other words, if the observed LOS changes were due to SWE, positive values in the fire scars indicate a relatively deeper snow cover than the unburned area, and negative values indicate a shallower snow cover. With the incidence angle of ALOS-2 (38 degrees), a linear approximation of equation 6 in Guneriusen et al. (2001) for snow density (ρ) in 0 - 0.5 can be expressed as;

$$\Delta\phi_S = -\frac{4\pi}{\lambda}\Delta Z_S(-1.00)\rho, \quad (3.1)$$

where ϕ_S is the phase delay due to snow cover, λ is the microwave wavelength (24.2 cm), and Z_S is the snow depth. Assuming a snow density of 0.2 g/cm³ from a representative value in Siberian taiga (Zhong et al., 2014), a displacement of 1.0 cm corresponds to a change in snow depth of 5.0 cm. In other words, if we consider Figure 3-7 in terms of change in snow depth, the relative snow depth must become shallow by ~5.0 cm only in the immediate fire year and deepen ~50 cm from the second year after the fire in the 2018 scar. However, such a reversed temporal change is unlikely. On the other hand, it is interesting to note that the LOS changes at the Batagaika megaslump are consistently

positive in both Sentinel-1 and ALOS-2. Considering the topographic depression there, they could possibly represent the SWE.

3.4.2 Comparison of seasonal freeze-thaw signals at certain unburned areas and fire scars

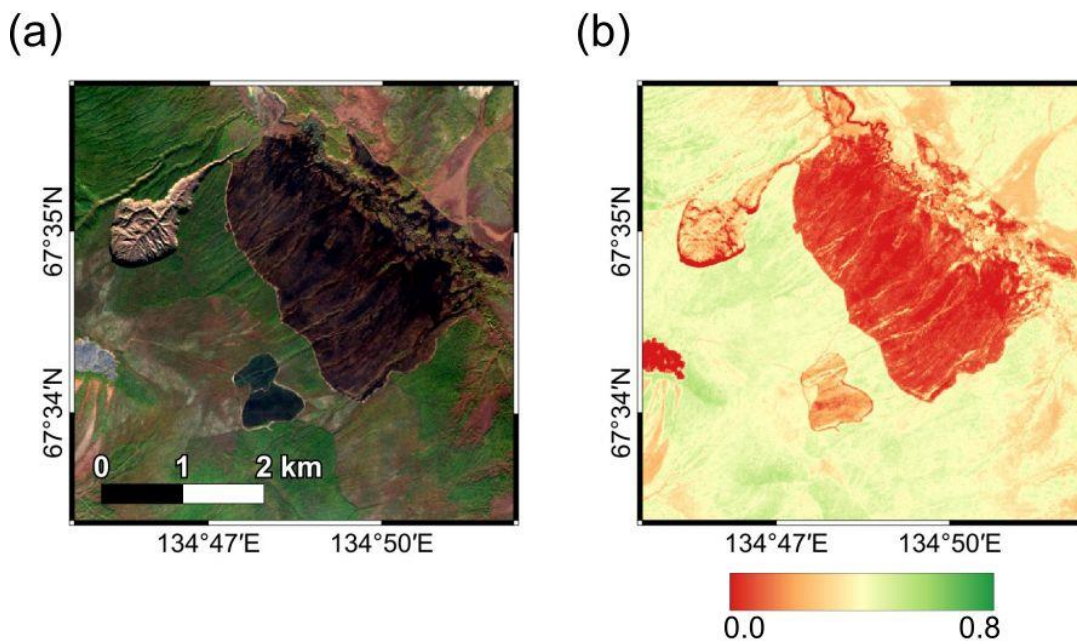


Figure 3-11. (a) Real color and (b) Normalized Difference Vegetation Index (NDVI) derived by Sentinel-2 image taken on 31 August 2019.

In addition to the large-amplitude frost heave over the fire scars, we have shown enhanced seasonal freeze-thaw signals at the diamond-shaped area near the 2018 scar and the north-eastern low-elevation area inside the 2019 scar. The duration of frost heave is apparently shorter than those observed at the fire scars (Figure 3-3). They are both unrelated to the wildfires (Figures 3-3a, d, g) but are commonly located in fewer tree areas (Figures 3-11a). On the other hand, NDVI shows no difference between the diamond-shaped area and surrounded tree area but

low values in the low-elevation area, suggesting that the soil can be exposed on the surface (Figure 3-8b). The relatively large seasonal heave signals suggest the deep ALT or high SWC, and more ice lenses formed. In addition, these two areas do not reveal clear annual subsidence signals (Figures 3-7). In other words, the spatio-temporal change suggests that differences in vegetation create an environment that is more prone to steady seasonal frost heave than the surrounding area, but permafrost disturbance and secular thawing are not occurring there.

3.4.3 Thaw depth evolutions and frost heave signals at the fire scars

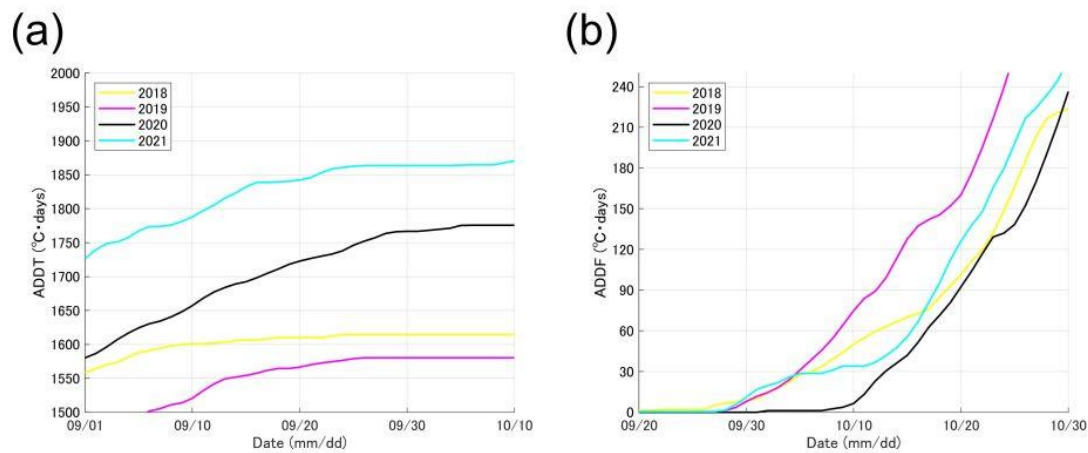


Figure 3-12. Temporal change of (a) ADDT and (b) ADDF at Batagay in September 2018-2021. The daily mean air temperature data at Batagay is archived on the CLIMAT website (<https://www.data.jma.go.jp/gmd/cpd/monitor/dailyview/index.php>) by the Japanese Meteorological Agency.

The extension of the frost heave period detected by InSAR described in Figure 3-3 is consistent with the temporal deepening of the thaw depth in Figure 3-9. The heave stopped in November in the burned year at both fire scars (Figures 3-3a and d), whereas it continued by December in the next year after the fires (Figures 3-3b and e). The thaw depth at the 2019 scar was not much

deep in 2019 (Figures 3-9b) because the 2019 scar did not experience an entire thawing season after burning in 2019. Furthermore, the increase in the heave period in the next year after the fires can be interpreted by the increase in time required for the freezing lines to descend to the subsurface layer. The temporal changes in thaw depth are consistent with those after fires in Alaska (Yoshikawa et al., 2003).

The thaw depths in 2020, however, may be under-estimated, which could be because the thaw season in 2020 was about ten days longer than 2019 and 2021. Figure 3-12 shows accumulated degree days of thawing (ADDT) and accumulated degree days of freezing (ADDF) at Batagay. Using Stefan function under the assumption of stable soil conditions during the period (e.g., Nelson et al., 1997; Klene and Hinkel, 2001), the thaw depth on 12 September was 4.0 cm shallower than that on 10 October, the last day of the thaw season. Thus, while it is certainly an under-estimate, the degree of under-estimation is less than the standard deviation. Furthermore, the long-lasting thaw season in 2020 is consistent with the temporal change of the frost heave. We can detect that the frost-heave initiated in mid-October and continued until December 2020 (Figure 3-6).

Although the thaw depth values are roughly the same at the 2019 scar as those at the nearby unburned area in 2019 (Figure 3-9b and c), Figure 3-7b clearly indicates excess frost heave signals at the 2019 scar in 2019. Roughly the same thaw depths at both burned and unburned areas suggest the same sub-surface temperatures and thus indistinguishable differences in the volume content of pore water as well. Then, the expanding volume of pore water by freezing would be identical at both burned and unburned areas, and no excess uplift at the burned could be expected. However, the loss of surface vegetation cover at the fire scar will generate a larger temperature gradient between the surface and the top of the ice-rich permafrost than at unburned area, thus causing a larger frost-heaving pressure that is proportional to the temperature gradient (e.g., Rempel et al. 2004; Worster and Wettlaufer, 2006).

Moreover, ADDE, which has monotonous progression throughout the winter, cannot explain stopping in early winter and the temporal extending of heave. In this respect, the temporal changes of heave signal in InSAR images are consistent with the report of the on-site heave experiment in Canada (Gruber, 2020). We consider these observations as a further evidence for the frost heave as due to ice lens formation by the migration of subsurface (premelted) water instead of due to the volume expansion of pore-fluids in the near-surface soil.

Chapter 4

Spatio-temporal Heterogeneity of Post-fire Permafrost Thaw within the 2018-19 Fire Scars

Chapter 4. Spatio-temporal Heterogeneity of Post-fire Permafrost Thaw within the 2018-19 Fire Scars

4.1 Introduction

Wildfire is one of the main factors of abrupt permafrost thaw that causes severe topography change (Holloway et al., 2020). In contrast to the gradual thaw due to temperature rising, the abrupt thaw happens locally but occurs deeper and more drastically (Turetsky et al., 2020). Indeed, the loss of surficial organic layer due to wildfires can accelerate the post-fire thawing of subsurface permafrost layer for years to decades (Yoshikawa et al., 2003; Holloway and Lewcowicz, 2019). Thus, as well as releasing greenhouse gases directly through the combustion of fire (Mack et al., 2014), post-fire thawing additionally promotes decomposition of soil organic carbon in the polar terrestrial region where half of the global belowground organic carbon is stored (Tarnocai et al., 2009). Furthermore, in the northern circumpolar region, a model estimation suggests global warming would increase the lightning flash rate, which is the major cause of wildfire (Chen et al., 2021). Thus, it can accelerate positive feedback on carbon release and resulting global warming. Therefore, it is necessary to elucidate the physical process of abrupt permafrost thaw and monitor thawing amounts more globally.

Abrupt thaw causes topography change such as land subsidence, thaw erosion on a slope, and landslide. This characteristic topography and deformation process are called “thermokarst” (Jorgenson and Osterkamp, 2005; Jorgenson, 2013; Kokelj and Jorgenson, 2013) and has been monitored by pioneering on-site observations and remote sensing techniques. The topography change can affect ecosystems and hydrological environments (Lawrence et al., 2015). For instance, some thermokarst lakes promote CH₄ emission from anaerobic environments in the bottom of those (Walter et al., 2008). Also, retrogressive thaw slumps (RTS) have discernable effects on lake-water chemistry by running off the sediment and melting water (Lantz and Kokelj, 2008). Interferometric Synthetic Aperture Radar (InSAR) has been used to detect such ground deformation in various permafrost

distributed areas (e.g., Liu et al., 2010; Short et al., 2011; Iwahana et al., 2016a; and Daout et al., 2017). In these previous studies, the effectiveness of L-band satellites has been reported because relatively long wavelengths can maintain high coherence even in the permafrost area. In the three Siberian cases, the effectiveness of L-band InSAR has also been reported. Yanagiya and Furuya (2020) detected post-fire thawing subsidence at the 2014 fire scar northwest to Batagay village in the Sakha Republic, Northeastern Siberia, with L-band and C-band InSAR (see Chapter 2). Abe et al. (2020) detected thermokarst subsidence at Maya, Sakha Republic, using L-band InSAR. Antonova et al. (2018) have successfully detected thermokarst signals around the Lana River delta using X-band InSAR, but they also mentioned the effectiveness of L-band InSAR.

Chapter 3 reported immediate post-fire ground deformation in the 2018-19 fire scars on the same slopes as the world's largest RTS, Batagaika megaslump. InSAR images maintained high coherence even in pairs during winter and across the fire season around Batagay. To further investigate the spatial pattern of post-fire thaw, especially within the fire scars, we started observations with ALOS-2 SM1 data with a high spatial resolution. The Batagaika megaslump has expanded from a small gully in the 1970s to a diameter of 1.8 km in 2019, and thawing is still in progress (Kunitsky et al., 2011; Murton et al., 2021). Assuming nearly the same amount of ground ice is distributed around the fire scars, a second megaslump could be formed due to post-fire permafrost thawing. Therefore, we need to observe the detailed topographic changes from the early disturbance stage. The primary objective of this chapter was to detect finer-scale ground deformation than our previous reports. As a result, we detected spatially heterogeneous deformation signals within the fire scars. The second objective was to interpret the spatial heterogeneity of the post-fire ground deformation with the on-site measured data of thaw depth, ground temperature, and soil water content (SWC). We especially found and discussed the spatial heterogeneity around the gully in the 2019 scar and inside the 2018 fire scar.

4.2 Data and Method

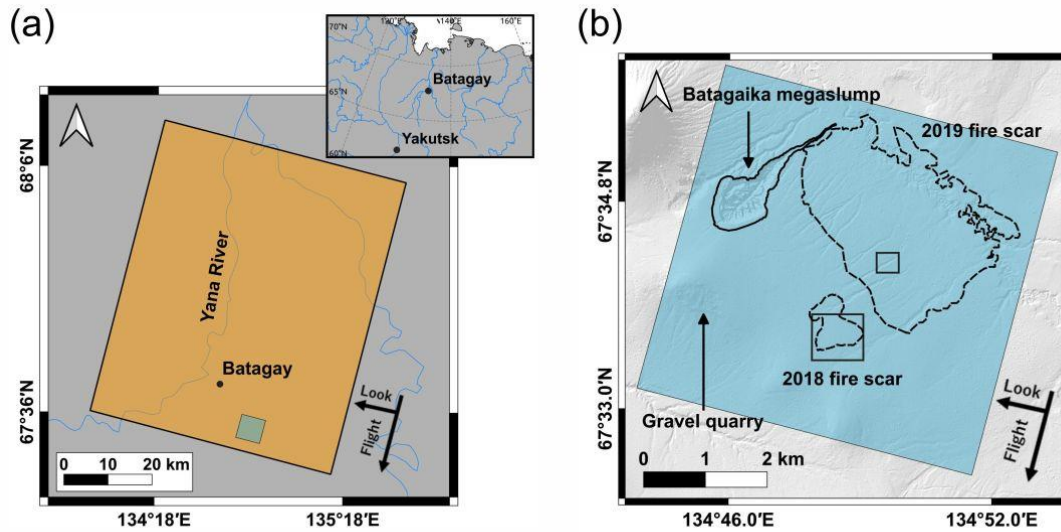


Figure 4-1. ALOS-2 imaging area around the 2018 and 2019 fire scars. (a) The orange rectangular indicates the imaging range of the original ALOS-2 SM1 InSAR image. (b) The blue rectangular indicates the range of the clipped InSAR image. The black dashed lines are the target fire scars, and the black line is Batagaika mega slump. The black rectangular indicate the closed-up area in figure 4-3 and 4-4.

The InSAR images were derived from the ALOS-2/PALSAR-2 SM1 mode image, which has a high spatial resolution of 1.4 m in the range direction and 1.8 m in the azimuth direction. The orange square in figure 4-1a shows the full scene imaging coverage, and the blue square in 4-1b shows the clipped coverage around the fire scars. In the clipped InSAR images, the number of looks for range and azimuth directions is 2×2 px (2.8×3.6 m). The topographic fringes were simulated using the 2 m mosaic data of ArcticDEM, which is provided by the University of Minnesota (Porter et al., 2018). In addition, the InSAR images were detrended after unwrapping using a quadratic polynomial approximation to simulate the long-wavelength phase trend. We discuss the relative displacement of the fire scars to the surrounded unburned sites because the displacement value is almost zero in the

unburned sites. We performed these InSAR image analyses with the GAMMA software in version 20200728 (Wegmüller and Werner, 1997).

Furthermore, we conducted on-site observation from 15 to 21 September 2021 within the fire scars, where the InSAR images detected particularly significant spatial heterogeneities. The location of each measurement point is shown in Figures 4-7 and 4-8. We set up a 350 m transect across the gully from northside to southside in the 2019 scar and measured thaw depth and SWC with about 5 m intervals. On the other hand, we set up an 800 m transect from the west part to the east part of the 2018 scar and measured the thaw depth and SWC every ten times at ten observation points. Thaw depth data were measured by probing with a metal rod, which has accuracy in centimeters. We manually measured the depth from the ground surface (below the surficial vegetation layer) to the frozen table. SWC data were collected by electric conductivity measuring with a soil moisture meter at the same point as thaw depth measurement. The length of the soil moisture meter is 20 cm, and we probed vertically from the ground surface. Thus, the values of SWC are averaged from the ground surface to a depth of 20 cm. We also excavated pits at representative points of the bottom, flank, and outside the gully in the 2019 scar. In the pits, we took vertical profiles of soil temperature and SWC every 10 cm interval.

4.3 Results

4.3.1 Spatially heterogeneous signals detected L-band InSAR

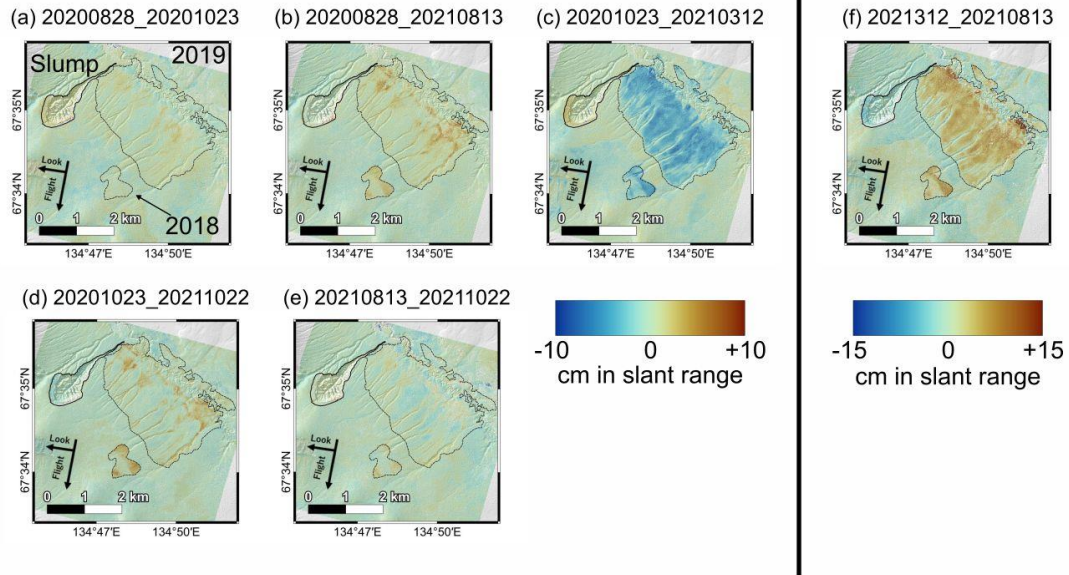


Figure 4-2. Overview of the ALOS-2 SM1 InSAR images with a shaded relief map around the fire scars. Warm and cold colors indicate LOS displacement far away and toward the satellite, respectively. (a, c, e, f) Seasonal deformation in each period (yyyymmdd to yyyymmdd). (b, d) Annual subsidence from 2020 to 2021 (yyyymmdd to yyyymmdd).

The ALOS-2 SM1 InSAR images showed spatial heterogeneity of the seasonal and annual ground displacement within the 2018-19 fire scars (Figure 4-2). Each InSAR image shows the ground deformation in the following periods; the transition period from the thaw season to the freezing season (Figures 4-2a and e), the annual period from 2020 to 2021 (Figures 4-2b and d), the freezing season in 2020 (Figure 4-2c), and the thaw season in 2021 (Figure 4-2f).

In the transition period, the thaw subsidence and frost heave signals could be canceling out (Figures 4-2a and e). Therefore, the displacement amplitude is as small as ~3 cm, and the positive and negative signals exist simultaneously within the fire scars. The annual displacement is far from the satellite, indicating the post-fire secular subsidence. The amplitude of annual subsidence was larger than that of the transition period (Figures 4-2b and d). Furthermore, the spatial pattern of annual subsidence is spatially ununiform. The annual subsidence signals were detected only around the gully, part of the lower portion in the 2019 scar, and only at the east and west parts in the 2018 scar. In these regions, positive signals are detected in the transitional period, and it indicates seasonal subsidence is also predominant there.

The seasonal ground deformation had a larger amplitude up to 15 cm than annual ground deformation. The displacement toward the satellite, indicating frost heave, was detected in the freezing season (Figure 4-2c), and the displacement far from the satellite was detected in the summer season (Figure 4-2f). The seasonal heave and subsidence showed different spatial patterns from the annual ground subsidence and almost uniformly deformed within the 2019 scar. In the 2019 scar, the seasonal ground deformation signals were detected in the plain slope area between gullies, where there is no deformation signal annually. There are also seasonal displacement signals with a small amplitude outside the fire scars. For instance, the diamond-shaped area west to the 2018 scar deformed only seasonally and has not deformed annually. It is the same temporal pattern as immediately after the fire, caused by vegetation distribution (see Chapter 3).

(a) 20201023_20211022 (b) 20201023_20210312 (c) 20200312_20210813

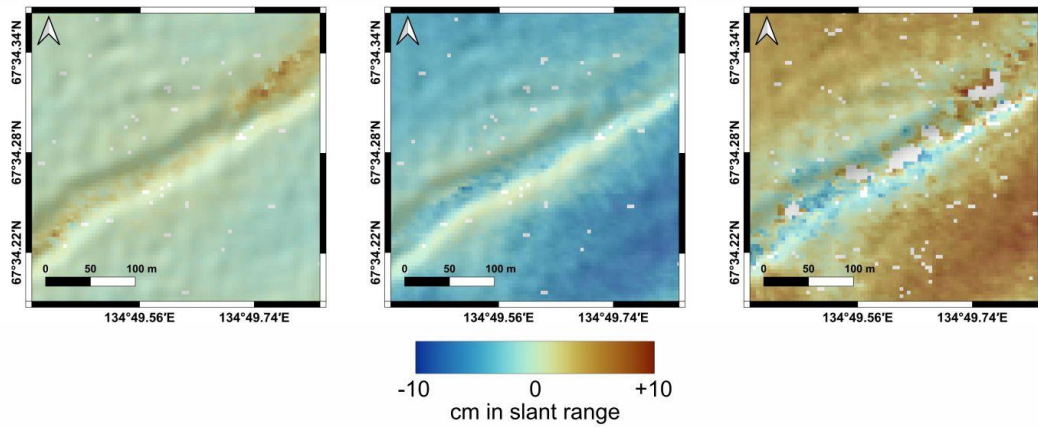


Figure 4-3. ALOS-2 SM1 InSAR images around the gully in the 2019 scar with a shaded relief map. (a) Annual subsidence from 23 October 2020 to 22 October 2021. (b) Seasonal uplift from 22 October to 12 March 2021. (c) Seasonal subsidence from 12 March to 13 August 2021.

The InSAR images indicated apparent spatial heterogeneity, particularly around the gully in the 2019 scar and the southern part of the 2018 scar. Figures 4-3 and 4-4 are enlarged InSAR images around there. The imaging ranges are indicated by the black square in Figure 4-1b. First, in the 2019 fire scar, the deformation signals were ununiform at the bottom, flank, and outside the gully. The InSAR images showed ~3 cm of annual subsidence (Figure 4-3a) and ~6 cm of seasonal heave (Figure 4-3b) at the bottom of the gully. However, the signal may be derived due to the effect of water and discussed the effect of phase noise with the Phase Closure Test (PCT) in Figure 4-9.

In the thaw season, some pixels lost coherence due to the effect of water flow at the bottom of the gully (Figure 4-3c). It suggests that the water flow changes the backscattering process between primary and secondary imagings. In the area along the flank of the gully, we can confirm no

displacement signal both annually and seasonally. On the northeast part of the south-facing flank of the gully, the InSAR image detected an annual subsidence signal (Figure 4-3a). We can see the decorrelation signal at the same area in the summer pair (Figure 4-3c), suggesting that erosion-like deformations might occur there. Moreover, the InSAR images detected ~10 cm of displacement in both seasonal heave and subsidence in the plane slope area, although almost no subsidence annually.

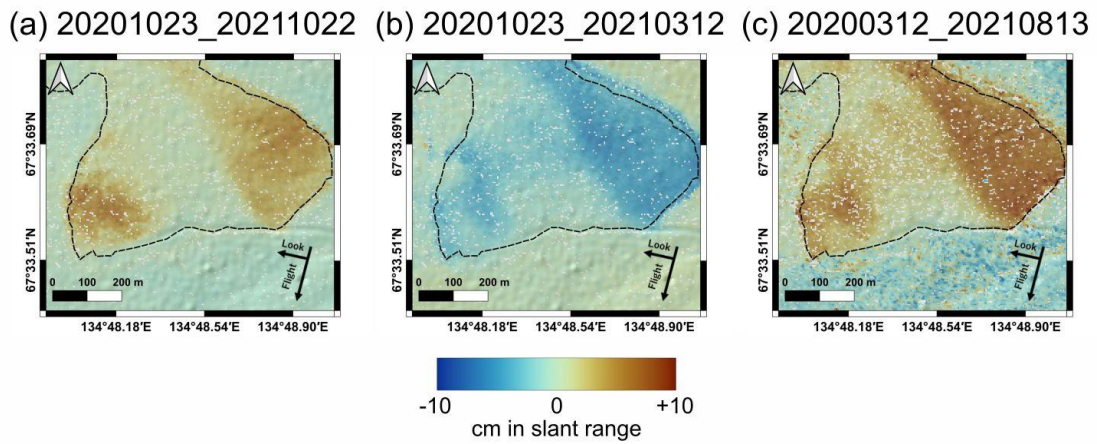


Figure 4-4. ALOS-2 SM1 InSAR images around the displacement boundary in the 2018 scar. (a) Annual subsidence; (b) Seasonal uplift; (c) Seasonal subsidence on the same time range as Figure 4-3.

In the second place, there is a clear boundary between the deformed and non-deformed areas within the 2018 scar. At the east and west parts of the 2018 scar, the InSAR images detected ground deformation signals both seasonally and annually (Figure 4-4). The amplitude of annual subsidence was ~8 cm, that of seasonal heave was ~6 cm, and that of seasonal subsidence was ~10 cm. On the other hand, at the central part of the 2018 scar, there is almost no deformation signal both seasonally and annually. The amplitude of annual subsidence was ~1 cm, that of seasonal heave was ~3 cm, and that of seasonal subsidence was ~4 cm. In contrast to the gully in the 2019 scar, the terrain in the 2018

scar is relatively uniform, and it was challenging to interpret the cause of these ununiform deformations only from the InSAR images.

4.3.2 SBAS time series analysis

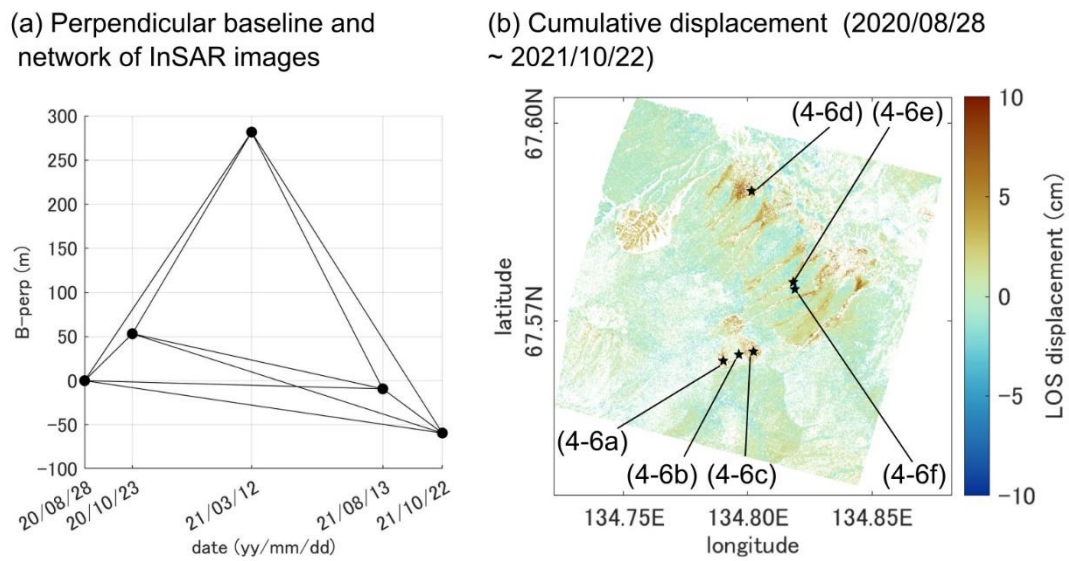


Figure 4-5. (a) The network of the InSAR images. The perpendicular baseline is the relative value to the first date SAR data. (b) Estimated cumulative displacement in LOS direction from 28 August 2020 to 22 October 2021. The black stars indicate the points of each time series panel shown in Figure 4-6.

We applied InSAR time series analysis named the small baseline subset (SBAS) method (Berardino et al., 2002; Schmidt and Bürgmann, 2003) using ten images of ALOS-2 SM1 InSAR. The perpendicular baselines (B-perp) of all InSAR images are less than 350 m because the orbit of ALOS-2 is well controlled. Therefore, we did not consider the coherence loss due to B-perp. The summer-winter pair showed coherence loss at the bottom of the gully but maintained in almost other areas. Hence, we derived all InSAR pairs for the analysis and calculated modeled LOS

displacement values of the four periods. Figure 4-5a shows the time intervals and B-perm of each InSAR image. Figure 4-5b is the cumulative value of the estimated ground deformation in the entire period. A cumulative positive value indicates the progress of the secular thaw subsidence interannually. The secular subsidence signal has the same spatial pattern as the original InSAR images. We also detected the phase changes at the interior of the slump and the bottom of the gully. The results of PCT suggest that these phase changes might be caused by unwrapping error and phase noise due to soil water (Figure 4-10).

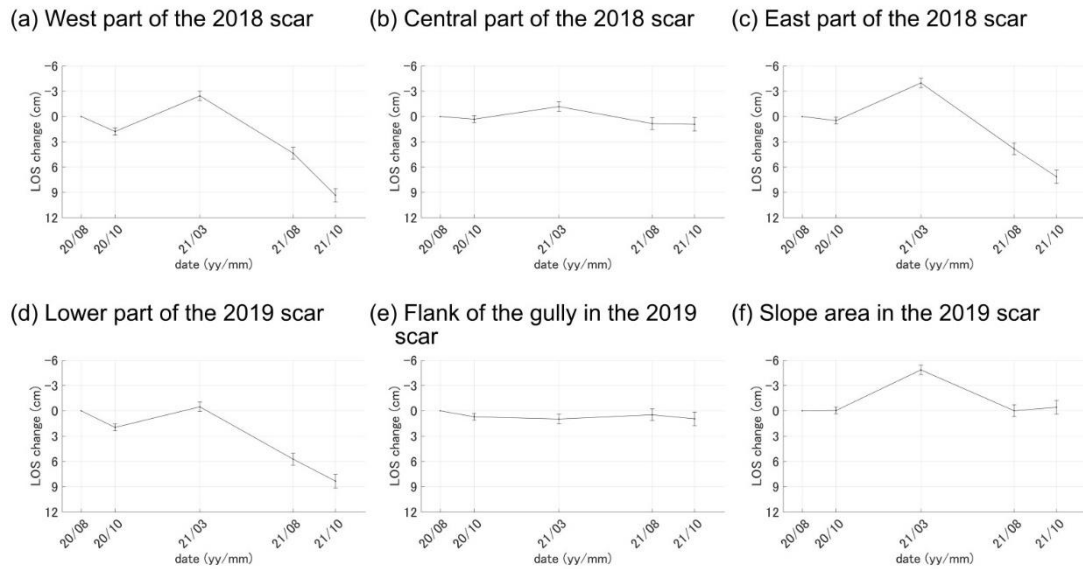


Figure 4-6. The time series of estimated LOS displacements at each point indicated in Figure 4-5. Negative and positive values mean uplift and subsidence signals. Panels (a), (b), and (c) are at the west, central, and east parts of the 2018 scar, respectively. Panel (d) is at the lower portion of the 2019 scar. Panels (e) and (f) are at the flank of the gully and the slope area in the 2019 scar, respectively.

The estimated LOS change time series at the six representative points indicated the temporal deformation process (Figure 4-6). The error bars indicate the propagated model errors as a value of 2σ assuming that the standard deviation of each InSAR image is 0.2 cm. Since the long-wavelength trend was removed from all the InSAR images, we considered the noise amplitude was smaller than the previous study (e.g., 0.4 cm in Schmidt and Bürgmann, 2003). The temporal patterns at each point are ununiform. For example, the east and west parts of the 2018 scar deformed seasonally and annually (Figure 4-5a and c). On the other hand, in the central part, the amplitude of seasonal deformation is reduced to about 1 cm, and slight annual subsidence occurs. In the 2019 scar, significant seasonal deformation and secular subsidence were detected in the lower part of the slope near the river (Figure 4-5d). There is no deformation signal on the flank of the gully (Figure 4-5e). On the flat slope outside the gully, although seasonal deformation occurred with the same amplitude as in other areas, no annual deformation occurred (Figure 4-5f). Thus, we found several temporal patterns of the post-fire deformation process within the fire scars.

4.3.3 Thaw depth and soil water content measurement

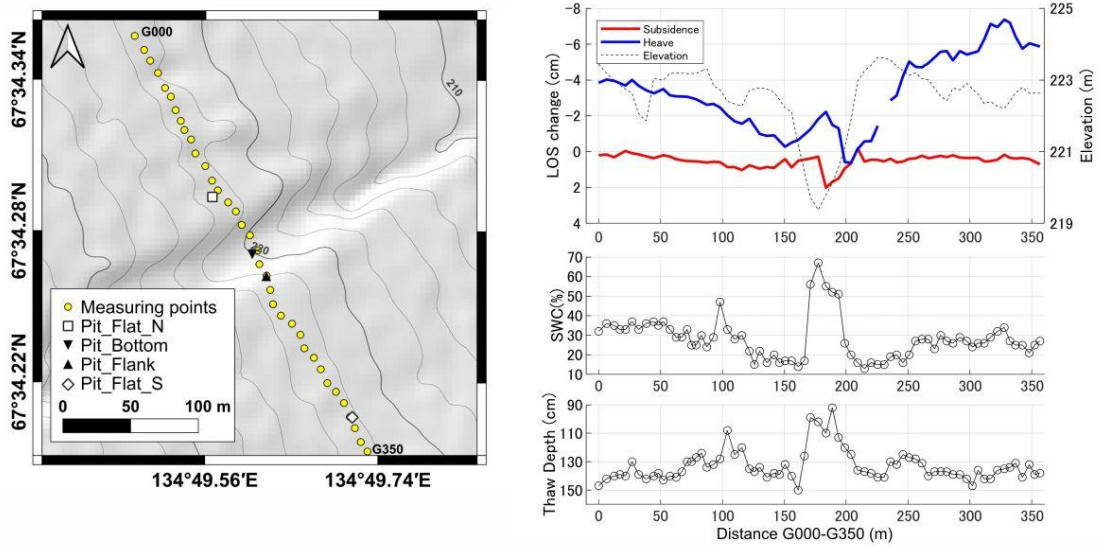


Figure 4-7. The left panel is the map of on-site observation in 2021. The right panels show the profiles of LOS change, SWC, and thaw depth across the transect from G000 to G350 shown in the left panel.

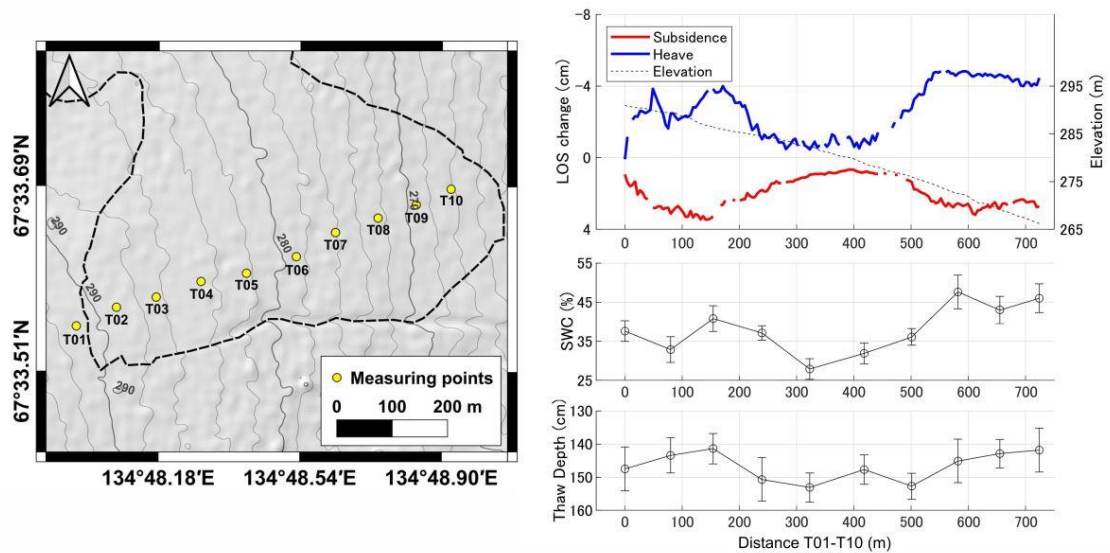


Figure 4-8. The left panel is the map of on-site observation in 2021. The right panels show the profiles of LOS change, SWC, and thaw depth across the transect from T01 to T10 shown in the left panel.

Figure 4-7 shows the on-site observation points around the gully in the 2019 scar as yellow points. The black dashed line indicates DEM elevation in the upper right panel, the red line indicates annual subsidence (Figure 4-3a), and the blue line indicates seasonal heave (Figure 4-3b). The middle right panel indicates SWC measured along the transect from point G000 to G350 across the gully in the 2019 scar. The lower right panel indicates thaw depth values along the same transect. The bottom of the gully shows a specific high SWC and shallow thaw depth due to the water flow and erosion. Comparing the flanks with the flat slope outside the gully, we detected no significant difference in the thaw depth, but the SWC was ~10% lower on the flanks than the flat slope. This trend was also shown in the pits described below, indicating a drier soil condition at the gully's flanks.

Figure 4-8 shows the on-site observation points inside the 2018 scar as yellow points. The black dashed, blue, and red lines on the upper right side indicate DEM elevation, seasonal heave (Figure 4-4b), and annual subsidence (Figure 4-4a), respectively. The middle right panel shows SWC, and the lower right panel shows thaw depth. The values are averages of ten measurements at each point, and the error bars represent 2σ of the measured values. The distribution of SWC shows that the east-west well-deformed parts had ~ 20% higher value than the non-deformed central part. On the other hand, there is no significant difference in thaw depth between the east-west and central parts. Moreover, the thaw depth in the east-west part is slightly shallower than that in the central part (~10 cm). Therefore, it indicates no positive correlation between seasonal deformation and the thaw depth as described in previous studies. Instead, it suggests that seasonal deformation increased due to extra ice lenses with high soil water content.

4.3.4 Pit survey around the gully in the 2019 fire scar

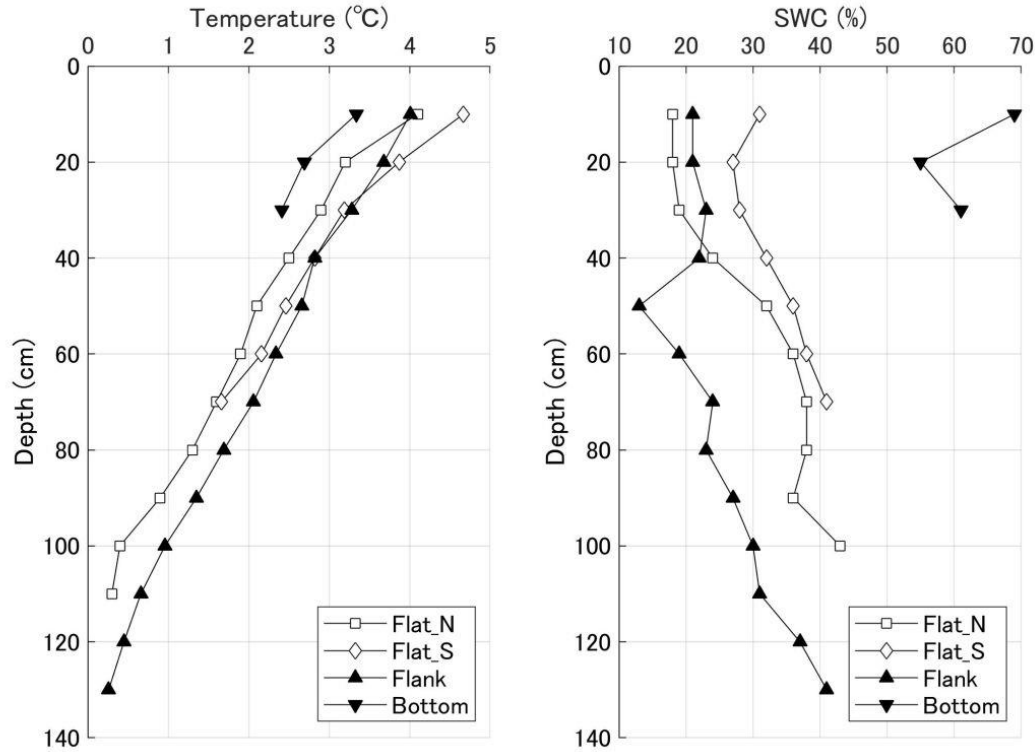


Figure 4-9. The vertical profile of soil temperature and SWC at the pits along the transect of the gully.

Figure 4-9 shows the vertical profile of ground temperature and SWC at the four pits shown in the left panel of Figure 4-7. The white square indicates the north flat area, the white diamond indicates the south flat area, the black triangle indicates the flank of the gully, and the black reversed triangle indicates the bottom of the gully. Photographs of each pit are shown in Appendix (Figure 8-1). Other than the gully flanks, the three points were saturated with groundwater during excavation and could not reach the permafrost layer. On the other hand, the permafrost layer was exposed at the flank at a depth of 140 cm. The permafrost layer is composed of mineral soil, and no ground ice was

exposed. Similar to the trend of Figure 4-7, the bottom of the gully shows higher soil temperature and soil moisture content. On the other hand, the profile indicates that the soil temperature and SWC at the flank were at ~ 0.5 °C and $\sim 20\%$ lower than those in the plane slope area, respectively. The trend became stronger as the depth got deepening.

4.4 Discussion

4.4.1 Spatial heterogeneity around the gully in the 2019 fire scar

The annual subsidence around the gully was limited only to the bottom and part of the flank and not detected in the plane slope area between gullies (Figure 4-6f). This process is as opposed to the cases of the 2014 scar (Yanagiya and Furuya, 2020) and the 2018 scar. The amplitudes of annual subsidence were large in the year close to the burning in the two cases. Hence, it can suggest that fire-induced secular thawing in the plane slope area within the 2019 scar has calmed down only in a year. The amplitude of the seasonal deformation is ~ 10 cm larger than that of the surrounding unburned area. It can be interpreted as the ALT reaching a maximum of 150 cm (Figure 4-7) and sufficient soil water for ice lens formation.

On the other hand, neither annual nor seasonal deformations had occurred in the gully flank (Figure 4-6e). The result suggests that there was no melting of ground ice and also no seasonal ice lens formation. The on-site observation in 2021 revealed that thaw depth deepened on the flank to the same depth as the plane slope areas. In addition, the on-site data showed that the soil water content was $\sim 20\%$ lower than the slope area, both horizontally and vertically. It suggests soil water content was insufficient for ice lens formation due to the gully's topography. Moreover, it also means that seasonal deformation cannot be interpreted in terms of thaw depth.

Annual subsidence and seasonal heave signal in winter were detected at the bottom of the gully, while the result was noisy in the summer-winter pair due to coherence loss. Although the coherence was relatively high for the annual and winter pairs, we performed a phase closure test to investigate phase noise due to water flow at the bottom of the gully. The phase closure (Φ) is expressed as follows (De Zan et al., 2015);

$$\Phi_{abc} = \phi_{ab} + \phi_{bc} + \phi_{ca}, \quad (4.1)$$

where ϕ_{ab} means interferometric phase between the date a and b. The phase closure test is mainly used to check a noise due to soil moisture (Zwieback et al., 2016). This principle has also been used to detect unwrapping errors in automatic SBAS analysis programs (Morishita et al., 2020). Phase Closure would be zero under ideal conditions with no phase noise other than ground deformation. On the other hand, in case of unwrapping errors, the phase would be shifted by multiple of π in the phase closure.

We subtracted the long-wavelength trend from the original InSAR images, so the trend approximation model's effect can also be seen in the phase closure. Figure 4-10 shows the phase closure calculated for all the InSAR image combinations used in the SBAS analysis. The multiple values of π , which means unwrapping error, were detected inside the slump and around the northwest river (Figure 4-10e, h, j). Figure 4-10a, g, d, using the SLC image taken on 28 August 2020 and 12 March 2021, shows the signal along the gully inside the 2019 scar. It is caused by coherence loss in the original summer-winter InSAR image pair. It is worth noting that the signal was detected inside the gully in Figure 4-10c, f, h. For instance, Figure 4-10f shows the amplitude of phase closure at the gully bottom is ~ 4.0 radian, and that at the plane slope areas is ~ 0.3 radian. Although the coherence was relatively high because only annual and winter pairs were used, there is a large difference in phase closure values between the gully's bottom and plane slope areas. It suggests that we may be detecting

a water-affected phase noise at the gully's bottom even in the relatively coherent annual and winter pairs.

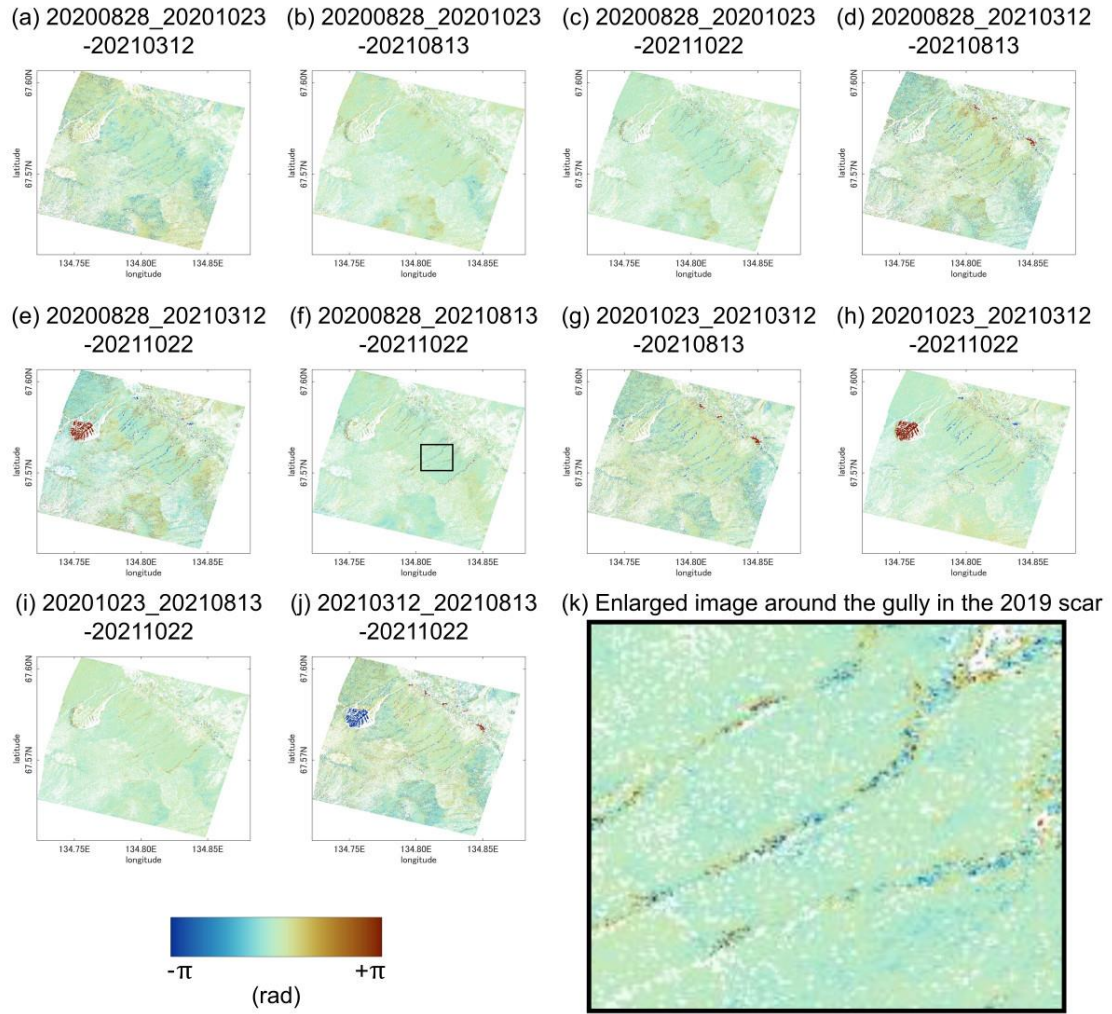


Figure 4-10. Phase closures for all combinations of the InSAR image. Each figure (a-j) shows the value between dates expressed as yyymmdd. The value of zero indicates that there is no phase change other than ground deformation. (k) Enlarged image of Figure 4-10f around the gully in the 2019 scar.

4.4.2 Clear boundary of subsidence and heave in the 2018 fire scar

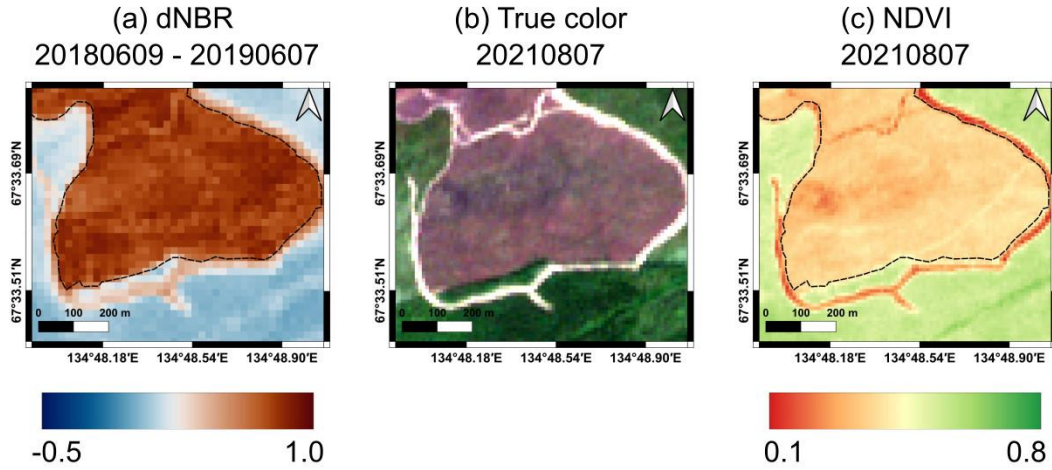


Figure 4-11. (a) dNBR value between 9 June 2018 (pre-fire) and 7 June 2019 (post-fire).

A positive value means the severity of the fire. (b) True-color image of Sentinel-2 taken on 7 August 2021. (c) NDVI on 7th August 2021 derived by Sentinel-2.

The InSAR images showed a clear boundary between the deformation and non-deformation areas within the 2018 scar. In addition, the on-site data showed a similar spatial pattern of SWC under the uniform condition of thaw depth. This chapter discusses the cause of heterogeneity of deformation and SWC based on vegetation and topography. Figure 4-11a shows the delta normalized burn ratio (dNBR) calculated by pre- and post-fire Sentinel-2 optical images. The positive value means severe burning. The value of dNBR is uniform inside the 2018 scar, indicating almost no spatial heterogeneity in burn severity. Figure 4-11b is the true-color image, and Figure 4-11c shows the normalized difference vegetation index (NDVI) on 7 August 2021 derived by Sentinel-2. NDVI was calculated from Band B8 (NIR) and B4 (Red) from Sentinel-2 optical image. A negative value indicates an unvegetated area, and a positive value indicates a vegetated area. On the surrounding 2018 scar, a negative value was detected linearly. It is the unpaved road local people made to pretend the fire extension. There is also a fire road within the 2018 scar, but it is not concerned with the spatial pattern

of the deformation signal. The vegetation is uniformly distributed in the 2018 scar. Therefore, it is impossible to interpret a clear boundary of the deformation area within the 2018 scar.

On the other hand, we used DEM to verify the correspondence between the boundary and the elevation. Figure 4-12a shows no clear correlation between the elevation itself and the boundary. In order to investigate the undulation in slope, we approximated the slope where the fire scar is located using the least-squares method (Figure 4-12b) and then subtracted the approximated plane from the original terrain (Figure 4-12c). Positive values indicate that the DEM is more convex than the approximated plane, while negative values indicate concave. Compared to the InSAR image, concavity was detected in the well-deformed area, and convexity was detected in the non-deformed area. In particular, the west well-deformed area corresponds well with the spatial change of undulation. A case of larch yellowing caused by ununiform soil water distribution due to undulations has been reported in Yakutsk (Iwasaki et al., 2010). Therefore, the undulation can contribute to the soil water distribution within the 2018 fire scar leading to an increase in the amplitude of seasonal ground deformation.

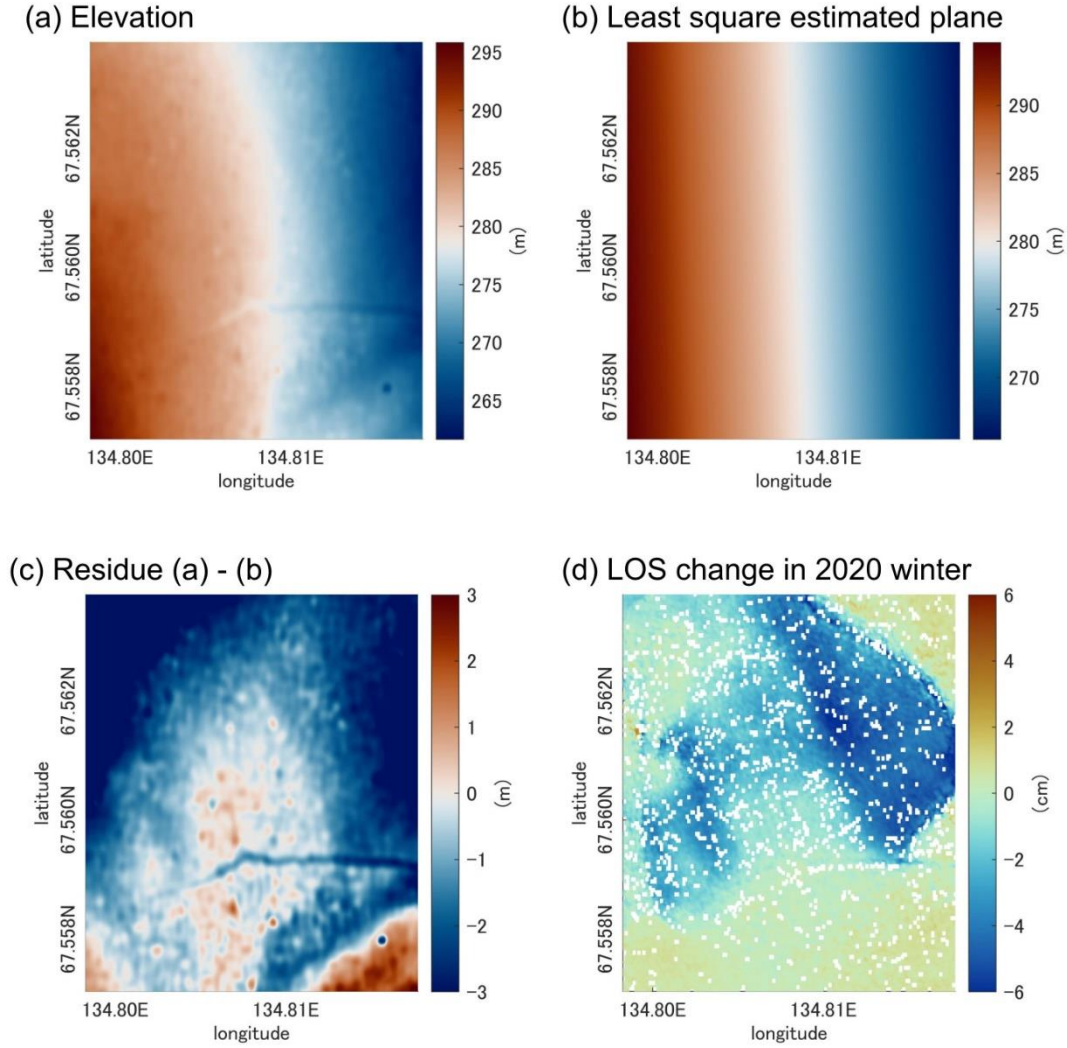


Figure 4-12. (a) Elevation value of ArcticDEM. (b) The plane approximated (a) with a least-squares method. (c) The residue was subtracted approximated plane from DEM. The positive and negative values mean that it is more convex and concave than the approximated plane, respectively. (d) LOS change in 2020 winter showed in Figure 4-4b.

As for the annual subsidence, spatial heterogeneity can be caused by topographic undulations. The ground ice melted in the well-deformed areas, while there may be no ground ice or the thaw depth may not have reached the ground ice layer due to convexity in the non-deformed area.

It suggests that topographic undulations also contribute to annual deformation. Shikolomanov et al. (2013) reported isotropic thaw subsidence in the undisturbed tundra region of Alaska. Isotropic means the annual and interannual thaw subsidence with constant ALT. They explained that there were spatial differences in the ice content of the transient layer just below the active layer, and only subsidence occurred due to meltwater runoff. Under a similar situation, annual subsidence may proceed selectively with constant ALT at both east and west well-deformed areas. In other words, the results suggest that post-fire annual subsidence can amplify the topographic undulations within the 2018 fire scar.

Chapter 5

Thesis Findings and Conclusions

Chapter 5. Thesis Findings and Conclusions

Although Siberia is the world's largest permafrost distribution area, the overall view of thaw amounts has not been studied sufficiently. Therefore, it causes uncertainty of the carbon cycle in the polar terrestrial region. Moreover, permafrost thawing has a complexity interrelating not only carbon emission but also geomorphology, hydrology, ecology, and local people's lives. This thesis reports the regional dynamics of post-fire abrupt thawing in Siberia for the first time by combining on-site observation and satellite geodetical observation. In particular, the thesis provides valuable data around Batagay, which has the potential for a drastic change of topography, such as the Batagaika megaslump.

Chapter 2 reports the spatio-temporal ground deformation at the 2014 fire scar detected by InSAR time-series analysis, the first challenge in Siberia. Time series analysis allowed us to estimate cumulative displacements and their temporal evolution, as quality interferograms could be obtained even in winter. The interannual permafrost thaw in the burned area lasted three years after the fire but apparently slowed down after five years. Despite the rather homogeneous burn severity, the cumulative subsidence magnitude was larger on the east-facing slopes and showed a clear correlation with the development of gullies, suggesting that the east-facing active layers might have been originally thinner. The interpretation of the frost heave signals within a framework of premelting dynamics is consistent with the seasonal heave amount derived by InSAR.

Chapter 3 focuses on the deformation immediately after the fires, which was not observed in Chapter 2 and other previous studies. Owing to the highly continental environment of Batagay and the high coherence of the L-band InSAR image, we succeeded in detecting the annual deformation across the fire period for the first time. As a result, we found that outstanding frost heave signal in the burning years, and the secular subsidence started in the next year of the fires. In addition, C-band InSAR captured the extension of the seasonal heave period corresponding to the time elapsed since the fires, and it corresponded to an increase in the thaw depth over time. However, these temporal

changes in frost heave cannot be interpreted by monotonic propagation in ADDF, suggesting the need for an interpretation based on premelting theory as well.

Chapter 4 discusses the causes of the spatial heterogeneity of deformation signals within the fire scars detected by high-resolution L-band InSAR images. We found the spatial pattern in seasonal and annual ground deformation closely correlated with gully topography in the 2019 fire scar. In addition, we also found a clear boundary of deformation area in the 2018 fire scar, where almost uniform vegetation, burn severity, and elevation. The on-site observation data indicate that the spatial heterogeneity of ground deformation within the fire scars correlates with the surface SWC instead of thaw depth. This result is contrary to the conventional reports of a positive correlation between the amount of post-fire seasonal deformation and thaw depth deepening. However, following the premelting theory, it can be qualitatively interpreted as an increase in ice lens formation due to increased soil water content. The gully topography determines the SWC distribution in the 2019 scar, and slight slope undulations would cause that in the 2018 scar. In other words, it is suggested that SWC distribution due to topography mainly dominates the amount of seasonal ground deformation in the interior of fire scars with sufficiently deepened thaw depth.

Overall, in the fire scars around Batagay, we observed accelerated interannual thaw subsidence and calming down over time, which had been previously reported in other regions. On the other hand, due to the snow cover characteristics that can maintain high coherence, we observed annual deformation in the burned year for the first time. The combination of on-site observation and InSAR image allows us to detect non-uniform deformation within the fire scars. It suggests that a simple algorithm for estimating a thaw depth from a seasonal subsidence value (e.g., ReSALT algorithm in Michaelides et al., 2019) would be inappropriate for post-fire thawing. This is because seasonal subsidence must be concerned with the melting of seasonally formed ice lenses, and the amount of ice

lens formation is not determined only by the thaw depth. Micro-scale premelting dynamics can describe the formation of ice lenses, but modeling macroscopic (meter to kilometer) deformation is a challenging theme. This thesis also confirms the effectiveness of L-band InSAR in permafrost observations as well as other previous studies. Currently, only JAXA's ALOS-2 is in constant operation, but its successor ALOS-4 and NASA/ISRO's NISAR will be launched in the next few years. More frequent observations by next-generation L-band satellites will spatially expand understanding of the dynamics of permafrost thawing in the whole polar region.

Chapter 6. Acknowledgment

First of all, I would like to thank Hokkaido University for providing an excellent research environment for me as a graduate student. Furthermore, I have deep respect and special gratitude for my supervisor, Professor Masato Furuya. Thanks to him, I got a chance to study the exciting cryosphere phenomenon of permafrost and learn about interferometric SAR from basic theory. I will never forget the first time we walked 15 km one way together in 2019 to observe the Batagay fire scar and camped there under the Siberian cold night. He always supported me in attending scientific meetings and fieldwork in Siberia. I also appreciate financial support as a doctoral researcher in the last six months of my doctoral course. I am grateful to my associate referees for their reviews. Prof. Kousuke Heki and Prof. Youichiro Takada helped me with my research by giving me accurate suggestions and advice in the solids seminar and daily laboratory life. Prof. Mamoru Ishikawa gave me the opportunity to attend the Winter School at the University of Oslo, as I had just started my research in a master's course and did not have knowledge about permafrost. Prof. Shyunji Kanie gave me precise comments from an engineering point of view at the joint research meeting of the feasibility study, which enabled me to proceed with my research. I would also like to thank Prof. Kiyoshi Yomogida and Prof. Kazunori Yoshizawa for their comments from various viewpoints through the solid seminars.

Especially, I would like to express my gratitude to Prof. Go Iwahana for his great help through our joint research and field observations. He listened to my reckless wish to visit the Batagay and supervised me from preparing the field measurement plan to the actual survey. Furthermore, he sharply pointed out my optimistic ideas in the field, and I could carry out observations flexibly. I would also like to thank my co-researcher, Dr. Petr Danilov. He helped and guided us through our first survey in Batagay in 2019. Prof. Alexander Fedorov, Director of the Melnikov Permafrost Institute, permitted us to enter and annual observations in Siberia and generously supported us with observation tools. Erel Stroticov was indispensable in guiding us in Batagay, assisting with our research, and taking care of the dreaded bear. My contemporary, Nikolai Fedorov, helped me with the annual field research and is a good friend to talk about Russian topics and discuss our research. I am looking forward to seeing him again in Siberia. I would also like to thank the researchers at the Melnikov Permafrost Institute, Sasha, the driver at the Batagay, and all the people involved in the research.

Some great research groups have given me the opportunity to learn about permafrost. I would like to thank all the joint feasibility study project members. In particular, Prof. Go Iwahana, Dr. Takahiro Abe, and Dr. Takumi Kawamura allowed me to accompany them on their observation of Mayya in 2018, the first time to visit Siberia for me. I would also like to thank ISOP, a permafrost research group in Japan, and all the researchers affiliated with them. They graciously allowed me to participate in the meetings, and I learned a lot from the open and vigorous discussions.

My laboratory members were always there to help me. Dr. Yoko Tu kindly welcomed me in room 303, as I had just been assigned to the lab and didn't know my way around. Dr. Yuji Himematsu kindly taught me many things, from PC setup to InSAR image analysis. Dr. Hitoshi Matsuzawa took a lot of time with me during our daily research and always cheerfully took me out to eat, taking care of my shyness. Mr. Elran Sumanjaya and Mr. Naufal Setiawan from Indonesia were good English practice partners. Thank you for accompanying me in discussions about research and GAMMA software despite my poor English. All of my peers have greatly supported me in both research and life. Mr. Kotaro Tsukahara, as a resident of room 303, has been a great help in discussions about analysis. Mr. Shuntaro Hata gave me information on cryosphere science. I have good memories of the two weeks we spent together at the University of Oslo. Of course, I was also supported by all the younger students. I would like to thank Yuta Tokui, Toru Taira, and Shun Fukushima for inviting me to go on a parfait tour during my laboratory life.

My family has always been supporting me. I am grateful to my parents, who raised me in Sapporo and generously encouraged me through graduate school. When I said I wanted to go on to a doctoral course, they worried about my lack of financial stability. Even though they probably want me to find a job as soon as possible, in the end I am most grateful that they trusted my decision. I will continue my research as long as I can. Finally, I would like to thank my wife, who has always been my closest supporter since our high school age. I am sure that the way to home with her has supported my research life. Especially during the month when I went to Siberia during the COVID disaster, I caused her great anxiety. Although our fields are different, I will devote myself to working as hard as her.

I wish to thank several financial supports from the Overseas Fellowship Program, Arctic Challenge for Sustainability (ArCS) Project for attending RCOP 2019, the Overseas Fellowship Program, and the Arctic Challenge for Sustainability II (ArCSII) Project for the field observation in 2021, and Hokkaido University DX Doctoral Fellowship. ALOS-2/PALSAR-2 level 1.1 data in the thesis are sharing among the PALSAR Interferometry Consortium to Study out Evolving Land surface (PIXEL) and provided by JAXA under a cooperative research contract with the Earthquake Research Institute, University of Tokyo. The ownership of PALSAR-2 data belongs to JAXA. Sentinel-1 and -2 data are provided by the ESA via Copernicus Open Data Hub (<https://scihub.copernicus.eu/>). Tandem-X DEM data is provided by the German Space Agency. ArcticDEM data is provided by the University of Minnesota via Polar Geospatial Center (<https://www.pgc.umn.edu/data/arcticdem/>). The climate data of Verkhoyansk and Batagay are provided by JMA via CLIMAT (<https://www.data.jma.go.jp/gmd/cpd/monitor/dailyview/index.php>). All the InSAR images in the thesis were generated by commercial software GAMMA. Some of the figures were generated by commercial software MATLAB and open-source software QGIS.

Chapter 7. Bibliography

- Abe, T., & Furuya, M. (2015). Winter speed-up of quiescent surge-type glaciers in Yukon, Canada. *The Cryosphere*, 9, 1183–1190. doi:10.5194/tc-9-1183-2015
- Abe, T., Iwahana, G., Efremov, P.V., Desyatkin, A.R., Kawamura, T., Fedorov, A., Zhegusov, Y., Yanagiya, K., Tadono, T. (2020). Surface displacement revealed by L-band InSAR analysis in the Mayya area, Central Yakutia, underlain by continuous permafrost. *Earth, Planets and Space*, 72. doi:10.1186/s40623-020-01266-3
- Antonova, S., Sudhaus, H., Strozzi, T., Zwieback, S., Kääb, A., Heim, B., Langer, M., Bornemann, N., & Boike, J. (2018). Thaw Subsidence of a Yedoma Landscape in Northern Siberia, Measured In Situ and Estimated from TerraSAR-X Interferometry. *Remote Sensing*, 10(4):494, doi:10.3390/rs10040494.
- Ashastina, K. (2018). Palaeo-environments at the Batagay site in West Beringia during the late Quaternary. *Doctoral Dissertation, the Friedrich Schiller University Jena*
- Ballantyne, C. K., & Murton J. B. (2018). Periglacial geomorphology. *John, Wiley & Sons Ltd., New Jersey*. ISBN 9781405100069
- Berardino, P., Fornaro, G., Lanari, R., & Sansosti, E. (2002). A New Algorithm for Surface Deformation Monitoring Based on Small Baseline Differential SAR Interferograms, *IEEE Trans. Geosci. Remote Sens.*, 40(11), 2375—2383. doi:10.1109/TGRS.2002.803792
- Biggs, J., Wright, T., Lu, Z., & Parsons, B. (2007). Multi-interferogram method for measuring interseismic deformation: Denali Fault, Alaska. *Geophys. J. Int.*, 170(3), 1165–1179. doi:10.1111/j.1365-246X.2007.03415.x.
- Brown, J., Ferrians, O.J.J., Heginbottom, J.A. & Melnikov, E.S. (1997) International Permafrost Association circum-Arctic map of permafrost and ground ice conditions. scale 1:10,000,000, U.S. Geol. Surv., Washington, D.C.
- Bürgmann, R., Rosen, P. A., & Fielding, E. J. (2000). Synthetic aperture radar interferometry to measure Earth's surface topography and its deformation. *Annual Review of Earth and Planetary Sciences*, 28, 169–209. doi.org/10.1146/annurev.earth.28.1.169
- Burn, C. R., & Lewkowicz A. G. (1990). Retrogressive thaw slumps. *The Canadian Geographer*, 34, 273–276.
- Chen, J., Günther, F., Grosse, G., Liu, L., & Lin, H. (2018). Sentinel-1 InSAR Measurements of Elevation Changes over Yedoma Uplands on Sobo-Sise Island, Lena Delta. *Remote Sensing*, 10, 1152; doi:10.3390/rs10071152.
- Chen, J., Liu, L., Zhang, T., Cao, B., & Lin, H. (2018). Using Persistent Scatterer Interferometry to Map and Quantify Permafrost Thaw Subsidence: A Case Study of

-
- Eboling Mountain on the Qinghai - Tibet Plateau. *J. Geophys. Res., Earth Surf.*, 123(10), 2663-2676, doi:10.1029/2018JF004618.
- Chen, Y., Romps, D. M., Seeley, J. T., Veraverbeke, S., Riley, W. J., Mekonnen, Z. A., & Randerson, J. T. (2021). Future increases in Arctic lightning and fire risk for permafrost carbon. *Nature Climate Change*, 11(5), 404–410.
- Cherosov, M. M., Isaev, A.P., Mironova, S.I., Lytkina, L.P., Gavriilyeva, L.D., Sofronov, R.R., Arzhakova, A.P., Barashkova, N.V., Ivanov, I.A., Shurduk, I.F., Efimova, A.P., Karpov, N.S., Timofeyev, P.A., & Kuznetsova, L.V. (2010). Vegetation and human activity, in *The Far North Plant Biodiversity and Ecology of Yakutia*, edited by A. P. Isaev et al., 286 pp., Springer, New York.
- Costantini, M., (1998). A novel phase unwrapping method based on network programming. *IEEE Transactions on Geoscience and Remote Sensing*, 36, 813–821. doi:10.1109/36.673674
- Daout, S., Doin, M. P., Peltzer, G., Socquet, A., & Lasserre, C. (2017). Large - scale InSAR monitoring of permafrost freeze - thaw cycles on the Tibetan Plateau. *Geophys. Res. Lett.*, 44(2), 901-909, doi:10.1002/2016GL070781.
- Dash, J. G. (1989). Thermomolecular Pressure in Surface Melting: Motivation for Frost Heave, *Science*, 246, 1591-1593.
- Dash, J. G., Rempel, A. W., & Wettlaufer, J. S. (2006). The physics of premelted ice and its geophysical consequences, *Rev. Mod. Phys.*, 78, 695—741. doi:10.1103/RevModPhys.78.695.
- Davies, D.K., Ilavajhala, S., Wong, M.M., & Justice, C.O. (2009). Fire Information for Resource Management System: Archiving and Distributing MODIS Active Fire Data. *IEEE Transactions on Geosci. Remote Sens.* 47 (1):72-79. doi:10.1109/TGRS.2008.2002076.
- De Zan, F., Parizzi, A., Prats-Iraola, P., & Lopez-Dekker, P. (2014). A SAR interferometric model for soil moisture. *IEEE Trans. Geosci. Remote Sens.*, 52(1), 418–425. doi: 10.1109/TGRS.2013.2241069.
- De Zan, F., Zonno, M., & López-Dekker, P. (2015). Phase Inconsistencies and multiple Scattering in SAR Interferometry. *IEEE Trans. Geosci. Remote Sens.*, 53(12), 6608–6616.
- Escuin, S., Navarro, R., & Fernández, P., (2008). Fire severity assessment by using NBR (Normalized Burn Ratio) and NDVI (Normalized Difference Vegetation Index) derived from LANDSAT TM/ETM images. *International Journal of Remote Sensing*, 29, 1053–1073.. doi:10.1080/01431160701281072

- Fedorov, A.N., Vasilyev, N.F., Torgovkin, Y.I., Shestakova, A.A., Varlamov, S.P., Zheleznyak, M.N., Shepelev, V.V., Konstantinov, P.Y., Kalinicheva, S.S., Basharin, N.I., Makarov, V.S., Ugarov, I.S., Efremov, P.V., Argunov, R.N., Egorova, L.S., Samsonova, V.V., Shepelev, A.G., Vasiliev, A.I., Ivanova, R.N., Galanin, A.A., Lytkin, V.M., Kuzmin, G.P., Kunitsky, V.V. (2018) Permafrost-Landscape Map of the Republic of Sakha (Yakutia) on a Scale 1:1,500,000. *Geosciences*, 8, 465. doi.org/10.3390/geosciences8120465
- Fialko, Y., Simons, M., & Agnew, D. (2001). The complete (3-D) surface displacement field in the epicentral area of the 1999 MW7.1 Hector Mine Earthquake, California, from space geodetic observations. *Geophys. Res. Lett.*, 28, 3063–3066. doi:10.1029/2001gl013174
- Fox-Kemper, B., H.T. Hewitt, C. Xiao, G. Aðalgeirsdóttir, S.S. Drijfhout, T.L. Edwards, N.R. Golledge, M. Hemer, R.E. Kopp, G. Krinner, A. Mix, D. Notz, S. Nowicki, I.S. Nurhati, L. Ruiz, J.-B. Sallée, A.B.A. Slangen, & Y. Yu, (2021). Ocean, Cryosphere and Sea Level Change. In *Climate Change 2021: The Physical Science Basis. Contribution of Working Group I to the Sixth Assessment Report of the Intergovernmental Panel on Climate Change. Cambridge University Press*. In Press
- French, H. M. (2007). *The Periglacial Environment -3rd ed.*, John Wiley & Sons Ltd.
- Furuya, M., Suzuki, T., Maeda, J., & Heki, K. (2017). Midlatitude sporadic-E episodes viewed by L-band split-spectrum InSAR, *Earth Planets Space*, 69:175. doi:10.1186/s40623-017-0764-6.
- Gibson, C. M., Chasmer, L. E., Thompson, D. K., Quinton, W. L., Flannigan, M. D., & Olefeldt, D. (2018). Wildfire as a major driver of recent permafrost thaw in boreal peatlands, *Nature Comm.*, 9:3041, doi:10.1038/s41467-018-05457-1.
- Gillett, N. P., Weaver, A. J., Zwiers, F. W., & Flannigan, M. D. (2004), Detecting the effect of climate change on Canadian forest fires, *Geophys. Res. Lett.*, 31, L18211, doi:10.1029/2004GL020876.
- Goldstein, R. M. (1995). Atmospheric limitations to repeat-track radar interferometry. *Geophys. Res. Lett.*, 22(18), 2517–2520. doi.org/10.1029/95gl02475
- Goldstein, R. M., & Werner, C. L. (1998). Radar interferogram filtering for geophysical application. *GEOPHYSICAL RESEARCH LETTERS*, 25(21), 4035–4038.
- Gomba, G., Parizzi, A., Zan, F. D., Eineder, M., & Bamler, R. (2016). Toward operational compensation of ionospheric effects in SAR interferograms: The split-spectrum method, *IEEE Trans. Geosci. Remote Sens.*, 54 (3), 1446–1461. doi:10.1109/TGRS.2015.2481079

-
- Gruber, S. (2020). Ground subsidence and heave over permafrost: hourly time series reveal interannual, seasonal and shorter-term movement caused by freezing, thawing and water movement. *The Cryosphere*, 14(4), 1437–1447.
- Guneriussen, T., Høgda, K. A., Johnsen, H., & Lauknes, I. (2001). InSAR for estimation of changes in snow water equivalent of dry snow. *IEEE Transactions on Geoscience and Remote Sensing*, 39(10), 2101–2108. doi.org/10.1109/36.957273
- Günther, F., Grosse, G., Jones, B. M., Schirrmeister, L., Romanovsky, V. E., & Kunitsky, V. (2016). Unprecedented permafrost thaw dynamics on a decadal time scale: Batagay mega thaw slump development, Yana Uplands, Yakutia, Russia, AGU Fall Meeting San Francisco, USA, 12 December 2016 - 16 December 2016.
- Harris, S.A., French, H. M., Heginbottom, J. A., Johnston, G. H., Ladanyi, B., Sego, D.C. & van Everdingen, R. O. (1988). Glossary of permafrost and related ground-ice terms, Technical Memorandum (National Research Council of Canada. Associate Committee on Geotechnical Research), doi.org/10.4224/20386561.
- Hinkel, K. M. & Nelson F. E. (2003). Spatial and temporal patterns of active layer thickness at Circumpolar Active Layer Monitoring (CALM) sites in northern Alaska, 1995–2000. *J. Geophys. Res.*, 108 (D2), 1995–2000. doi.org/10.1029/2001jd000927
- Hinkel, K. M. & Hurd, J. K. Jr. (2006). Permafrost Destabilization and Thermokarst Following Snow Fence Installation, Barrow, Alaska, U.S.A., *AAAR*, 38(4), 530-539.
- Holloway, J. E., & Lewkowicz, A. G. (2020). Half a century of discontinuous permafrost persistence and degradation in western Canada. *Permafrost and Periglacial Processes*, 31(1), 85–96. doi.org/10.1002/ppp.2017
- Hu, F. S., Higuera, P. E., Walsh, J. E., Chapman, W. L., Duffy, P. A., Brubaker, L. B., & Chipman, M. L. (2010). Tundra burning in Alaska: linkages to climatic change and sea ice retreat. *J. Geophys. Res. Biogeosci.* 115, G04002, doi:10.1029/2009JG001270.
- Hu, Y., Liu, L., Larson, K. M., Schaefer, K. M., Zhang, J., & Yao, Y. (2018). GPS Interferometric Reflectometry reveals cyclic elevation changes in thaw and freezing seasons in a permafrost area (Barrow, Alaska), *Geophys. Res. Lett.*, 45, 5581, doi: 10.1029/2018GL077960.
- Hugelius, G., Strauss, J., Zubrzycki, S., Harden, J. W., Schuur, E. A. G., Ping, C. L., Schirrmeister, L., Grosse, G., Michaelson, G. J., Koven, C. D., O'Donnell, J. A., Elberling, B., Mishra, U., Camill, P., Yu, Z., Palmtag, J. & Kuhry, P. (2014). Estimated stocks of circumpolar permafrost carbon with quantified uncertainty ranges and identified data gaps. *Biogeosciences*, 11 (23), 6573–6593. doi.org/10.5194/bg-11-6573-2014

- Ishikawa, M., & Saito, K. (2006). Frozen ground sciences influencing climate and water cycle-Reviews and perspectives. *J. Japan. Society of Snow and Ice* 68, 639–656. doi:10.5331/seppyo.68.639
- Iwahana, G., Uchida, M., Liu, L., Gong, W., Meyer, F. J., Guritz, R., Yamanokuchi, T., & Hinzman, L. (2016a). InSAR Detection and Field Evidence for Thermokarst after a Tundra Wildfire, Using ALOS-PALSAR, *Remote Sensing*, 8, 218, doi:10.3390/rs8030218.
- Iwahana, G., Harada, K., Uchida, M., Tsuyuzaki, S., Saito, K., Narita, K., Kushida, K., & Hinzman, L. D. (2016b). Geomorphological and geochemistry changes in permafrost after the 2002 tundra wildfire in Kougarak, Seward Peninsula, Alaska, *J. Geophys. Res., Earth Surf.*, 115(3), 1–14, doi.org/10.1002/2016JF003921
- Iwasaki, H., Saito, H., Kuwao, K., Maximov, T. C., & Hasegawa, S. (2010). Forest decline caused by high soil water conditions in a permafrost region. *Hydrol. Earth Syst. Sci. Discuss.* doi.org/10.5194/hessd-6-6087-2009
- Jafarov, E. E., Romanovsky, V. E., Genet, H., McGuire, A. D., & Marchenko, S. S. (2013). The effects of fire on the thermal stability of permafrost in lowland and upland black spruce forests of interior Alaska in a changing climate, *Environ. Res. Lett.*, 8, 035030, doi:10.1088/1748-9326/8/3/035030.
- Jolivet, R., Grandin, R., Lasserre, C., Doin, M.-P., Peltzer, G., (2011). Systematic InSAR tropospheric phase delay corrections from global meteorological reanalysis data. *Geophys. Res. Lett.* 38, doi:10.1029/2011gl048757
- Jones, B. M., Grosse, G., Arp, C. D., Miller, E., Liu, L., Hayes, D. J., & Larsen, C. F. (2015). Recent Arctic tundra fire initiates widespread thermokarst development, *Sci. Rep.* 5, 15865; doi: 10.1038/srep15865.
- Jorgenson, M. T., & Osterkamp, T. E. (2005). Response of boreal ecosystems to varying modes of permafrost degradation. *Canadian Journal of Forest Research*, 35(9), 2100–2111. doi.org/10.1139/x05-153
- Jorgenson, M. (2013). Thermokarst terrains, in Treatise on Geomorphology, vol. 8, edited by J. Shroder, R. Giardino, and J. Harbor, chap. Glacial and Periglacial Geomorphology, pp. 313–324, Academic Press, San Diego, Calif.
- Justice, C.O, L Giglio, S Korontzi, J Owens, J.T Morisette, D Roy, J Descloitres, S Alleaume, F Petitcolin, Y Kaufman (2002). The MODIS fire products. *Remote Sensing of Environment*, 83, 1-2, doi.org/10.1016/S0034-4257(02)00076-7
- Kanevskiy, M., Shur, Y., Fortier, D., Jorgenson, M.T. & Stephani, E. (2011). Cryostratigraphy of late Pleistocene syngenetic permafrost (yedoma) in northern

-
- Alaska, Itkilik River exposure. *Quaternary Research*, 75(3), 584-596, doi: 10.1016/j.yqres.2010.12.003.
- Kasischke, E., & Turetsky, M. (2006). Recent changes in the fire regime across the North American boreal region-spatial and temporal patterns of burning across Canada and Alaska, *Geophys. Res. Lett.*, 33, L09703, doi:10.1029/2006GL025677.
- Kasischke, E. S., Verbyla, D. L., Rupp, T. S., McGuire, A. D., Murphy, K. A., Jandt, R., Barnes, J. L., Hoy, E. E., Duffy, P. A., Calef, M. & Turetsky M. R. (2010). Alaska's changing fire regime — implications for the vulnerability of its boreal forests. *Canadian Journal of Forest Research*, 40(7), 1313–1324. doi.org/10.1139/x10-098
- Key, C. H., & Benson, N. C. (2006). Landscape Assessment (LA) sampling and analysis methods. *USDA Forest Service - General Technical Report RMRS-GTR, 164 RMRS-GTR*.
- Kinoshita, Y., Shimada, M., & Furuya, M. (2013). InSAR observation and numerical modeling of the water vapor signal during a heavy rain: A case study of the 2008 Seino event, central Japan, *Geophys. Res. Lett.*, 40, doi:10.1002/grl.50891.
- Klene, A. E., Nelson, F. E., Shiklomanov, N. I. & Hinkel, K. M. (2001). The N-Factor in Natural Landscapes: Variability of Air and Soil-Surface Temperatures, Kuparuk River Basin, Alaska, U.S.A. *Arctic, Antarctic, and Alpine Res.*, 33(2), 140. doi.org/10.2307/1552214
- Kokelj, S. V., & Jorgenson, M. T. (2013). Advances in Thermokarst Research, *Permafr. Periglac. Process.*, 24, 108–119, doi: 10.1002/ppp.1779.
- Kokelj, S. v., Tunnicliffe, J., Lacelle, D., Lantz, T. C., Chin, K. S., & Fraser, R. (2015). Increased precipitation drives mega slump development and destabilization of ice-rich permafrost terrain, northwestern Canada. *Global and Planetary Change*, 129, 56–68. doi.org/10.1016/j.gloplacha.2015.02.008
- Kunitsky, V. V., Syromyatnikov, I. I., Schirrmeister, L., Skachk-ov, Y. B., Grosse, G., Wetterich, S. & Grigoriev, M.N. (2013). Ice-rich permafrost and thermal denudation in the Batagay area - Yana Upland, East Siberia, *Kriosfera Zemli* (Earth' Cryosphere), 17(1), 56-68. (in Russian)
- Lacelle, D., Bjornson, J., & Lauriol, B. (2010). Climatic and Geomorphic Factors Affecting Contemporary (1950–2004) Activity of Retrogressive Thaw Slumps on the Aklavik Plateau, Richardson Mountains, NWT, Canada. *Permafr. Periglac. Process.*, 21, 1–15, doi: 10.1002/ppp.666.
- Lacelle, D., Brooker, A., Fraser, R. H., & Kokelj, S. V. (2015). Distribution and growth of thaw slumps in the Richardson Mountains–Peel Plateau region, northwestern Canada. *Geomorphology*, 235, 40-51, doi:10.1016/j.geomorph.2015.01.024

- Lantz, T. C., & Kokelj, S. V. (2008). Increasing rates of retrogressive thaw slump activity in the Mackenzie Delta region, N.W.T., Canada. *Geophysical Research Letters*, 35(6). doi.org/10.1029/2007gl032433
- Lawrence, D. M., Koven, C. D., Swenson, S. C., Riley, W. J., & Slater, A. G. (2015). Permafrost thaw and resulting soil moisture changes regulate projected high-latitude CO₂ and CH₄ emissions. *Environ. Res. Lett.*, 10 (9). doi.org/10.1088/1748-9326/10/9/094011
- Lewkowicz, A. G., & Harris, C. (2005). Morphology and geotechnique of active-layer detachment failures in discontinuous and continuous permafrost, northern Canada. *Geomorphology*, 69, 275-297, doi:10.1016/j.geomorph. 2005.01.01
- Lewkowicz, A. G. (2007). Dynamics of active- layer detachment failures, Fosheim Peninsula, Ellesmere Island, Nunavut, Canada. *Permafr. Periglac. Process.*, 18, 89–103, doi: 10.1002/ppp.578.
- Lewkowicz, A.G., & Way, R.G. (2019). Extremes of summer climate trigger thousands of thermokarst landslides in a High Arctic environment. *Nature Communications*, 10. doi:10.1038/s41467-019-09314-7
- Lillesand, T. M., Kiefer, R. W., & Chipmal, J. W., (2015). *Remote Sensing and Image Interpretation*, seventh edition. John Wiley & Sons, Inc., New York.
- Liu, L., Zhang, T., & Wahr, J. (2010). InSAR measurements of surface deformation over permafrost on the North Slope of Alaska. *J. Geophys. Res., Earth Surf.*, 115(3), 1–14, doi.org/10.1029/2009JF001547
- Liu, L., Jafarov, E. E., Schaefer, K. M., Jones, B. M., Zebker, H. A., Williams, C. A., Rogan, J. & Zhang, T. (2014). InSAR detects increase in surface subsidence caused by an Arctic tundra fire, *Geophys. Res. Lett.*, 41, 3906–3913, doi:10.1002/2014GL060533.
- Liu, L., Schaefer, K. M., Chen, A. C., Gusmeroli, A., Zebker, H. A., & Zhang, T. (2015). Remote sensing measurements of thermokarst subsidence using InSAR, *J. Geophys. Res., Earth Surf.*, 1935–1948, doi:10.1002/2015JF003599.
- Mack, M., Bret-Harte, M., Hollingsworth, T., Jandt, R. R., Schuur, E. A. G., Shaver, G. R., & Verbyla, D. L. (2011). Carbon loss from an unprecedented Arctic tundra wildfire, *Nature*, 475, 489–492, doi:10.1038/nature10283.
- Massonnet, D., Rossi, M., Carmona, C., Adragna, F., Peltzer, G., Feigl, K., & Rabaute, T. (1993). The displacement field of the Landers earthquake mapped by radar interferometry. *Nature* 364, 138–142. doi:10.1038/364138a0

-
- Massonnet, D., & Feigl, K. L. (1998). Radar interferometry and its application to changes in the earth's surface. *Reviews of Geophysics*, 36(4), 441–500.
doi.org/10.1029/97RG03139
- Michaelides, R. J., Zebker, H. A., Schaefer, K., Parsekian, A., Liu, L., Chen, J., Natali, S., Ludwig, S., & Schaefer, S. (2019). Inference of the impact of wildfire on permafrost and active layer thickness in a discontinuous permafrost region using the remotely sensed active layer thickness (ReSALT) algorithm, *Environ. Res. Lett.*, 14(3), 035007.
- Molan, Y. E., Kim, J. W., Lu, Z., Wylie, B., & Zhu, Z. (2018). Modeling wildfire-induced permafrost deformation in an Alaskan boreal forest using InSAR observations. *Remote Sensing*, 10(3). doi.org/10.3390/rs10030405
- Morishita, Y., Lazecky, M., Wright, T. J., Weiss, J. R., Elliott, J. R., & Hooper, A. (2020). LiCSBAS: An Open-Source InSAR Time Series Analysis Package Integrated with the LiCSAR Automated Sentinel-1 InSAR Processor. *Remote Sensing*, 12(3), 424.
- Murton, J. B., Edwards, M. E., Lozhkin, A. V., Anderson, P. M., Savvinov, G. N., Bakulina, N., Bondarenko, O. V., Cherepanov, M. V., Danilov, P. P., Boeskorov, V., Goslar, T., Grigoriev, S., Gubin, S. V., Korzun, J. A., Lupachev, A. V., Tikhonov, A., Tsygankova, V. I., Vasilieva, G. V., & Zanina, O. G. (2017). Preliminary paleoenvironmental analysis of permafrost deposits at Batagaika megaslump, Yana Uplands, northeast Siberia, *Quaternary Res.*, 87, 314–330,
doi:10.1017/qua.2016.15.
- Murton, J.B., Opel, T., Toms, P., Blinov, A., Fuchs, M., Wood, J., Gärtner, A., Merchel, S., Rugel, G., Savvinov, G., Wetterich, S. (2021). A multimethod dating study of ancient permafrost, Batagay megaslump, east Siberia. *Quaternary Res.* 1–22.
doi:10.1017/qua.2021.27
- Mutou, Y., Watanabe, K., Ishizaki, T. & Mizoguchi, M. (1998). Microscopic observation of ice lensing and frost heave in glass beads. In *Proc. Seventh Intl. Conf. on Permafrost*, June 23–27, 1998, Yellowknife, Canada (ed. A. G. Lewkowicz & M. Allard), pp. 283–287. Universite Laval, Montreal, Canada.
- Molan, Y. E., Kim, J. W., Lu, Z., Wylie, B., & Zhu, Z. (2018). Modeling Wildfire-Induced Permafrost Deformation in an Alaskan Boreal Forest Using InSAR Observations, *Remote Sens.*, 10, 405; doi:10.3390/rs10030405.
- Narita, D., Gavrilieva, T., & Isaev, A. (2020). Impacts and management of forest fires in the Republic of Sakha, Russia: A local perspective for a global problem. *Polar Science*, 100573. doi.org/10.1016/j.polar.2020.100573

- Natali, S. M., Holdren, J. P., Rogers, B. M., Treharne, R., Duffy, P. B., Pomerance, R., & MacDonald, E. (2021). Permafrost carbon feedbacks threaten global climate goals. *PNAS*, 118(21), 1–3. doi.org/10.1073/pnas.2100163118
- Nelson, F. E., Shiklomanov, N. I., Mueller, G. R., Hinkel, K. M., Walker, D. A. & Bockheim, J. G. (1997). Estimating Active-Layer Thickness over a Large Region: Kuparuk River Basin, Alaska, U.S.A. *Arctic and Alpine Res.*, 29(4), 367. doi.org/10.2307/1551985
- Obu, J., Westermann, S., Bartsch, A., Berdnikov, N., Christiansen, H. H., Dashtseren, A., Delaloye, R., Elberling, B., Etzelmüller, B., Kholodov, A., Khomutov, A., Kääb, A., Leibman, M. O., Lewkowicz, A. G., Panda, S. K., Romanovsky, V., Way, R. G., Westergaard-Nielsen, A., Wu, T., ... Zou, D. (2019). Northern Hemisphere permafrost map based on TTOP modelling for 2000–2016 at 1 km 2 scale. *Earth-Science Reviews*, 193, 299–316, doi.org/10.1016/j.earscirev.2019.04.023
- Olefelt, D., Goswami, S., Grosse, G., Hayes, D., Hugelius, G., Kuhry, P., Mcguire, A. D., Romanovsky, V. E., Sannel, A. B. K., Schuur, E. A. G. & Turetsky, M. R. (2016). Circumpolar distribution and carbon storage of thermokarst landscapes. *Nature Communications*, 7. doi.org/10.1038/ncomms13043
- Ouchi, K. (2004). リモートセンシングのための合成開口レーダの基礎, 第二版. 東京電機大学出版局, (In Japanese)
- Ouchi, K. (2013). Recent Trend and Advance of Synthetic Aperture Radar with Selected Topics. *Remote Sensing* 5, 716–807. doi:10.3390/rs5020716
- Ozawa, T., & Kozono, T. (2013). Temporal variation of the Shinmoe-dake crater in the 2011 eruption revealed by spaceborne SAR observations. *Earth, Planets and Space* 65, 527–537. doi:10.5047/eps.2013.05.004
- Peppin, S. S. L., & Style, R. W. (2013). The Physics of Frost Heave and Ice-Lens Growth, *Vadose Zone J.*, 12, 1-12, doi:10.2136/vzj2012.0049
- Ponomarev, E., Kharuk, V., & Ranson, K. (2016). Wildfires Dynamics in Siberian Larch Forests. *Forests*, 7(12), 125. doi.org/10.3390/f7060125
- Porter, C., Morin, P., Howat, I., Noh, M., Bates, B., Peterman, K., Keesey, S., Schlenk, M., Gardiner, J., Tomko, K., Willis, M., Kelleher, C., Cloutier, M., Husby, E., Foga, S., Nakamura, H., Platson, M., Wethington, M., Williamson, C., Bauer, G., Enos, J., Arnold, G., Kramer, W., Becker, P., Doshi, A., D'Souza, C., Cummins, P., Laurier, F. & Bojesen, M., (2018), “ArcticDEM”, doi.org/10.7910/DVN/OHHUKH, Harvard Dataverse, V1, [2021.7.14].
- Rees, W. G. (2001). *Physical Principles of Remote Sensing*, Cambridge University Press, Cambridge, United Kingdom.

-
- Rempel, A. W., Wettlaufer, J. S. & Worster, M. G. (2004). Premelting dynamics in a continuum model of frost heave, *J. Fluid. Mech.*, 498, 227-224; doi: 10.1017/S00222112003006761
- Rempel, A. W. (2007). Formation of ice lenses and frost heave, *J. Geophys. Res., Earth Surf.*, 112, F02S21, doi:10.1029/2006JF000525.
- Rignot, E., Echelmeyer, K., & Krabill, W. (2001). Penetration depth of interferometric synthetic-aperture radar signals in snow and ice. *Geophys. Res. Lett.*, 28(18), 3501–3504. doi.org/10.1029/2000GL012484
- Rosen, P. A., Hensley, S., Zebker, H. A., Webb, F. H., & Fielding, E. J. (1996). Surface deformation and coherence measurements of Kilauea Volcano, Hawaii, from SIR - C radar interferometry, *J. Geophys. Res., Planets*, 101(E10), 23,109—23,125, doi:10.1029/96JE01459.
- Roshydromet (2008). Assessment report on climate change and its consequences in Russian Federation – General Summary. Moscow.
http://climate2008.igce.ru/v2008/pdf/resume_ob_eng.pdf
- Rouyet, L., Lauknes, T. R., Christiansen, H. H., Strand, S. M., & Larsen, Y. (2019). Seasonal dynamics of a permafrost landscape, Adventdalen, Svalbard, investigated by InSAR. *Remote Sens. Environ.*, 231, 111236, doi:10.1016/j.rse.2019.111236.
- Samsonov, S. V., Lantz, T. C., & Kokelj, S. V. (2016). Growth of a young pingo in the Canadian Arctic observed by RADARSAT-2 interferometric satellite radar. *The Cryosphere*, 10(2), 799, doi:10.5194/tc-10-799-2016.
- Schirmermeister, L., Froese, D., Tumskoy, V., Grosse, G., & Wetterich, S. (2013). Yedoma: Late Pleistocene Ich-Rich Syngenetic Permafrost of Beringia, in *Encyclopedia of Quart. Sci.*, 3, 542-552.
- Schmidt, D. A. & Bürgmann, R. (2003). Time-dependent land uplift and subsidence in the Santa Clara valley, California, from a large interferometric synthetic aperture radar data set, *J. Geophys. Res.*, 108(B9), 2416, doi:10.1029/2002JB002267
- Schuster, P. F., Schaefer, K. M., Aiken, G. R., Antweiler, R. C., Dewild, J. F., Gryziec, J. D., Gusmeroli, A., Hugelius, G., Jafarov, E., Krabbenhoft, D. P., Liu, L., Herman-Mercer, N., Mu, C., Roth, D. A., Schaefer, T., Striegl, R. G., Wickland, K. P. & Zhang, T. (2018). Permafrost Stores a Globally Significant Amount of Mercury. *Geophys. Res. Lett.*, 45 (3), 1463–1471. doi.org/10.1002/2017GL075571
- Schuur, E. A. G., McGuire, A. D., Schädel, C., Grosse, G., Harden, J. W., Hayes, D. J., Hugelius, G., Koven, C. D., Kuhry, P., Lawrence, D. M., Natali, S. M., Olefeldt, D., Romanovsky, V. E., Schaefer, K., Turetsky, M. R., Treat, C. C. & Vonk, J. E.

- (2015). Climate change and the permafrost carbon feedback, *Nature*, 520, 171–179, doi:10.1038/nature14338.
- Shiklomanov, N. I. & Nelson, F. E. (2002). Active-layer mapping at regional scales: A 13-year spatial time series for the Kuparuk region, north-central Alaska. *Permafr. Periglac. Processes*, 13 (3), 219–230. doi.org/10.1002/ppp.425
- Shiklomanov, N. I., Streletskiy, D. A., Little, J. D., & Nelson, F. E. (2013). Isotropic thaw subsidence in undisturbed permafrost landscapes, *Geophys. Res. Lett.*, 40, 6356–6361, doi:10.1002/2013GL058295.
- Short, N., Brisco, B., Couture, N., Pollard, W., Murnaghan, K., Budkewitsch, P. (2011). A comparison of TerraSAR-X, RADARSAT-2 and ALOS-PALSAR interferometry for monitoring permafrost environments, case study from Herschel Island, Canada, *Remote Sens. Environ.*, 115, 3491—3506, doi:10.1016/j.rse.2011.08.012
- Shur, Y., Hinkel, K.M., and Nelson, F.E. (2005). The transient layer: implications for geocryology and climate-change science. *Permaf. Perig. Processes*, 16, 5–17. doi:10.1002/ppp.518
- Siberian Times (2019). <https://siberiantimes.com/other/others/news/hell-on-fire-raging-bush-inferno-at-batagai-depression-giant-gash-in-the-tundra/>
- Singhroy, V., R. Couture, P. - J. Alasset, & V. Poncos (2007), InSAR monitoring of landslides on permafrost terrain in Canada, in 2007 IEEE International Geoscience and Remote Sensing Symposium, pp. 2451–2454, *Inst. of Electr. and Electr. Eng.*, Piscataway, N. J.
- Simons, M., & Rosen, P. A. (2015). Interferometric Synthetic Aperture Radar Geodesy. In *Treatise on Geophysics: Second Edition* (Vol. 3). Elsevier B.V. doi.org/10.1016/B978-0-444-53802-4.00061-0
- Strozzi, T., Antonova, S., Günter, F., Mätzler, E., Vieira, G., Wegmüller, U., Westermann, S. & Bartsch, A. (2018). Sentinel-1 SAR Interferometry for Surface Deformation Monitoring in Low-Land Permafrost Areas, *Remote Sens.*, 10, 1360, doi:10.3390/rs10091360
- Takada, Y., & Fukushima, Y. (2013). Volcanic subsidence triggered by the 2011 Tohoku earthquake in Japan. *Nature Geoscience*. 6, 637–641. doi:10.1038/ngeo1857
- Tarnocai, C., Canadell, J. G., Schuur, E. A. G., Kuhry, P., Mazhitova, G. & Zimov, S. (2009). Soil organic carbon pools in the northern circumpolar permafrost region. *Global Biogeochemical Cycles*, 23 (2), doi.org/10.1029/2008gb003327
- Taber, S. (1929). Frost heaving, *J. Geol.*, 37:428–461. doi:10.1086/623637
- Taber, S. (1930). The mechanics of frost heaving, *J. Geol.*, 38:303–317. doi:10.1086/623720

-
- Tsai, Y. L. S., Dietz, A., Oppelt, N., & Kuenzer, C. (2019). Remote sensing of snow cover using spaceborne SAR: A review. *Remote Sensing*, 11(12).
doi.org/10.3390/rs11121456
- Turetsky, M.R., Abbott, B.W., Jones, M.C., Anthony, K.W., Olefeldt, D., Schuur, E.A.G., Grosse, G., Kuhry, P., Hugelius, G., Koven, C., Lawrence, D.M., Gibson, C., Sannel, A.B.K., & McGuire, A. D. (2020). Carbon release through abrupt permafrost thaw. *Nature Geoscience*, 13, 138–143.
- Vonk, J. E., Tank, S. E., Bowden, W. B., Laurion, I., Vincent, W. F., Alekseychik, P., Amyot, M., Billet, M. F., Canário, J., Cory, R. M., Deshpande, B. N., Helbig, M., Jammet, M., Karlsson, J., Larouche, J., Macmillan, G., Rautio, M., Walter Anthony, K. M. & Wickland, K. P. (2015). Reviews and syntheses: Effects of permafrost thaw on Arctic aquatic ecosystems. *Biogeosciences*, 12 (23), 7129–7167.
doi.org/10.5194/bg-12-7129-2015
- Walter, K. M., Chanton, J. P., Chapin, F. S., Schuur, E. A. G. & Zimov, S. A. (2008). Methane production and bubble emissions from arctic lakes: Isotopic implications for source pathways and ages. *J. Geophys. Res. Biogeosci.*, 113 (3).
doi.org/10.1029/2007JG000569
- Wagner, A. M., Lindsey, N. J., Dou, S., Gelvin, A., Saari, S., Williams, C., Ekblaw, I., Ulrich, C., Borglin, S., Morales, A., Ajo-Franklin, J. (2018). Permafrost Degradation and Subsidence Observations during a Controlled Warming Experiment, *Sci. Rep.*, 8:10980, doi:10.1038/s41598-018-29292-y
- Wang, Z., & Li, S. (1999), Detection of winter frost heaving of the activelayer of Arctic permafrost using SAR differential interferograms, in IGARSS'99 Proceedings: Remote Sensing of the System Earth - A Challenge for the 21st Century: IEEE 1999 International Geoscience and Remote Sensing Symposium, 28 June - 2 July 1999, Congress Centrum Hamburg, pp. 1946–1948, *Inst. of Electr. and Electr. Eng.*, Piscataway, N. J.
- Watanabe, K. & Mizoguchi, M. (2000). Ice configuration near a growing ice lens in a freezing porous medium consisting of micro glass particles, *J. Cryst. Growth*, 213, 135–140.
- Wegmüller, U., & Werner, C. L. (1997). Gamma SAR processor and interferometry software. Proc. of the 3rd ERS Symposium, *European Space Agency Special Publication*, ESA SP-414, 1687–1692.
- Wettlaufer, J. S. & Worster, M.G (2006). Premelting Dynamics, *Annu. Rev. Fluid Mech.*, 38:427–52

- Worster, M. G., & Wettlaufer, J. S. (1999). The fluid mechanics of premelted liquid films. In *Fluid Dynamics at Interfaces* (ed. W. Shyy & R. Narayanan), pp. 339–351. Cambridge University Press.
- Yanagiya, K., & Furuya, M. (2020). Post - Wildfire Surface Deformation Near Batagay, Eastern Siberia, Detected by L - Band and C - Band InSAR. *J. Geophys. Res.: Earth Surface*, 125. doi:10.1029/2019jf005473
- Yoshikawa, K., Bolton, W. R., Romanovsky, V. E., Fukuda, M., & Hinzman, L. D. (2002). Impacts of wildfire on the permafrost in the boreal forests of Interior Alaska, *J. Geophys. Res.*, 107(D1), 8148, doi:10.1029/2001JD000438.
- Zhang, Y., Wolfe, S. A., Morse, P. D., & Fraser, I. O. R. H. (2015). Spatiotemporal impacts of wildfire and climate warming on permafrost across a subarctic region, Canada, *J. Geophys. Res. Earth Surf.*, 120, 2338–2356, doi:10.1002/2015JF003679.
- Zwieback, S., Hensley, S., & Hajnsek, I. (2015). Assessment of soil moisture effects on L-band radar interferometry. *Remote Sens. Environ.*, 164, 77-89, doi: 10.1016/j.rse.2015.04.012
- Zwieback, S., Liu, X., Antonova, S., Heim, B., Bartcsh, A., Boike, J., & Hajnsek, I. (2016). A Statistical Test of Phase Closure to Detect Influences on DInSAR Deformation Estimates Besides Displacements and Decorrelation Noise: Two Case Studies in High-Latitude Regions. *IEEE Trans. Geosci. Remote Sens.*, 54(9), 5588-5601, doi: 10.1109/TGRS.2016.2569435.

Chapter 8. Appendix

Table 8-1. Data list of ALOS-2 for interferograms in Figures 2-4 a-e and Figure 2-7.

Interferogram	Dates (YYYYMMDD)	Perpendicular Baseline (m)	Temporal Baseline (days)
Short-term images (Figure 2-4)			
(a)	20170617-20170729	11	48
(b)	20170729-20171009	-104	72
(c)	20171009-20171202	-46	54
(d)	20171202-20180310	283	98
(e)	20180310-20180602	-259	84
Long-term images (Figure 2-7)			
(a)	20151010-20161008	98	364
(b)	20160730-20170729	97	364
(c)	20161008-20171007	-104	364
(d)	20161217-20171202	-146	350
(e)	20170617-20180602	-118	350
(f)	20170729-20180728	-200	364
(g)	20180310-20190309	-191	364
(h)	20180602-20190601	41	364

Table 8-2. Data list of Sentinel-1 for interferograms in Figures 2-4 f-j and 2-6.

Stack	Interferogram	Dates (YYYYMMDD)	Perpendicular Baseline (m)	Temporal Baseline (day)
(f)	(1)	20170611-20170623	23	12
	(2)	20170623-20170705	-74	12
	(3)	20170705-20170729	-15	24
(g)	(4)	20170729-20170810	43	12
	(5)	20170810-20170822	-30	12
	(6)	20170822-20170903	36	12
	(7)	20170903-20170915	-15	12
	(8)	20170915-20170927	-54	12
	(9)	20170927-20171009	35	12
(h)	(10)	20171009-20171021	80	12
	(11)	20171021-20171102	32	12
	(12)	20171102-20171114	-46	12
	(13)	20171114-20171126	-89	12
	(14)	20171126-20171208	26	12
(i)	(15)	20171208-20171220	114	12
	(16)	20171220-20180101	43	12
	(17)	20180101-20180113	-66	12
	(18)	20180113-20180125	-143	12
	(19)	20180125-20180206	34	12
	(20)	20180206-20180218	59	12
	(21)	20180218-20180302	26	12
	(22)	20180302-20180314	-25	12
(j)	(23)	20180314-20180407	-91	24
	(24)	20180407-20180419	-43	12
	(25)	20180419-20180501	155	12
	(26)	20180501-20180513	-29	12
	(27)	20180513-20180525	-74	12
	(28)	20180525-20180606	-73	12

Table 8-3. Data list of ALOS-2 for interferograms in Figures 3-7.

Dates (yyyymmdd)	Time span (days)	Perpendicular baseline (m)	Image Mode/Path/Frame
20180310 to 20190309	364	-192	SM3/122/1360
20180602 to 20190601	364	41.8	SM3/122/1360
20190309 to 20200307	364	103.8	SM3/122/1360
20190601 to 20200530	364	118.7	SM3/122/1360
20200307 to 20210306	364	152	SM3/122/1360

Table 8-4. Data list of Sentinel-1 for interferograms in Figure 3-3, 3-4, 3-5, and 3-6.

Stack	Dates (yyyymmdd)	Time span (days)	Perpendicular baseline (m)
	20180419 to 20180501	12	154.9
	20180501 to 20180513	12	-29.3
	20180513 to 20180525	12	-74.6
	20180525 to 20180606	12	-72.8
	20180606 to 20180618	12	42.5
	20180618 to 20180630	12	135.7
	20180630 to 20180712	12	-18.4
	20180712 to 20180724	12	-46.3
	20180724 to 20180805	12	-70.5
	20180805 to 20180817	12	0.4
	20180817 to 20180829	12	-5.9
	20180829 to 20180922	24	110.4
	20180922 to 20181004	12	-42.8
Figure 3-3 (a)	20181004 to 20181016	12	-27.7
	20181016 to 20181028	12	87.4
	20181028 to 20181109	12	62.4
Figure 3-3 (b)	20181109 to 20181121	12	-7.1
	20181121 to 20181203	12	-20.3
	20181203 to 20181215	12	-125.0

Figure 3-3 (c)	20181215 to 20181227	12	52.1
	20181227 to 20190108	12	80.1
	20190108 to 20190120	12	16.7
	20190120 to 20190201	12	8.3
	20190201 to 20190213	12	-178.1
	20190213 to 20190225	12	39.6
	20190225 to 20190309	12	50.9
	20190309 to 20190321	12	21.4
	20190321 to 20190402	12	19.0
	20190402 to 20190414	12	-65.0
	20190414 to 20190426	12	-58.7
	20190426 to 20190508	12	41.7
	20190508 to 20190520	12	88.9
	20190520 to 20190601	12	-26.1
	20190601 to 20190613	12	-25.8
	20190613 to 20190625	12	-89.5
	20190625 to 20190719	24	85.0
	20190719 to 20190731	12	-23.6
	20190731 to 20190812	12	5.6
	20190812 to 20190905	24	-65.9
Figure 3-3 (d)	20190905 to 20190917	12	20.3
	20190917 to 20190929	12	145.2
	20190929 to 20191011	12	-76.4
	20191011 to 20191023	12	-47.5
	20191023 to 20191104	12	-7.3
Figure 3-3 (e)	20191104 to 20191116	12	77.1
	20191116 to 20191128	12	69.5
	20191128 to 20191210	12	-4.7
Figure 3-3 (f)	20191210 to 20191222	12	-43.0
	20191222 to 20200103	12	-84.5
	20200103 to 20200127	24	69.1
	20200127 to 20200208	12	102.7
	20200208 to 20200220	12	-97.2
	20200220 to 20200303	12	-110.7

	20200303 to 20200315	12	-15.7
	20200315 to 20200327	12	69.5
	20200327 to 20200408	12	77.9
	20200408 to 20200420	12	-5.5
	20200420 to 20200502	12	-99.7
	20200502 to 20200526	24	-31.6
	20200526 to 20200607	12	114.4
	20200607 to 20200619	12	2.3
	20200619 to 20200701	12	-61.3
	20200701 to 20200713	12	-55.9
	20200713 to 20200725	12	51.2
	20200725 to 20200806	12	34.9
	20200806 to 20200818	12	-46.5
	20200818 to 20200830	12	28.0
	20200830 to 20200911	12	-35.7
	20200911 to 20200923	12	-14.3
	20200923 to 20201005	12	55.5
Figure 3-3 (g)	20201005 to 20201017	12	28.9
	20201017 to 20201029	12	13.1
	20201029 to 20201110	12	-40.7
Figure 3-3 (h)	20201110 to 20201122	12	-40.5
	20201122 to 20201204	12	89.5
	20201204 to 20201216	12	53.9
Figure 3-3 (i)	20201216 to 20201228	12	0.3
	20201228 to 20210109	12	-81.0
	20210109 to 20210121	12	-51.5
	20210121 to 20210202	12	-5.4
	20210202 to 20210214	12	100.3
	20210214 to 20210226	12	10.0
	20210226 to 20210310	12	-40.8
	20210310 to 20210415	36	-114.6

Table 8-5. Data list of ALOS-2 SM1 interferograms in Chapter 4.

Primary Date (yyyymmdd)	Secondary Date (yyyymmdd)	Time span (days)	Perpendicular baseline (m)	Image Mode/Path/Frame
20200828	20201023	56	53	SM1/28/2240
	20210312	196	282	
	20210813	350	-9	
	20211022	420	-59	
20201023	20210312	140	229	
	20210813	294	-62	
	20211022	364	-113	
20210312	20210813	154	-291	
	20211022	224	-341	
20210813	20211022	70	-50	



Figure 8-1. The pictures of pits at the transect of the gully (Chapter 4.3.4).